GEORG-AUGUST-UNIVERSITÄT GÖTTINGEN

Faculty for Physics

Institute for the Dynamics of Complex Systems

MAX PLANCK INSTITUT FOR DYNAMICS AND SELF-ORGANISATION


Master thesis

---

# Wechselwirkung von Aktin- und Clathrin-Punctae bei der Adhesion von *Dictyostelium discoideum*.

# Interplay of actin foci and clathrin rich areas upon *Dictyostelium discoideum* adhesion.

---


prepared by

**Christoph Schich**


17.09.2020, Göttingen


# Contents

# 1. Introduction

Cell movement is essential for life. If one were to assume a unicellular organism without the ability of self-induced movement, it would rely on diffusion through Brownian motion for movements and its nutrient uptake and would not even be able to actively ingest them. Due to their small size, however, cell movement is dominated by their environmental viscosity and can be divided into two different types of locomotion: swimming and crawling. Cells, like some bacteria or spermatozoon, move with the help of flagella, a long whip composed of microtubles which rotate in a propeller-like movement. Further, a swimming movement due to collective beating of a variety of cilia was found, which is smaller then flagella but comparable in its structure.
Cell crawling upon which besides for example blebb-based or lamellipodia-based migration, the actin driven amoeboid like movement is one central migration mode. It can be segmented into three parts: protrusion of the cell membrane forming a pseudopodia at the leading edge, interaction and adhesion of specialised proteins located at the pseudopdia with the substrate and retraction of the cell back, the uropod, and its contraction in order to shift the cell center forward. This movement is mainly driven by the interactions of the actomyosin-cortex, with actin as one of three components defining the cytoskeleton, besides the mentioned microtubules and intermediate filaments neither of whom plays any part in this work.
Cell crawling is the most common type of movement for eukaryotic cells and essential to a variety of processes like wound healing or cancer metastasis. After an injury, polymorphonuclear neutrophils and macrophages move towards the inflammation to attack and ingest the intruding microorganisms. After this inflammatory stage, fibroblasts enter the wounded area to produce collagen and fibronectin, which are parts of the extra cellular matrix (ECM), to form a scaffold for recolonization. These cells move in response to a chemical stimulus a process manner called chemotaxis.
Another example for directed cell crawling is cancer cell metastasis which describes the invasion of cancer cells from the primary tumor and the resulting formation of new tumors in the organism. Reducing the cell-substrate and cell-cell adhesion strength of cancer cells enables them to escape from the tissue dynamics. A major transmembrane protein for cell-cell adhesion is E-cadherin, the loss of which promotes cancer metastasis [1]. In order to interact and move on the surrounding ECM the metastatic cells relies amongst others transmembrane proteins on members of the integrin family. This shows the importance of the adhesion process and the destructive effect of changes in adhesion for the formation of metastases. Thus, knowledge of molecular and cell biophysical details of cell adhesion and the proteins involved is crucial for understanding the whole process and its consequences and,

therefore, may lead to revealing possible cures.
As a highly simplified model, a cell adhering to a surface can be compared to a shell composed of phospholipds, a liposome, sticking non specifically to a substrate through Van der Walls (VdW) interactions. Based on the assumption of a liquid droplet wetting a surface, the adhesion strength of the entire cell can be described as a function of the contact area, by assuming a uniform adhesion [2]. It has been shown that even in this passive system of a polymeric capsule, membrane properties can lead to deformation of the capsule and thus lead from a heterogeneous contact area to area spots closer to the substrate [3].
In addition, repulsive interaction arises due to thermal membrane fluctuation, buffering glycoproteins and electrostatic interactions between the substrate and the membrane. Adhesion is ensured by specific clusters of proteins that serve as contact points to the substrate or neighbouring cells. The Regulation of adhesion and unbinding is vital for cell movement.
Endocytosis is the internalization of external material into the cell. One can distinguish between phagocytosis as the engulfment of larger substances for example microorganisms or cell debris what is often refereed to as cell eating, the pinocyotis utilized for fluid uptake and the receptor mediated endocytosis. Clathrin is a protein required for the uptake of fluid or receptor cargo through clathrin mediated endocytosis (CME) from the plasma membrane. However, it was shown that clathrin plays an additional role in cell adhesion for mammalian cells. In the disassembly of focal adhesion by integrin engulfment and in the creation of long lived clathrin coated structures (CCS) as adhesion platforms for example for sensing of substrate rigidity.
This work focuses on the analysis of the adhesion process of *Dictyostelium discoideum* (*D.d.*). It is remarkable that these cells adhere and crawl despite lacking integrins. Instead *D.d.* rely on adhesion proteins like SadA or SibA that form clusters of a multitude of proteins connected to spots of high actin activity, actin foci, at the ventral cell side. The amoeboid CME shows similarities to mammalian cells as the dependence on actin activity, occurrence on the ventral side of the cell or as possible pathway for transmembrane protein uptake. Furthermore it was detected, that the membrane-substrate distance is reduced on the appearance of a clathrin rich area (CRA). The aim of this Masters thesis is to investigate the degree of participation of CRA in the adhesion of *D.d.* and thus the interplay with actin foci.
To investigate this, height maps of fluorescence-labeled proteins at the ventral side of the cell are record with Metal-induced energy transfer (MIET) microscopy. MIET allows to measure changes in the fluorescence lifetime of fluorophors in close vicinity to a metal surfaces with a spatial resolution of 250nm and 3nm accuracy of z height information. This enables the height determination of membrane and freshly polymerised actin or clathrin and further the relative comparison between the height maps.
Another way used to investigate the adhesion of CRA in *D.d.* is the assessment of adhesion properties of wild-type and clathrin light chain (clc) knock-out cells with atomic force microscopy- based Single Cell Force Spectroscopy (SCFS). As shown previously for *D.d.*, the stochastic step like rupture events, visible upon cell

retraction from the surface, rely on collective unbinding of adhesion proteins in bond clusters [2].
MIET and SCFS individually consider different aspects of CRA, whereas the combination of both methods can help to place the information gained in the overall context to better understand the adhesion process.

# 2. Background

## 2.1. Dictyostelium Discoideum (*D.d.*) and its Life Cycles

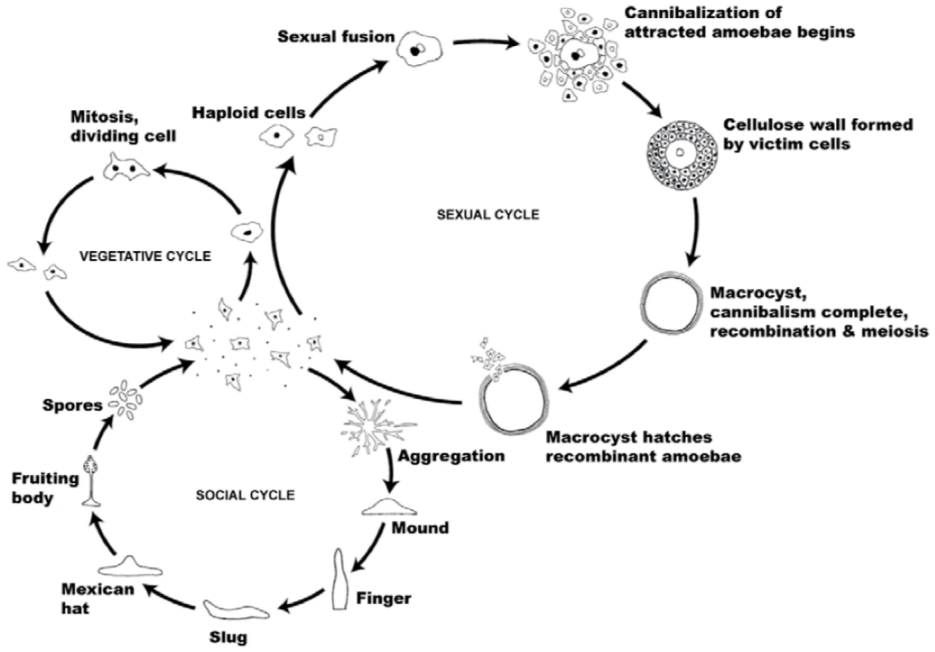


Figure 2.1.: Under ideal conditions the *D.d.* feeds on bacteria and divides by mitosis during the vegetative cycle. Upon food shortage, the amoeba can transfer to one of the other two cycles. Following the sexual cycle, two matching haploid *D.d.* fuse and begin to prey on surrounding cells. Victim cells build a shielding vacuole wall around the group. After several intermediate steps and upon finding better living conditions, the recombinant cells leave the generated macrocyste and colonize their environment. Another more heavily studied mechanism is the social cycle. A large group of *D.d.* aggregate in a slug-like multicellular body. In this state, cells are more motile to reach larger distances in search of better preying conditions. During continued absence of bacterial nutrient, the group forms a fruiting body in order for cell spores to colonize new areas. Extracted from [4].

The soil dwelling amoeba *Dictyostelium discoideum* (*D.d.*) is a commonly used model organism to investigate cell migration, signal transducation, adhesion and chemotaxis.
*D.d.* cells have the ability to react to different biological environments, by performing one of the three (social) life cycles, shown in Figure 2.1. Under ideal conditions, the social amoeba *D.d.* live in their natural habitate soil, hunt and feed on bacteria during the vegetative cycle. To hunt, *D.d.* detects folate, which is synthesised and secreted by some types of bacteria and functions as a chemoattractant. The folic acid is detected by fAR1, a G-protein-coupled receptor whose activation stimulates pathways for actin activity. The activation thus stimulates chemotactic movement and enables the engulfment of the bacteria by utilizing the plasma membrane, a process called phagocytosis [5]. During the vegetative cycle cells can reproduce by binary fission with the cell number doubling after roughly 8 hours.
With a depleted food supply, cells can enter one of the following cycles depending on their environmental conditions.
After a period of starvation *D.d.* passes through developmental changes, e.g. by synthesizing and releasing the chemical cyclic adenosine monophosphate (cAMP), increases the expression of the membrane receptor carA or by down regulating adhesion proteins to decrease the overall adhesion which can result in a motility increase [6–8]. After roughly 6 hours of starvation *D.d.* periodically releases cAMP. The external chemical signal is detected by receptor proteins like carA, which activates a G-protein whose pathways influence the actin network and likewise cAMP release of the cell [6]. The detection and release of cAMP enables the cells to create a chemical gradient in which they crawl in a chemotactic movement towards the highest cAMP concentration and aggregate at its center, with up to $100,000$ cells [9]. The aggregated cells form a slug-like structure to cover larger distances in search of better living conditions. At further absence of food, the social cycle leads to a fruiting body formation on top of a stalk formed from self-sacrificing cells. The resulting cell spores can be transported by the wind and colonize their surroundings under better conditions.
Under darkness and wet conditions the cells can proliferate following the sexual cycle. This cycle allows a gene exchange and leads to the building of a macrocyst that is better fitted to endure poor living conditions [10].

## 2.2. Actin Cortex Structure

The actin cortex is a $100 - 200$nm thin layer comprised of a dynamic actin scaffold and a variety of specialized actin-binding proteins interacting with the cortex. This highly dynamical network adjacent to the cell membrane plays a crucial role by defining the cell shape, creating cell movement and adhesion and is being involved in the internalisation of membrane vesicles [12].
The polymerisation process of globular, monomeric actin (G-actin), linked to adenosine

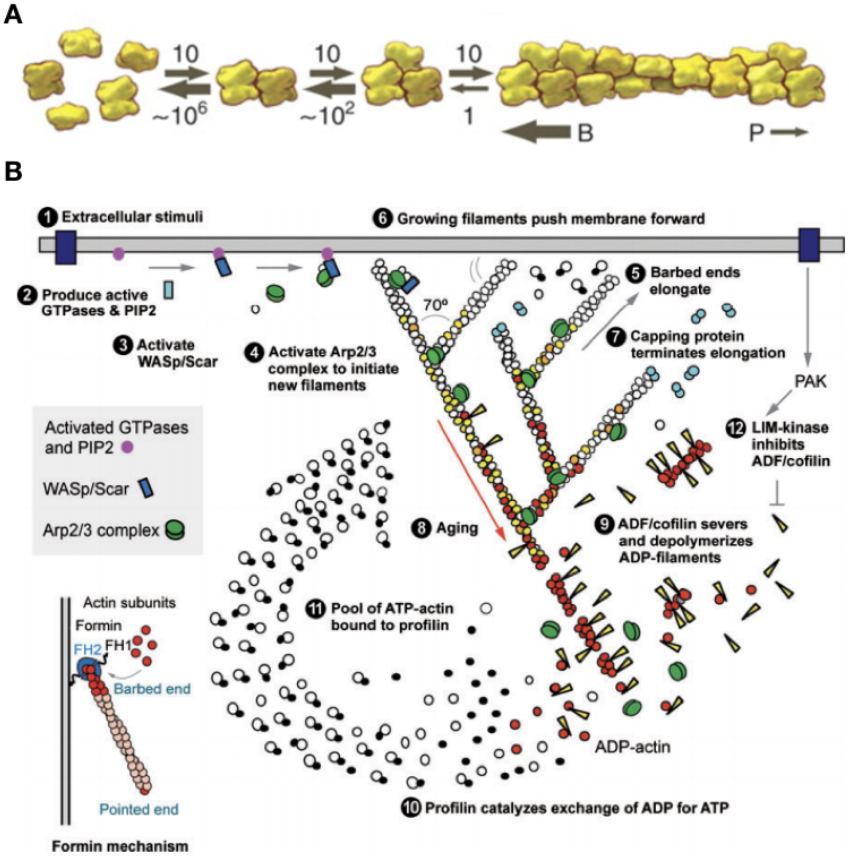


Figure 2.2.: Example for actin dynamics of G-actin assembly and filament branching. (A) Dynamics of actin filament elongation. The filament polymerizes faster at the barbed end (B arrow) than at the pointed end (P arrow). The dimers and trimers are unstable which promotes the building of a pool of actin monomers. The rate constants are expressed with the arrow size. The association rate constant is given in units of $\mu M^{-1}s^{-1}$ and the dissociation rate constant in units of $s^{-1}$[11]. Adapted from [12]. (B) Branching of an actin filament. The WASp/Scar proteins promote and activate the Arp2/3 complex. Together with a G-actin, they bind to a filament and enable the growth of a side branch in a 70° angle. The growing filament branch pushes against the membrane. A capping protein can bind to the barbed end of the filaments and, thereby, regulate the expansion. The ATP-actin sub-units of the filament ages by hydrolyzing ATP to ADP. This promotes depolymerization of the filaments through ADF / cofilin. Extracted from [13].

triphosphat (ATP), on an existing actin filament without the influence of actin-binding proteins is shown in Figure 2.2 (A). The sub-units of the polymer are oriented in the same direction and the filament ends differ in their de- and polymerisation rate. This results in a higher polymerisation velocity at the barbed end in comparison

to the pointed end, so the actin filament is polar. Interestingly, the polymerisation rate is higher than the depolymerisation rate which facilitates growth and a long lifetime of the actin filament [12]. Also, the depolymerisation rate of small oligomeres is much larger than their polymerisation rate. Thus, the nucleation of new actin filaments is unlikely in comparison to the instability of small actin oligomers at the minus end. This ensures a pool of G-actin and promotes directed growth of larger polymers at the plus end [12].
An overview of the dynamic process of actin filament growth and its interaction with proteins is shown in Figure 2.2 (B). Besides the filament elongation, the branching at an existing filament is another way of elongation and thereby creates a cross-linked and gel-like structure. For this, activated WASp/Scar proteins bind together with G-actin to form the Arp2/3 complex. This activated complex binds to a mother filament and enables the elongation of a daughter filament in a 70° angle [13]. The branching network can exert forces against structures which can for example result in pushing the membrane outward. It is located at membrane protrusions, for example in pseudopodia formation or in phagocytosis, but the appearance of WASp and its interactions with Arp2/3 are also involved in the engulfment of membrane vesicle during CME [14]. The further growth of filaments can be hindered by capping proteins.
The protein formin, supports nucleation of filaments by interacting with the barbed end and thereby, hindering interactions with capping proteins and thus promoting elongation [13]. Formins are for example found in unbranched actin bundles at filopodia [12]. However, after the polymerisation, hydrolysis of ATP passes actin into the ADP state, which is also referred to as aging of the filament. This structural transition enables binding of regulatory proteins and partial disassembly of the actin filament.

Other proteins playing a major role at the actin cortex are motor proteins. The only known family of motor proteins interacting with actin are myosins. *D.d.* possesses 13 members of the myosin family fulfilling different tasks[16]. The different myosin proteins have a relatively conserved motor domain, interacting with actin filaments by hydrolysis of ATP and varying in their tail domain. For example expresses *D.d.* 7 different types of Myosin-I, of which 6 posses a region for membrane interactions [16]. The most prominent member of the myosin family involved in *D.d.* movement is myosin-II. Two myosin-II motors can assemble on different actin filaments and stabilize the filaments or generate contractive forces as shown in Figure 2.3. This movement of actin filaments against each other, contracts the uropod to push the cell center forward. Myosin-II is localized in adhesion regions at the cell periphery which suggests that the exerted forces possibly contribute to actin foci dynamics [17, 18].

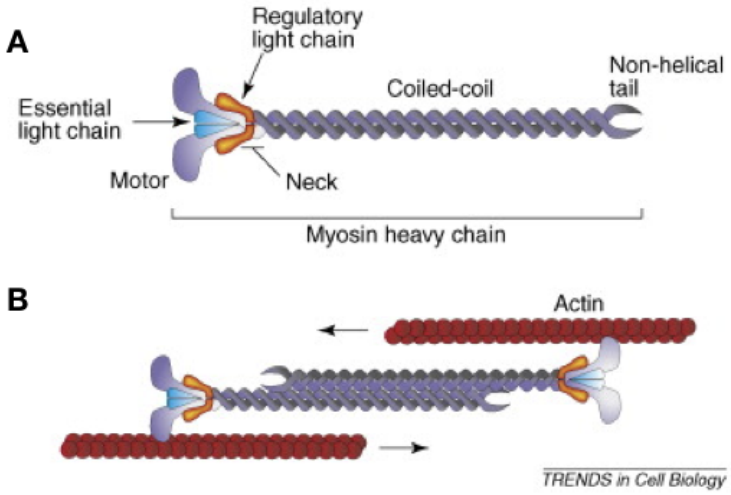


Figure 2.3.: (a) Schematic drawing of a myosin II motor. The protein is composed of two heavy chains linked in a coiled-coil. The heavy chain possesses a motor or head domain which attaches to actin filaments and a neck region which is comparable to a rigid lever and moves the motor head. The light chain is attached to the neck region which supports the motor and regulates the ATPase activity. (b) Example of two self-assembled myosin II motors. They attach to the coiled-coil region and generate a force by walking on differently oriented actin filaments. From [15].

## 2.3. Cell Adhesion

Interaction between cells and their surroundings is essential for many processes ranging from active cell movement and the necessary cell-substrate adhesion to tissue formation with cell-cell adhesion. Cell-cell adhesion does not play a role in this work.

### 2.3.1. Adhesion Proteins and Focal Adhesion

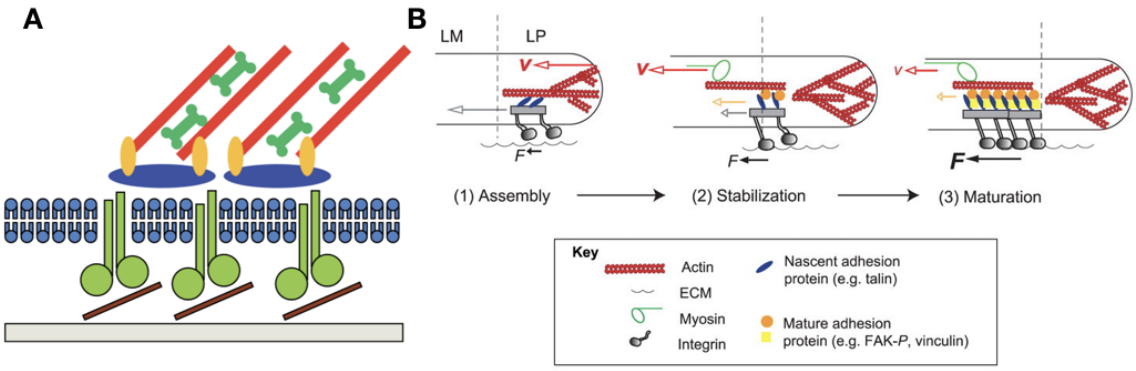


Figure 2.4.: (a) Transmembrane proteins (green) like integrin embedded into the plasma membrane gets activated, either by intracellular binding of proteins to the cytosolic tail or by binding to ligands of the ECM. Talin can cross-link adhesion proteins (blue) and bind like vinculin (yellow) to actin cortex. Myosin-II can connect actin fibers to exert contractile forces or stabilize the cytoskeleton. Extracted from [19]. (b) Schematic drawing of the relation between retrograde flow and adhesion cluster. (1) Freshly polymerized actin in membrane protrusion drives retrograde flow (red arrow) with adhesion proteins (grey arrow). The resulting traction force of the assembling adhesion spot is small (black arrow). (2) With an increased adhesion, the retrograde flow velocity is reduced and the traction force increased. Further actin flow is driven by myosin contractions. (3) The size of the adhesion cluster increases while aging. For mammalian cells as shown here, further focal adhesion proteins begin to interact and actin stress fibers assemble. The traction force further increases. Extracted from [20].

To establish a sufficiently strong bond, information about their environmental properties, for example by probing substrate rigidity, is necessary [21]. The cell interacts with their environment by using proteins incorporated into the plasma membrane to promote adhesion. Mammalian cells adhere employing the integrin family of transmembrane proteins. These adhesion proteins bind to the ECM and are intracellularly connected to the actin cortex by anchoring proteins like talin,

$\alpha$-actinin, filamin, paxillin or vinculin [22]. Besides the connection between integrin and the actin cortex, proteins like talin also cross-link neighboring integrins and, thereby, further stabilize the focal adhesion.
Integrins can assemble into adhesion clusters called focal adhesion what is shown in Figure 2.4 (a). Besides mechanical stabilization and anchoring of the cell to the substrate, focal adhesion points also serve as signaling platforms. Thereby, proteins, which are part of the signaling complexes, regulate cluster properties, migration and consequently cell behavior. A prominent example for the regulation of focal adhesion points is the Rho-family small GTPase, whose activation is regulated by integrin signaling pathways. The Rho signaling pathways, influence the actin-myosin cortex and affect adhesion assembly and disassembly [23]. Thereby, Rho regulates large and long lived focal adhesion regions and is often localized on actin-stress fibers. The migrating regions of the cell require a dynamical adhesion. Often smaller focal adhesion region, referred to as focal complexes with a short lifetime, can be found in lamellipodia regions as shown in Figure 2.4 (b), which are regulated by Rac proteins [24].

### 2.3.2. Cell Adhesion and Movement

From a physical point of view, cells need to form a sufficiently strong bond to a substrate to exert traction force onto the substrate to create an active movement. It is important that the back of the cell is detached and retracted to increase the cell pressure and thereby shift the cytoplasm in direction of movement.
Besides a strong bond to transmit forces to the substrate, cells couple the adherent areas to a force generator. The actin-myosin cortex generates forces by a retrograde actin flow, the action of stress fibers or due to contractile myosin activity at the actin network [20].
The actin network polymerises at the leading edge of a cell forming a lamellipodia, thereby actin polymerization and myosin activity can drive a retrograd actin flow towards the cell center as shown in Figure 2.4 (B,1). A possible explanation for a flow on the basis of locomotion could mark it as a consequence of a contraction between the elongating actin networking and the cortex of the momentary, stationary cell body which result in a force against the direction of the flow [25]. For example a model has been proposed for a myosin based retrograd flow in filopodia of neuronal growth cones [26]. In addition, the membrane tension influences the lamellipodia extension and can therefore contribute in the generation of the retrograde flow [27]. By anchoring the elongating actin filaments through new formed focal adhesion points, with the substrate, the local retrograde flow velocity is reduced [28] as shown in Figure 2.4 (B), what hints at a support for the generated protrusion.

### 2.3.3. Theoretical Description of Adhesion Clusters Formation and their Stability

A single integrin binds to members of the ECM with a short lifetime with a dimension of seconds. If a constant number of adhesion molecules is uniquely distributed

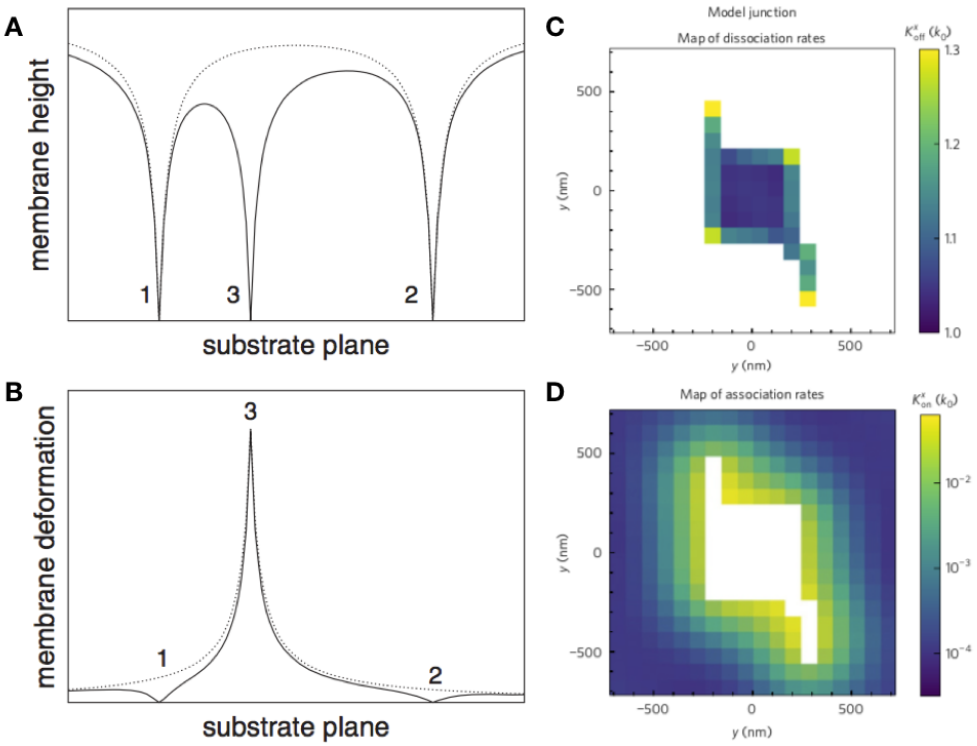


Figure 2.5.: (A) shows a set of two existing bonds (1,2; dashed line) and the membrane contour after a height change under bond formation (3; black line). New formed bond reduces the overal membrane height, what reduces the load on the other on the other bonds depending on the distance to the other bonds. (B) shows that the membrane deformation by forming a bond on the set of two existing bonds (black line) is always smaller than the bond formation without existing bonds (dashed line). (A) and (B) are extracted from [29]. (C) shows the effectiv dissociation rate of an adhesion cluster. The colormape shows the magnitude of the parameter. Within a cluster and surrounded by adhesion molecules the dissociation rate is small. At the boarder the rate increases. (D) shows the association rate for bond formation of free adhesion proteins near the cluster. Due to the reduced height the rate increases in the neighborhood of the cluster. (C) and (D) are extracted from [30]

over the contact area and thermal fluctuations lead to membrane deformation, the stochastical unbinding of adhesion molecules would be able to detach whole parts of the cell-substrate contact area. Instead areas with a high number of adhesion

molecules are expressed by cells to buffer regional fluctuations, bond failure and to transmit forces. Experimental results support a theoretical approach by finding a possible linear relation between the size of adhesion regions and applied loading forces [31]. This section gives an overview of established models to discuss cluster formation and stability under a loading force.

Sunnick *et al.* proposed a model describing the spontaneous cluster formation by considering membrane elasticity and energy stored in bond interaction [29]. The harmonic multispring model (describing each bond as sum over spring constant for membrane and bond elongation) is used to decompose membrane contribution into the summation of the donation of each individual bond [29]. On a exemplary system with two closed bonds as shown in Figure 2.5 (A) the closure of a bond near an existing bond reduces the overall membrane substrate distance and is energetically favorable. A simulations of this model shows on randomly distributed bonds, with a random diffusion of open bonds, the formation of bond cluster [29].

The model proposed by Fenz *et al.* describes the cluster formation of cadherins (adhesion proteins for cell-cell adhesion, bond closure with a cadherin of the opposite cell) through membrane fluctuation which increases the interaction field of the adhesion proteins [30]. The model is based on a harmonic spring model, as described before but with two contributing adhesion proteins. The dynamics of bond formation is described with the effective binding rates, whose rate constants for bond formation and rupture are dependent on regional membrane fluctuation [30]. The membrane fluctuations regulate the binding range of the adhesion proteins but also cause stochastic forces through bond reduced fluctuations on closed bonds. The rates for bond closure and dissociation of an adhesion cluster are shown in Figure 2.5 (C,D). This model shows a dynamical process of bond formation and rupture at the boarders of the adhesion cluster caused by membrane fluctuation with an stable core of low dissociation rate.

In both models, by considering membrane fluctuations on rate equations or energy potential differences under bond closure or rupture result in a favorable bond formation in close vicinity to an existing bond as well as stability of existing bonds at the cluster center. Thus they favor bond cluster formation instead of homogeneous distributed bonds.

Bell first established a deterministic model of an adhesion cluster under constant force [32] to discuss bond stability. Based on Bells approach, Erdmann and Schwarz established a stochastic model which includes fluctuations [33]. The model is based on considering a cluster of $N_0$ adhesion molecules adhering to a substrate with the dissociation rate $k = k_0 e^{F/nF_b}$ depending on the applied force on a single bond $F/n$ and a force scale depending on the thermal energy and an energy barrier to rupture point[33]. The model has the advantage of being able to simulate trajectories of adhesion clusters of a given size under an applied load force, which is shown in Figure 2.6 for different cluster sizes $N_0 = 10, 100, 1000$ and force regimes (A,B).

The cluster trajectories in Figure 2.6 (A) show stable cluster formation for a sufficient number of contributing adhesion molecules ($N_0 = 1000$). The applied loading force is higher a critical value for the trajectories in (B). The cluster constantly

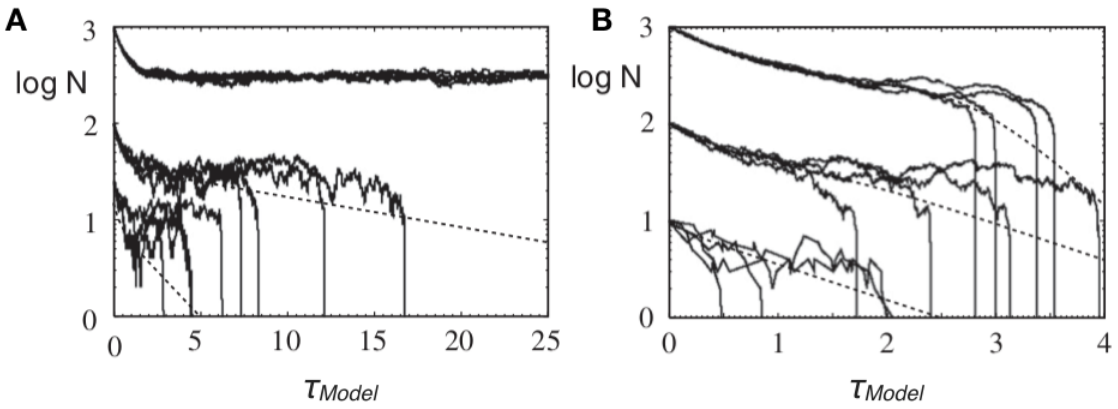


Figure 2.6.: The figure shows simulated results of the stochastic model for the mean number of closed bondes $N$ under different initial conditions. (A) shows 4 trajectories for each of the $N_0 = 10, 100, 1000$ cases with a force per bond lower a critical value. The trajectories shows an unstable regime for smaller cluster sizes ($N_0 = 10, 100$) and a longer lifetime for larger cluster with $N_0 = 1000$. (B) by increasing the force per bond over the critical value also the stable clusters with $N_0 = 1000$ participating proteins becomes unstable and rupture randomly due to fluctuations. Adapted and modified from [33].

dissociate bonds, while small fluctuations increase the load force on the remaining bonds which exponentially increases the dissociation rate and as a consequence leads to a cascade of dissociating bonds and a collective unbinding of the whole cluster [33]. Based on the model it is suggested, that the applicable loading force on a cluster is dependent on the number of adhesion molecules and the bond formation rate until the critical force is reached. At a constantly applied force, the collective unbinding in a rupture event is due to fluctuations.
However, the adhesion of a cluster, is an interplay of a multitude of different adhesion molecules contributing with different bond strengths and repulsive proteins. The simplified models, in comparison to real adhesion cluster, helps to understand the physical background of cluster formation and rupture events and underlines the high dynamics of adhesion clusters.

### 2.3.4. Cell-Substrate Adhesion of *D.d.*

*D.d.* do not carry the genes to express integrins to mediate focal adhesions, do not produce relevant ECM in the single cell state and do not express actin stress fibers. Therefore more fundamental interactions are taking place to provide sufficient traction and be able to adhere onto many different substrates.

### Fundamental Interaction Forces

A theory describing fundamental interaction of colloidal particles was developed by Derjaguin, Landau, Vervey, and Overbeek (DLVO). This theory assumes that the interaction of two interfaces can be approximated by

$$W(h) = W_{VdW}(h) + W_{DL}(h), \tag{2.1}$$

with $W(h)$ the total free energy per unit area depending on the distance $h$ between the interacting surfaces [34]. The two terms contributing to $W(h)$ are $W_{VdW}(h)$, with interactions based on Van der Waals (VdW) forces, which are dipole interactions and $W_{DL}(h)$, the double layer interaction, depending on surfaces charges. A resulting DLVO energy profile is shown in Figure 2.7 (C). This energy profile shows a secondary

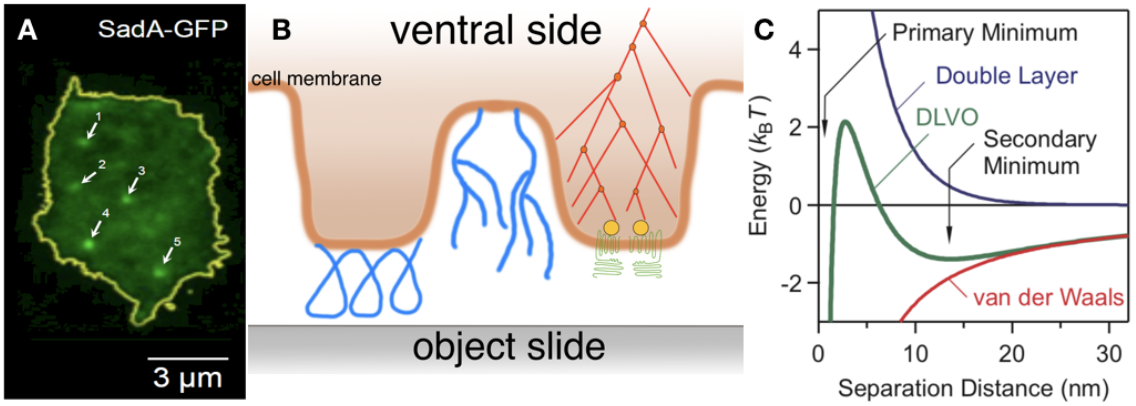


Figure 2.7.: (A) Ventral side of *D.d.* with fluorescencly labeled SadA. Bright spots shows SadA rich areas. Total internal reflection fluorescence (TIRF) method ensures information from the contact area. Extracted from [2]. (B) The figure shows a simplified schematic drawing of the ventral side of *D.d.*. Shown in blue are glyco-proteins interacting as steric repeller and signaling interaction for adhesion. The actin cortex in red, branches with an Arp2/3 complex shown as red dots. This activity is visible as actin foci and supposedly pushes the membrane outward. Adhesion proteins like SadA or SibA, shown in green, are connected to the actin cortex through actin binding proteins like Talin A visualized with yellow dots. (C) DLVO profile for the case of two symmetric surfaces with the same charges. The function starts with the primary minimum, due to the strong VdW interactions for short distances. The repulsive double layer interaction generates a maximum, after which the longer ranging VdW interactions create a smaller secondary minimum. Extracted from [34].

minimum where the VdW attractive term outweighs the double layer term until, for smaller distances, it reaches an energy barrier where the repelling electrostatic

interaction wins. It has been recently shown that VdW forces by glycoproteins play a main role in the adhesion process together with attractive and repulsive electrostatic forces and the hydrophobic effect [2, 35].

### *D.d.* Adhesion Proteins

Many publications address the question whether *D.d.* shows expression of comparable adhesion proteins and formations to mammalian cells while lacking the integrin family of adhesion proteins [2, 8, 36, 37]. The most prominent adhesion proteins are the three transmembrane proteins SadA, SibA and Pgh1A. SibA shows similarities to the mammalian integrin $\beta$, as for example both have a cytosolic domain interacting with talin [38]. A knock-out of Pgh1A and SadA, proteins with nine transmembrane domains each, results in a strong defect in SibA localisation at the membrane [36]. Fluorescence labeled SadA reveal spots of higher SadA concentration on the ventral side of the cell as shown in Figure 2.7 (a), while these clusters colocalize to 96% with actin foci [39].
It was found that, the membrane is closer to the substrate at the area of the actin foci, and thus probably forming some "feet-like" structure. Also traction forces are transmitted in areas near actin foci, what suggestes the involvement of these foci in transmitting forces [18]. *D.d.* express clusters of adhesion proteins which show similar behavior to focal adhesion in case of the collective unbinding of adhesion molecules under a loading force [2]. It was shown that talin links SibA to the actin cortex and that this link is necessary for retraction of the uropod [17]. A schematic visualzing a possible formation of an actin focus is shown in Figure 2.7 (b). These clusters are long lived contacts which ensure the attachment of the cells even after the majority of the contact area is detached. Further, it provides contact under traction forces that enables movement.
To summarize, it should be mentioned, that by lacking interaction partners, the adhesion proteins interact with the substrate. These interactions, e.g. VdW and electrostatic interactions are strongly distance depended. To overcome the repulsive interaction, provided by the cell to distance them self from the substrate for undefined short range interactions, the cell produces feet like structures to decrease the distances to the substrate. I believe that a high concentration of adhesion proteins is located on this feet. Variation in salt concentration influences the electrostatic interaction. Interestingly, by applying a detachment force on a cell in a medium of higher salt concentration, the distance after which the cell is detached from the substrate is decreased [2]. A possible explanation can be that with increasing salt concentration, the extent of the attractive part of the peak-like potential in the energy-separation-curve decreases. A small separation increase would lead to a faster shift into the repulsive regime and thus to the detachment of the adhesion cluster.
At higher developmental stages of *D.d.*, the cells down-regulate the expression of SadA and SibA and reduce adhesion strength to possibly gain an increased motility [8].

# 2.4. Clathrin

## 2.4.1. Clathrin Structure and Assembly

An assembled clathrin protein, also called clathrin triskelion, is composed of three 190-kDa heavy chains (chc) and three 30-kDa light chains (clc) as shown in Figure 2.8 (B) [40]. The three chc assemble on their C- terminus and spread as legs from

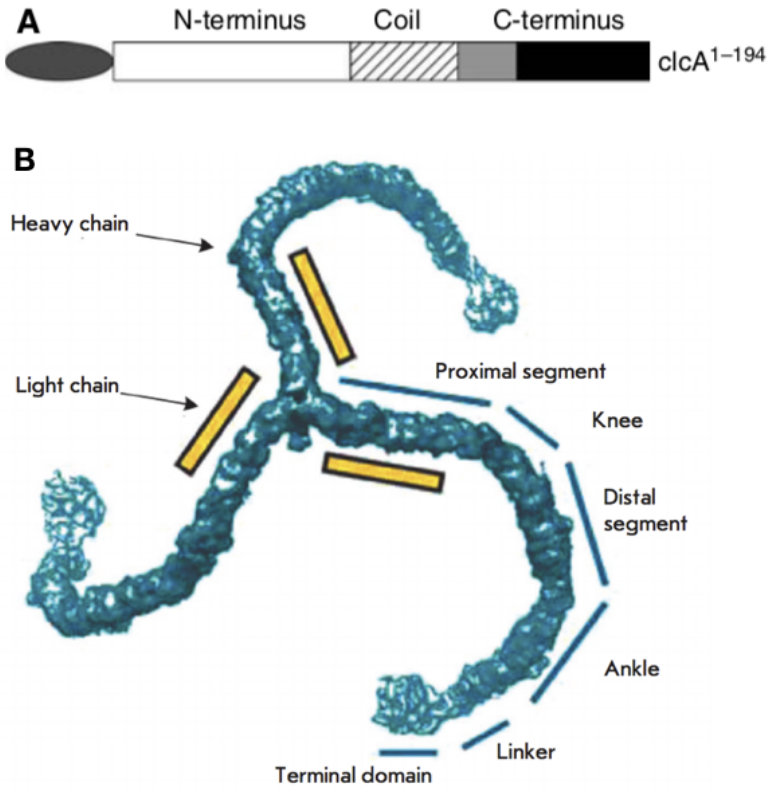


Figure 2.8.: (A) shows the clcA with 194 amino accids. The light chain consists of three segments. The carboxy (C-) terminal is critical for the light chain function and contains the heavy chain binding region as a part of the black marked region. The coiled domain is involved in binding to the heavy chain by augmenting the interaction region. The fluorescence protein (black oval) is fused to the amino (N-) terminal. From [41].
(B) shows the assembled clathrin triskelion. The segments of the heavy chain are labeled, the interaction region of the light chain is visualized with the yellow box. The chc are connected at their C- terminal on the inside. The terminal domain contains the N-terminus and binding domains for adaptor proteins. Adapted from [42].

their centered position. The chc interact with the legs of other triskelion by their proximal and distal segments [43]. The length of the triskelion legs was determined for *D.d.* and is $48 \pm 5$ nm [40]. The light chain is composed of three regions, the

N-terminus, C-terminus and a coil in the center. For *D.d.* cells, the C-terminus is responsible for binding to the proximal segment of the chc, and the coiled domain augments the interaction. A knock out of the N-terminus, shows no difference in the phenotype and has therefore a minor influence [41]. Endocytosis, growth and osmoregulatory defects were found for *D.d.* in the vegetative state for a heavy chain knock out [44]. Whereas developmental defects were found under starvation [45]. In comparison to the heavy chain, the light chain knock out also shows defects in osmoregulation, cytokinesis and developmental defects, while they show similar growth and fluid-phase endocytosis rates compared to wild-type cells [46]. Also, triskelions of *D.d.* can still be formed in absence of the clc, but their ability of binding and assembling onto the membrane is strongly reduced [46]. This implies that the light chains take over regulatory functions and are presumably involved in the geometrical structuring of the heavy chains.

### 2.4.2. Clathrin Mediated Endocytosis (CME)

The CME describes the invagination of the plasma membrane, forming a pit, which is pinched off for internalization and further processing. Therefore it is used for nutrients and signaling molecule uptake and is the main route for receptor internalization for mammalian cells. Clathrin itself is not able to bind to its cargo and depend on adaptor proteins like, AP2 or DAB2, for sorting and interaction. These adaptor proteins can be considered as hubs, which link a particular cargo protein or the membrane to the N-terminus of the chc [47]. Thereby, clathrin assembles on the membrane into a polyhedral lattice comparable to a mesh. The activitiy of WASp induces the CME by activating the Arp2/3 complex [48]. By utilization of the actin cortex, the clathrin coated membrane is bend inwards and in later steps, the engulfed cup is transported away from the plasma membrane. The sequence for CME is shown in Figure 2.9 (B), a model to explain membrane invagination through actin activity is shown in the sub-figure. For more information about clathrin coat behavior see section 2.4.3.
Supported by the branching actin network, the clathrin pit is further engulfed into the membrane until it is pinched off. The clathrin coat serves as a scaffold by shaping and stabilizing the vesicle. The clathrin scaffold of a vesicle is shown in Figure 2.9 (A). The CME vesicles can vary in their diameter depending on the species, ranging roughly from $30 - 200$nm [49]. The diameter for example was estimated as 50 nm for *D.d.* from fluid uptake [50]. The differences in the diameter can be achieved by different lattice formations [42].
The process of *D.d.* CME has many similarities in its kinetics to CME of mammalian cells. For example, this is visible through the existence and recruitment of AP2 protein as a linker between transmembrane proteins and clathrin. The AP2 is homologous to mammalian cells and their presence is sufficient to form clathrin coated pits, but not essential, hinting at the presence of unknown interaction partners [51]. WASp is also recruited to the clathrin coat of *D.d.*, which activity is a marker

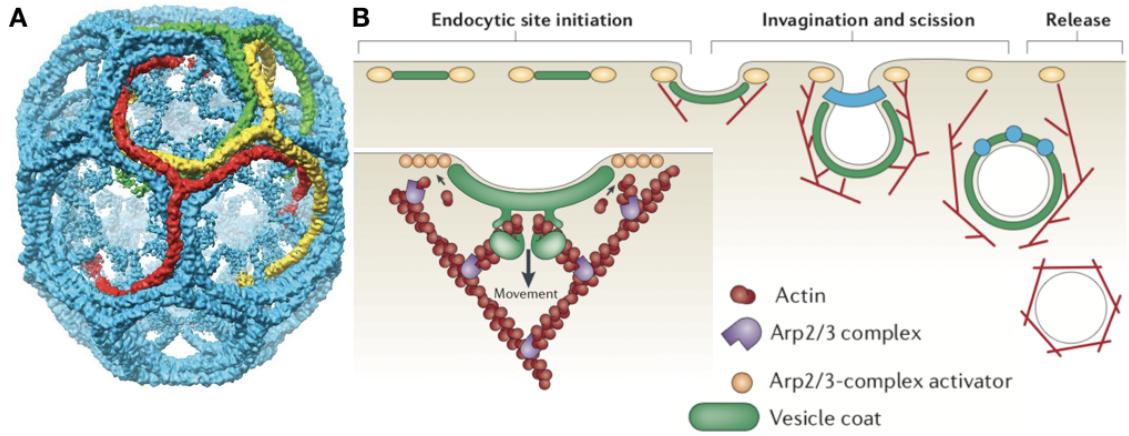


Figure 2.9.: (A) shows an example for clathrin cage formation, formed by 36 clathrin triskelion with a resolution of 0.79nm. To visualize the interaction regions of different triskelion, three clathrins are colored, clc are not shown. In this case, a clathrin triskelion (red) interacts with its next neighbor (yellow) by their proximal segment. This segment again interacts with the distal segment of the after next triskelion (green). The terminal domain is oriented to its membrane interaction partners inside. Adopted from [42].
(B) Schematic drawing of clathrin mediated endocytosis. A clathrin coated structure sits on the plasma membrane, colored in green. WASp proteins shown as yellow dots activate branching of actin cytoskeleton, shown in red, through interaction with the Arp2/3 complex. The clathrin coated membrane cup invaginates. The proteins involved in the scission process are shown in blue. The engulfed vesical is transported away from the membrane, the clathrin coat is dismantled and further processed. (B) sub-figure shows a possible way to model the membrane invagination by actin activity. The activated Arp2/3 complex branches the actin network which pushes against the plasma membrane. By a connection between clathrin lattice and actin network and further polymerization around the coated clathrin pit, the membrane bends inward and forms a cup. (B) and its sub-figure are extracted from [48] and modified.

for beginning CME [52]. Furthermore it was shown that dajumin, a transmembrane proteins is internalized by CME [51] and thus shows CME as a possible path for transmembrane protein internalization also for *D.d.*. Recent studies have shown the involvement of I-BAR in CME for *D.d.*, also in accordance to mammalian cells. The I-BAR protein is used for membrane curving of filopodia and lamellipodia. Furthermore, it is colocalized with clathrin spots and thereby may support the pinch-off, by stabilising the point of inflection of the curved membrane for CME [53]. This

accordance suggests an early development of the CME process in evolution.

### 2.4.3. Clathrins Involvement in Adhesion.

As mentioned before, CME transports receptor cargo from the plasma-membrane and can therefore fulfill regulatory purposes. It has been shown that the CME is one of the major internalization routes for membrane and especially proteins, for example integrin in mammalian cells. This serves several purposes. By the engulfment of integrin the ECM is involved in the regulation and disassembly of adhesion complexes like focal adhesion and thus affects the cell motility and its interaction with the substrate [54, 55]. By reduction of inactive integrins, it ensures integrin recycling and their internal transport for the next use [55]. The targeted reduction of active integrins in focal adhesion spots, can for example reduces the adhesion strength of a spot.
Different adaptor proteins fulfill different purposes of application. The NUMB protein for example promotes migration by regulating the internalisation at the leading edge or the involvement of the AP2 and DAB2 protein for the internalisation of inactive integrin at the dorsal side of the cell [55].
Different models for the creation of the curvature to form a clathrin cup where proposed. For a more precise discussion of alternative models see [56]. The different models are based on two opposing assumptions. On assumption is that the clathrin triskelion assembly curves the membrane and thereby forms the pit. The other assumption is that clathrin assembles as plaque on the membrane and the pit formation is induced. An approach producing clathrin vesicles with minimal components showed that clathrin assembles at liposomes covered with adaptor proteins in flat hexagonal structures at 4°C. A temperate transition to 37°C activates the assembly of a clathrin vesicle [57]. This shows, that the activation and assembly of clathrin is sufficient to form vesicles *in vitro*. However *in vivo* experiments revealed a strong dependence on the membrane tension, where e.g. cargo interaction hinders pit formation in absence of actin. The involvement of the actin-cortex can overcomes the energy barrier arising from possible cargo interaction or membrane tension and further drive the CME [58].
The clathrin coated structures (CCS) are long-lived platforms dependent on integrin formation and it was suggested that they are used to sense substrate rigidity [21]. This shows that the involvement of adhesion proteins causes an obstruction which leads to an endocytotic delay. The size of CCS increases with more rigid material and they serve as a signaling platform [21].

#### Clathrin Involvment in *D.d.* Adhesion

The absence of integrins for *D.d.* raise the question whether similar or rudimentary mechanisms exist which involve clathrin in the adhesion process. It has been shown that more then 80% of actin foci appear at the position of a clathrin foci [59]. Consequently, actin foci appear independently of clathrin structures but the

majority of foci are colocalized, while the clathrin foci, which are also referred to as clathrin puncta, appears a variable time period before the actin foci. For example an appearing clathrin foci can be detected in order of tens of seconds until WASp activity induces the CME [14]. While Heinrich *et al.* exemplary show the appearance of a clathrin foci 17s before the actin foci maximum and that with increasing actin activity, as well as the also tracked Arp2/3 complex and other actin foci related proteins, the clathrin intensity decreases [59]. Furthermore for an analysis of clathrin and actin appearance with detected height changes, the mentioned colocalization of actin and clc foci could also be detected to 86% by increasing the observation time window to three minutes [39]. The analysis of the height changes revealed a membrane height change towards the substrate with increasing clc intensity at the same area. With occuring actin foci the clc intensity decreases and with resolving actin patch the membrane-substrate increases again [39]. The detected height change with occuring clathrin activity paired with the high correlation with actin foci as proposed adhesion cluster, strongly suggests the involvement of clathrin in the adhesion process. While the slightly delayed disappearance with the actin foci indicates a CME. The observed height change in combination with the variable time that a clathrin foci is present before an actin activity initiates its disappearance, indicates a possible clathrin based adhesion cluster. It is possible that despite the shown differences in the adhesion process to higher eukaryotic cells a comparable mechanism of CCS is already present in the adhesion process of *D.d.*.

## 2.5. Metal-Induced Energy Transfer (MIET)

To investigate the cytoskeletal structure during cell adhesion it is useful to achieve height information with an high axial resolution. With the spatial resolution of 250 nm and a height resolution of up to 3 nm accuracy, it is possible to determine the shape, for example of the cell membrane and, by dual labeling, set it in relation to other proteins. A new microscopy method which provides this resolution is MIET. A fluorescent molecule is excited by absorbing a photon of a defined wavelength. This transits the molecule to a higher energy level $S_1$. To transit back to the ground state $S_0$, the excited molecule can spontaneously emit a photon of a larger wavelength as shown in Figure 2.10 (A). This wavelength change is due to energy dissipation of non radiative transistions. Another possible interaction to transit into the ground state is named after the germane physicist *Theodor Förster* [60], the Förster resonance energy transfer (FRET). In this case the excited fluorescent molecule, called donor, can transfer the energy to another molecule, the acceptor. The jablonksi diagram in Figure 2.10 (A) illustrates a possible FRET. The energy transfer only occurs if these molecules overlap in their emission and absorption spectra. The efficiency of the energy transfer strongly depends on distance and orientation between both molecules. The efficiency is defined as the quantum yield $\phi = \#_{se,a}/\#_{a,d}$, as the relation between $\#_{se,a}$ number of spontaneous emission by the acceptor and $\#_{a,d}$ number of absorbed photons by the donor [62]. The loss of energy either induces

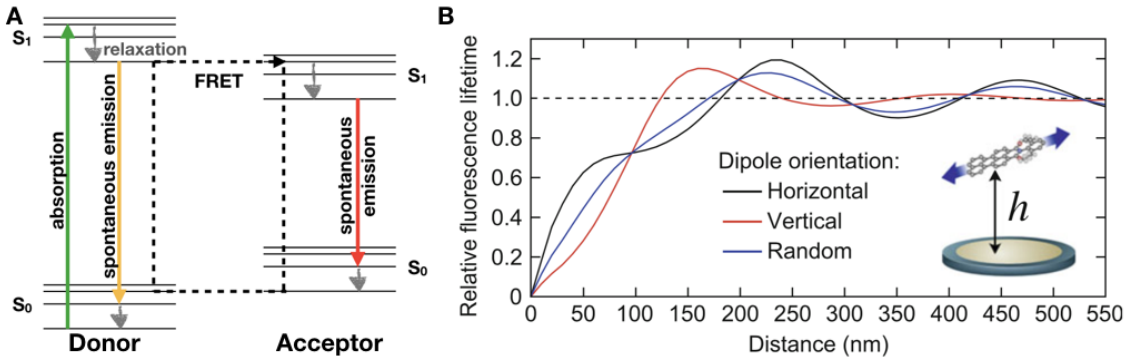


Figure 2.10.: (A) Jablonski diagram for a possible FRET transition. The donor absorbs a photon of a defined wavelength and is transferred to an excited state. Instead of a spontaneous emission, the energy can be transfered to an acceptor. The wavelength change is due to relaxation to the lowest vibrational level of the state. (B) Relation between the relative fluorescence lifetime and the distance $h$ between the fluorescence molecule and the metal layer. The curves are calculated for a vertical dipole orientation (red), a horizontal orientation (black) and a random distributed dipole orientation (blue). The metal for this example is a gold layer with a thickness of 20 nm, while the metal layer used in this work has a thickness of maximal 15 nm. The emitted wavelength of the fluorescence molecule is 650 nm. From [61]

a shortening of the donor's fluorescence lifetime, or in case of an efficient energy transfer, enables the acceptor to radiate light of a longer wavelength. The measured effect can be converted to the distance between the molecules, what enables for example the detection of relative distance changes between donor and acceptor in biological processes [62].

By using the basic principles of FRET, MIET describes the interaction between an excited fluorescent molecule (donor) and a thin metal layer (acceptor). The fluorescent molecule interacts with surface plasmons, consequently the electron cloud of localized electrons in the metal layer, whereby the dissipating energy of the interaction results in a shortening of the fluorescence lifetime [63]. Similar to FRET, the effect is a near-field interaction, depending on distance and orientation of the molecule. The quantitative understanding of MIET allows us the transformation of the lifetime change into a relative distance between the molecule and metal layer [64, 65].

The following part gives an insight into the theoretical approach and acts as a short summery of the theory part of the review [63]. The fluorescence molecule can be described as an emitting ideal electric dipole. The basic idea is to compute the interactions between dipole and metal layer. Therefore the electromagnetic field of the dipol is determined by solving the Maxwell equations [63]. By knowledge of the

electric field, the total emission per unit time can be calculated as:

$$S(z,\alpha) = S_{\perp}(z)\cos^2\alpha + S_{\parallel}(z)\sin^2\alpha \tag{2.2}$$

with $S_{\perp,\parallel}$ the emission functions for perpendicular/parallel dipole orientation to the surface, computed by the mentioned field. The dipole orientation is defined by an arbitrary angle $\alpha$ and $z$ is the height difference to the surface [63]. In the next step, the relation between a perturbed fluorescence molecule and its unperturbed state is calculated. Therefore, the relation of the average fluorescence lifetime $\tau_{MIET}$ to the unperturbed lifetime $\tau_0$ is given by

$$\frac{\tau_{MIET}(z,\alpha)}{\tau_0} = \frac{S_0}{\phi S(z,\alpha) + (1-\phi)S_0}, \tag{2.3}$$

which is additionally depending on the quantum yield and the unperturbed emission rate $S_0$ [63]. The calculated relation between distance and relative fluorescence lifetime is shown in Figure 2.10 for different dipole orientations. The interaction shows a monotonous relation between 0 and 120−180nm above the surface depending on dipole orientation. The function shows an oscillation around the relative fluorescence lifetime marked by the dashed line. The minimum of this oscillation marks the end of the monotonous relation and the region with no distinct solution due to the oscillatory behavior.
For labeled proteins like actin, the fluorescence proteins are randomly oriented. The focus point, to excite the proteins, contains ideally more than one protein and is measured multiple times, for more information on the method see section 3.3.2. Therefore the dipole orientation can be assumed as random and an orientation detection is not required.

# 3. Material and Methods

## 3.1. Cell Strains and Culture

### 3.1.1. Cell Culture

The NC4-A2 cell strains used for this work grow axenically, thus the medium contains no other living organisms to feed on, but instead they are cultured in a growth medium called HL5 (ForMedium™,UK). A protocol for *D.d.* cell culture is provided by *P. Fey et al.*, which gives deeper insight into the preparation and storage of *D.d.* and is referred to for more information [66].
The cells are stored as spores or amoebae, frozen at -80°C for longer time periods. Before usage the cells are defrosted at room temperature. The axenic strains are afterwards cultured in HL5 medium on a Petri dish. The optimal cell growth can be achieved in a temperature range between 21 and 23°C, while temperatures higher than 25°C will prevent growth. Cell doubling under ideal condition is 8 to 12 hours for the axenic strains. The cells show an exponential growth until a limiting cell concentration of roughly $4 \cdot 10^6$ cells $ml^{-1}$ is reached. To ensure a constant maximal growth rate, the cell culture is splitted and diluted into subcultures every 2 to 3 days. The passage number states the number of subculture splits the cells have undergone. To ensure a low probability for unwanted mutations, the culture is discarded after passage 15.
This work is focused on undeveloped, vegetative *D.d.* cells as shown in the vegetative cycle in Figure 2.1. At this state, with freshly removed nutrient solution, the cells move in a random-like manner and thereby express random adhesion regions. Under starvation the cells switch into the developmental stage and thereby undergo changes leading to chemotactic competence, reducing cell adhesion and show a directed movement. To exclude cells undergoing this switch in adhesion behavior, the measurement time is limited to 3 hours after removal of the HL5 medium.

### 3.1.2. Cell Strains

The genome of *D.d.* is haploid and thus genetic modifications, e.g. by knocking out or tagging proteins with a fluorescent label, can not be masked by the second genome as it is the case in diploid cells. With the SCFS measurement, clathrin light chain knock out cells (clc-) are compared to their wild type cells, the NC4-A2 is in the following refereed to as WT NC4A2. For the SCFS measurements, cells without fluorescence labels were used to avoid a possible influence of the labels on the adhesions process [68].

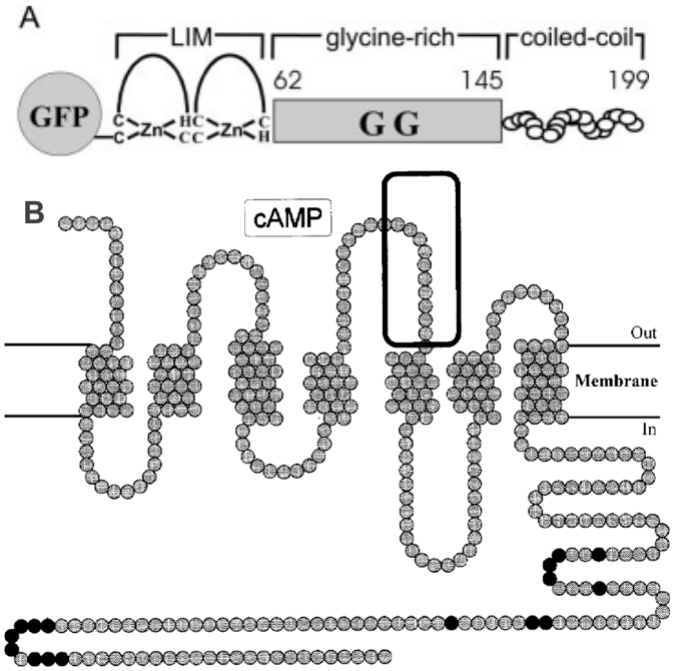


Figure 3.1.: Schematic drawing of (A) LimE protein. LimE is coposed of three regions, the number are referring to the bounding amino acids position. The fluorescence protein is fused to the N- terminal Lim domain. For LimE$\Delta$coil the C- terminal coiled-coil was removed. The combination of Lim domain and the glycine-rich area ensures the function in case of its localisation. Extracted from [67]. (B) shows structure of the transmembrane protein and major cAMP receptor carA. The scheme visualizes the intra- and extracellular regions of the protein. The black box comprises the major amino acids for cAMP affinity. The fluorescence label is tagged on the C- terminal inside. Extracted from [9]

To gain height information with the MIET method, specific proteins are genetically fused to fluorescence proteins. The carA protein is the primary cAMP receptor for *D.d.* and activates pathways affecting the actin activity. The labeled version shows an even distribution on the cell membrane for developed cells [69], but it was shown also to be active in the vegetative state [7] and therefore is ideal for membrane tracking. A fluorescence protein is fused to the C- terminal [69] in the inside of the cell as shown in Figure 3.1 (B). Therefore the obtained fluorescence signal is slightly above the cell membrane. For clathrin labeled cells, the fluorescence molecule is fused to the N-terminus of the clcA as shown in Figure 2.8 (A). It was shown, that the phenotype is reinstored by the expression of fluorescenct labeled clcA on clc- cells [41].
To detect actin foci, a globular actin label would be visible as a superposition of

the actin cytoskeleton and cytosolic actin [70]. The LIM domain-containing protein LimE operates at the actin cortex and is colocalized to freshly polymerized actin. The indirect LimE label improves the visualization of active actin regions such as actin foci and thereby reduces the background activity, which would be visible as noise. It is comprised of a glycine-rich region between the N-terminal Lim domain and the C-terminal coiled-coil domain, which are schematically shown in Figure 3.1 (A).
Label combinations used for MIET measurments are: clc- + pAL 05 pDM115 LimE-GFP, clc- + pAL 05 pDM115 LimE-GFP + mRFPmars- clc in pDEXH (518-7 in 338-19) and pAL 05 pDM115 LimE-GFP + carA-mCherry (pDM101) are used. The clc in pDEXH (518-7 in 338-19) was provided by the group of A. Müller-Taubenberger and carA-mCherry (pDM101) by the group of P. N. Devreotes.

### 3.1.3. Cell Preparation

To prepare the cells, the nutrient solution is removed from the subculture. Afterwards the adherent cells are washed from the petri dish with a phosphate buffer (PB, 2 g/L $KH_2PO_4$ + 0.36 g/L $Na_2HPO_4$ at pH 6) and filled into a flask where they are centrifugalized with the 5810R centrifuge from *Eppendorf*, with 1000 rpm for 3 minutes at 4°C. The remnant buffer is removed and the *D.d.* pellet is washed in PB, following the same procedure. Afterwards the cell pellet is solved in 20ml of fresh PB. The cells are counted and afterwards diluted to the desired cell concentration. A concentration of $3x10^5$ cells per ml has turned out to be preferable for easy handling by SCFS and MIET measurements.

## 3.2. Single Cell Force Spectroscopy (SCFS)

The adhesion strength is measured by applying an external force to a cell and quantifying their adhesive interactions. It can be differentiated between methods applying shear forces through an external flow and methods applying a pulling force. Typical examples for shear force assays are the washing assay, spinning disc assay or flow chambers. These assays determine the ratio of detached cells to an initial number of attached cells for a given external flow. The resulting adhesive strength can be estimated because applied shear force depends on cell shape, size and contact area [71].
The SCFS assays are based on detaching a single cell from a substrate by applying a pulling force and measuring the opposing force. There are different options to initialize SCFS for example by micro-pipette aspiration, optical tweezers or Atomic Force Microscopy (AFM). The AFM based method provides the largest range of applicable forces (up to 100nN) and also the largest spatial movement (up to 100$\mu$m) with a sensitivity to detect forces starting from 10pN [71]. It is thereby best suited for the measurements of this thesis, because it can detect molecular interactions of adhesion clusters and the overall adhesion force of the whole cell.

### 3.2.1. Atomic Force Microscopy (AFM)

The physical principle of an AFM is based on Hooke's law. A thin lever arm called cantilever approaches a sample. Upon contact with the sample the cantilever bends and exerts a force proportional to the bending of the cantilever on the sample. By measuring this bending behaviour, the AFM can measure forces, penetration depth for a defined force, or scanning the surface by determining the height of the cantilever while moving it over the surface to create a $3D$ image.

The AFM used for this work is a MFP-3D™ from Asylum Research with a 30 micrometer z-range [73] mounted on an Olympus microscope (IX71, with 40x objectives) and a CCD Camera (ANDOR Zyla 4.2 sCMOS) for optical control. The operating principle is explained in the following.
The method used in this work for force detection is called the optical lever detection. The cantilever is positioned with an angle of 11° to the substrate and a light beam emitted by a laser is focused on the reflective back of a cantilever tip region. The reflected light follows the light path visualized in Figure 3.3 (A) and is focused in the middle of a four quadrant photo detector as shown in Figure 3.2 (B). The interaction between cantilever and substrates leads to bending of the cantilever which deflects the reflected light from the neutral position as shown in Figure 3.2 (A). Through the length of the optical path, the difference from the neutral position is amplified which enables the resolution of even small interactions. The bending of the cantilever results in a vertical shift of the focus point at the photo detector called vertical deflection which is shown in Figure 3.2 (B,right) and is referred to in the following as *Deflection*. The cantilever can twist which creates a horizontal shift of the focus point called lateral deflection which is shown in Figure 3.2 (B,left) and

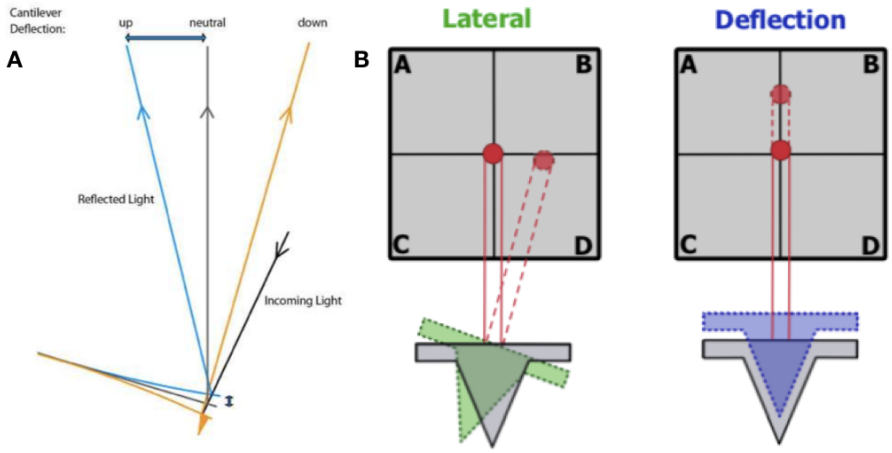


Figure 3.2.: The schemetics show in (A) the light path of the unperturbed cantilever in the neutral position and the change due to bending of the cantilever. (B) Four quadrant photo detector with the focus point of the reflected light beam positioned in the middle (in red). The height change is measurable as a shift in the vertical axis, called *Deflection* (right image). Also a twisting of the cantilever is possible, which is detectable as shift in the horizontal axis on the photo detector, called *Lateral*. From [72]

is referred to in the following as *Lateral*.
The photo detector is segmented to four quadrants (A,B,C and D) arranged as shown in Figure 3.2 (B). The voltage generated at each quadrant is proportional to the amount of photons hitting the respective quadrant, thus the resulting *Deflection* is set as the voltage difference between the upper ($V_A + V_B$) and lower part ($V_C + V_D$) of the detector and the *Lateral* as the difference between the left ($V_A + V_C$) and right ($V_B + V_D$) quadrants of the detector [73].
The optical units for the cantilever detection are mounted on the Z-Stage as shown in Figure 3.3 (A). The Z-Piezo/NPS unit (Figure 3.3, green) enables a controlled movement of the Z-Stage and thereby the cantilever. Following the piezoelectric effect, those units change their length in response to an applied voltage. Due to the non-linearity of the piezo over its movement range, the caused misalignment is adjusted by nano-positioning system. The MFP-3D™can move in x- and y-direction, which is build by similar units. For more information on the AFM method and its functions, see [72, 73].

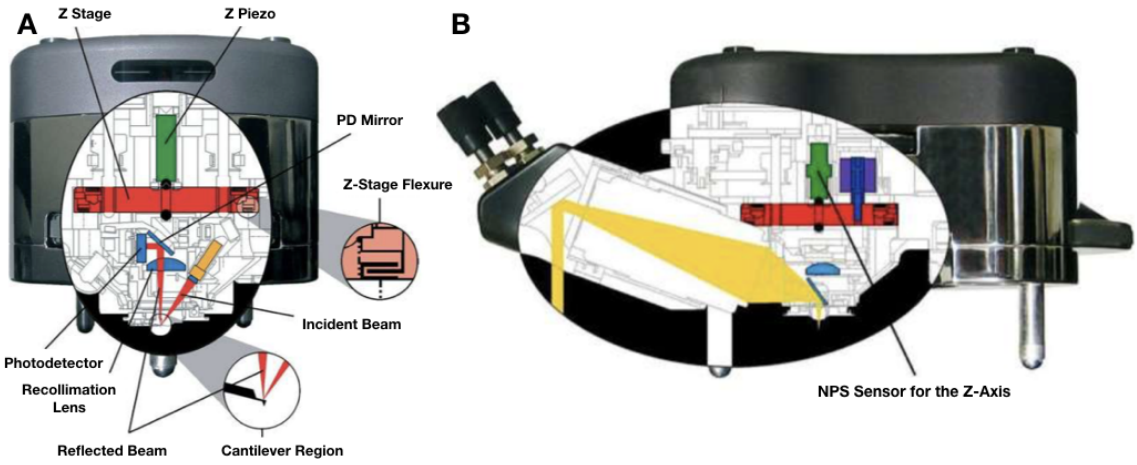


Figure 3.3.: Schematics of the AFM head used for the experiments. (A) shows the front view. The optical path is placed in the lower part of the head. A Piezo for the z direction (green) is build above the z stage (red) and moves the whole optical object with the cantilever. (B) shows side view with a unit measuring the exact position of the z stage called Nano-Positioning System (NPS™). The light path of the background light and microscope is colored in yellow and can be adjusted by setting screws (left side of B) which change the mirror position. From [73].

### 3.2.2. Calibration

Cantilever differ in their parameters like size, geometry, spring constant or tip size. These parameters change the resulting movement of the focus point on the photo detector and thus the voltage difference. By performing a force curve on a hard substrate, like a cover slide, the cantilever *Deflection* can be determined for a defined voltage difference of the detector ($\Delta U = 1\text{V}$), what is called sensitivity $S_{pd}$. With the sensitivity and the spring constant $k$ the instantaneous voltage difference $\Delta U$ can be calculated to the resulting force $F(\Delta U)$, following Hook's law, with

$$F(\Delta U) = -kS_{pd}\Delta U. \tag{3.1}$$

The spring constant of the cantilever is roughly defined by the producer. The precise spring constant is determined by the thermal noise method in liquid. For this means the AFM software provides a tool which measures thermal noise upon each experiment by the user. The applied equipartition theorem set the thermal energy in relation to the oscillation energy which enables the calculation of the spring constant [74]. A torsional moment on the cantilever tip creates a lateral shift at the photo detector, as mentioned before. The spring constant ratio between lateral $k_L$ and normal direction is roughly given by $k_L/k = (L/H)^2$ [75], with $L$ the length of the cantilever and $H$ is the height of the tip or in case of SCFS methode approximately the height of the cell. As the lateral spring constant is many times larger than the

normal spring constant, torque due to not centered contact at the cantilever tip is neglected. For more information on the calibration process see [73].

### 3.2.3. Experimental Setup of AFM based SCFS

As mentioned before, the AFM based version of SCFS provides a large range of applicable forces. On one hand, it can resolve the interactions of adhesion clusters. For example it gives information on the contribution specific proteins play for the adhesion process through comparison between knock out (KO) and wild type (WT) cells. On the other hand, it can detect the overall adhesion strength from the cell. Thus, the method is ideal to investigate the adhesion process of *D.d.*.
The SCFS is performed with tipless cantilevers (Arrow™ TL2, NanoWorld, typical spring constant $k = 0.03$ N m$^{-1}$). To ensure the cells stay attached to the cantilever and detach from the substrate instead, cantilevers are functionalized with CELL-TAK™. CELL-TAK™ is a commercially available polyphenolic protein extracted from the mussel *Mytilus edulis*. *D.d.* attached to tip of the cantilever coated with CELL-TAK™ show an increased cell attachment in comparison to uncoated cantilever and to the substrate by up to a factor of 10 [8]. For more information on handling of CELL-TAK™ see [76].
To prepare for the experiment, the object chamber is assembled and a calibration is performed in a phosphate buffer. Afterwards the cells need $20 - 30$ min time to sediment and adhere to the substrate.
A chosen adherent cell is picked with the cantilever tip. For this the cantilever gently pushes on the cell with 1nN for 60s. This gives the cell a chance to adhere to the functionalised cantilever tip, before lifting the tip at $1\mu$m s$^{-1}$ and detaching the cell from the surface. The success of the picking process is confirmed through optical feedback, like the cell attached to the cantilever is shown in the sub-figure 3.5 (C) in top view. After picking the cell up it is allowed a time period of 2 min to establish a stable adhesive connection before the measurement cycles starts.
A new position free of other cells, cell debris or proteins is chosen on the cover slide to ensure an unbiased movement. To record the force curve, the cell is passing through the measurement cycle as shown in Figure 3.5 (A) with the preoptimized parameter [8] listed in Table 3.2.3. The cycle begins with surface approach and a

| Parameter | Value |
|---|---|
| contact force $F_{con}$ | 0.5nN |
| approach velocity $v_r$ | $2.5\mu$m s$^{-1}$ |
| contact time $t_{con}$ | 30s |
| retraction velocity $v_r$ | $2.5\mu$m s$^{-1}$ |
| Sample rate | 5000Hz |

Table 3.1.: Single Cell Force Spectroscopy Parameters used in this Work with MFP-3D™.

light push with the constant contact force $F_{con}$ onto the glass substrate for a defined contact time $t_{con}$. During this time, a picture is recorded with the mounted camera to verify the cell-cantilever-substrate contact at the cantilever tip. The cycle closes with the retraction and detachment with a constant retraction speed. After $30 - 60$ s recovery time, the cell is ready for the next measurement cycle.
After each repetition it is useful to check the cell attachment to the cantilever. To prevent the cells from adapting to the applied routine, the record limit is set to 10 curves per cell. When the limit is reached, the cell is washed from the cantilever by the surface transition from buffer to air for several times. To ensure that *D.d.* cells are at the vegetative stage, the maximum measurement time is 3 hours beginning with the removal of the nutrition solution in the lab.
The measurable cell-substrate adhesion strongly depends on the applied parameters

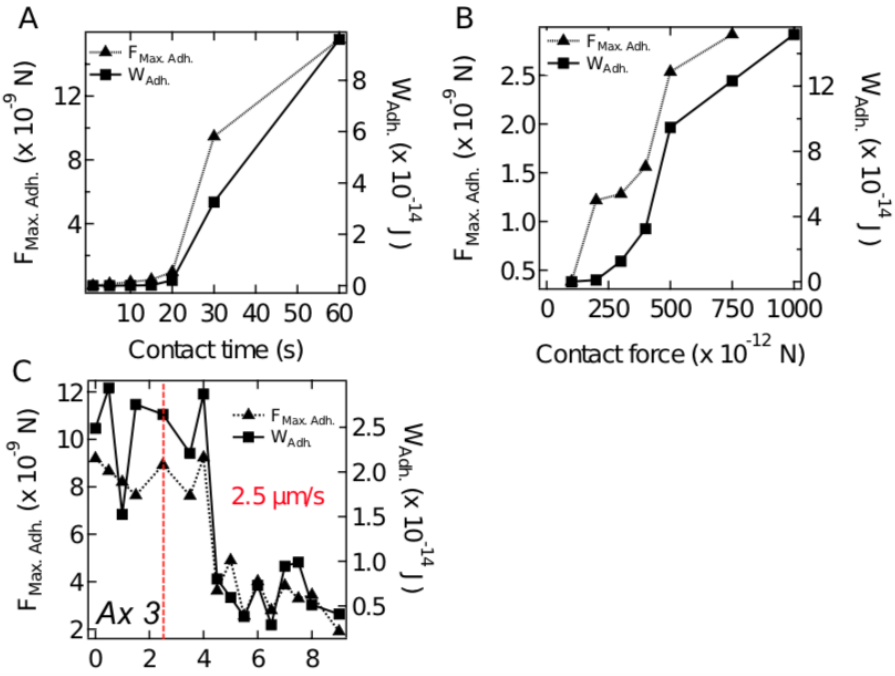


Figure 3.4.: Parameterization of SCFS parameter. Each sub-figure shows trajectories for maximum adhesion force ($F_{Max}$) (dashed line) and adhesion work ($W_{Adh}$) (solid line) for the parameters contact time $t_{con}$ (A), contact force $F_{con}$ (B) and retraction velocity $v_r$ (C). From [8]

as it is shown in Figure 3.4. An increase of $F_{con}$ can enlarge the contact area and therefore probably increase the cell adhesion [71]. The contact time is the time period of cell interaction with the substrate. For mammalian cells small, new formed integrin cluster were detected within seconds to minutes [77], which suggests an active rearrangement of the contact area to form adhesion clusters. An increase in contact time would lead on one hand to stronger cell adhesion with the substrate but on the other hand could increase the possibility of detachment and movement away from the cantilever [78]. The retraction speed $v_{rs}$ of the cantilever influences

the loading force applied to the adhesion molecules [78]. Therefore an increase in $v_{rs}$ leads to faster detachment of single adhesion molecules and increases the load applied to the remaining adhesion clusters. In case of slip bonds, two clusters with roughly the same number of contributing adhesion molecules would detach, more likely at the same time and thereby influence the resolution of the resulting force-curve.
$F_{con}$, $t_{con}$ and $v_{rs}$ values were chosen for *D.d.* AX3 cells on the basis of a parametrization [8] which is shown in figure 3.4. Whereby the choice of $t_{con}$ was influenced by the time of new actin foci creation with an half-lifetime of $10 - 15$s [18]. The retraction speed was chosen with a buffer to $4\mu$m s$^{-1}$, where a decrease in adhesion force and work was detected. $F_{con}$ was chosen closest to non-invasive, where an approach to the cell-substrate contact is ensured. For comparability's sake the parameters in this work are of the same values as earlier publications [2, 8, 39].
Next to the influenceable parameters, the cells vary in their size and viscoelasticity which results in different projected contact areas [78]. Therefore the recorded image is analysed to determine the cell diameter during substrate contact.

### 3.2.4. Analysis of SCFS force curve

An exemplarily chosen force-distance curve (FDC) is shown in Figure 3.5 (B) with corresponding phases of the measurement cycle shown in (A). A customized *MATLAB* script is used for the retrace-curve analization. An overview about the extracted parameters from the retraction curve is given in the following segment.

*Maximum adhesion force ($F_{Max}$)* :
By retracting the cantilever, the detected force decreases until it reaches a minimum, called $F_{Max}$. Up to this point the whole contact area is contributing to the cell attachment. $F_{Max}$ is therefore the highest achievable adhesion force for the cell, before rupture events occur and the detected retraction force approaches the base line.
*Adhesion Work ($W_{Adh}$)* :
The adhesion work is determined by the integral between FDC and the zero force line. It is defined as the energy dissipated during the retraction process [71]. Also the cell-body deformations and membrane tether are contributing to $W_{Adh}$, besides the number of adhesion foci and the adhesion proteins involved.

*Step properties* :
After $F_{Max}$ is exceeded rupture events occur. The load shared by the adhesion molecules located at the remaining contact area increases and the detected force approaches the non-linear, stochastic force regime where single- or cluster- unbinding events occur. Thereby the retraction after $F_{Max}$ shows step like events. These steps are characterized by the fact that they counteract against the applied retraction force. Depending on the slope before the discontinuity it can be distinguished between a non-linear decrease or a force plateau before the jump [79]. The events

with a non-linear increase, occur in the near surrounding to the ($F_{Max}$) point. A cytoskeletal anchor of the involved proteins is suggested, which reduces further separation until the cell-substrate contact ruptures. Also it is possible that the cytoskeletal anchor breaks. In this case, as well as the case of no membrane anchor, the attached cluster pulls a membrane tube called tether. Tether are visible as constant force plateau and can be described in this regime by membrane stiffens and tension [71]. When they occur, tether are the last contact between cell and substrate.
To extract the parameter, the force curve is overlaid with high frequency signals from the experimental setup. Filters are applied to the power spectrum of the force function to smoothen the curve. Therefor the peaks of the spectrum are detected and a notch filter cuts of high frequency signals. Afterwards a median filter further smoothens the signal by removing signal outliers. The steps are finally localized through the first derivative of the force function. The detected steps exceeding a defined height threshold are selected for their distinguishment from the background. Step properties extracted are their relative step height $F_{Step}$ and distance to the adjacent step $l_{Step}$, the position of the point of inflection at a step as $l\text{-}Position_{Step}$ and $F\text{-}Position_{Step}$, the number of steps per curve $N_{Step}$ and the pulling length $l_{Pull}$ after which the cell is completely detached.
During $t_{con}$, a bright field image is acquired as shown in figure 3.5 (C). To determine cell diameter, image analysis is performed with Fiji [80]. After the tip region, the cantilever width is constantly 100$\mu$m, what is set as a scale to determine the pixel size. By assuming a circular contact area the cell diameter is measured.

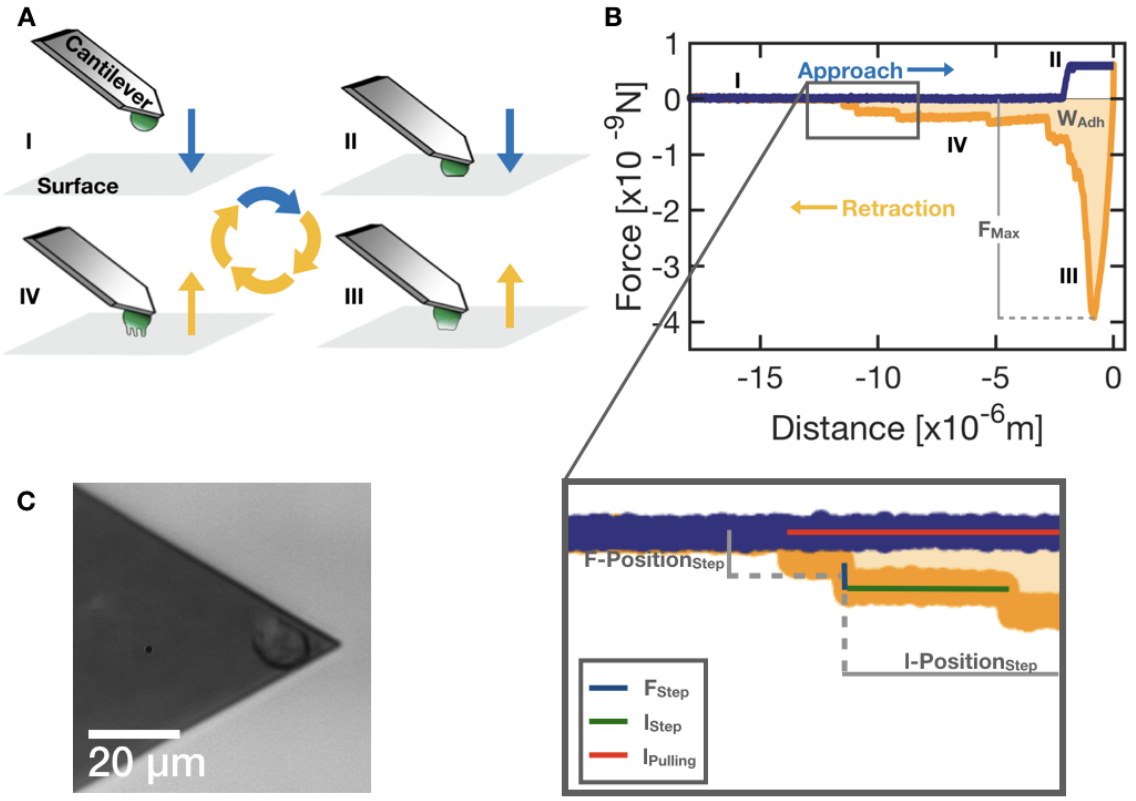


Figure 3.5.: (A) Steps of the cell-cantilever setting for SCFS setup. The repeated cycle begins with surface approach and pushing with a constant force $F_{con}$ to ensure contact and enabling the establishment of cell-surface adhesion (I and II). By applying a retraction force the contact area reduces (III) until tether rupturing (IV) and the retraction of the whole cell. The arrows illustrate the direction of cantilever movement. The approach phases are colored in blue, the retraction phases in orange.
(B) shows a resulting force curve with corresponding phases marked by numeration and color-code. (I) shows the approach phase with a constant reduction of distance. At contact (II) the force increases until $F_{con}$ is reached and held for the time $t_{con}$. The retraction force increases until $F_{Max}$ is reached and unbinding of the small regions occures by accompanying reduction of contact area (III). The unbinding of last adhesion cluster is visible in (IV) and refered to as tether until the cell is detached from the substrate and the force is zero again.
(B) sub-figure of enlarged region of force curve shows details to the analyzed step parameters. (C) figure of bright field image shows a *D.d.* cell attached to a cantilever tip in bottom view.

## 3.3. Metal-Induced Energy Transfer (MIET)

For an overview of the theoretical background see the MIET section in the background chapter 2.5. This section is concentrating on microscopy methods to perform MIET measurements.

### 3.3.1. Confocal microscope

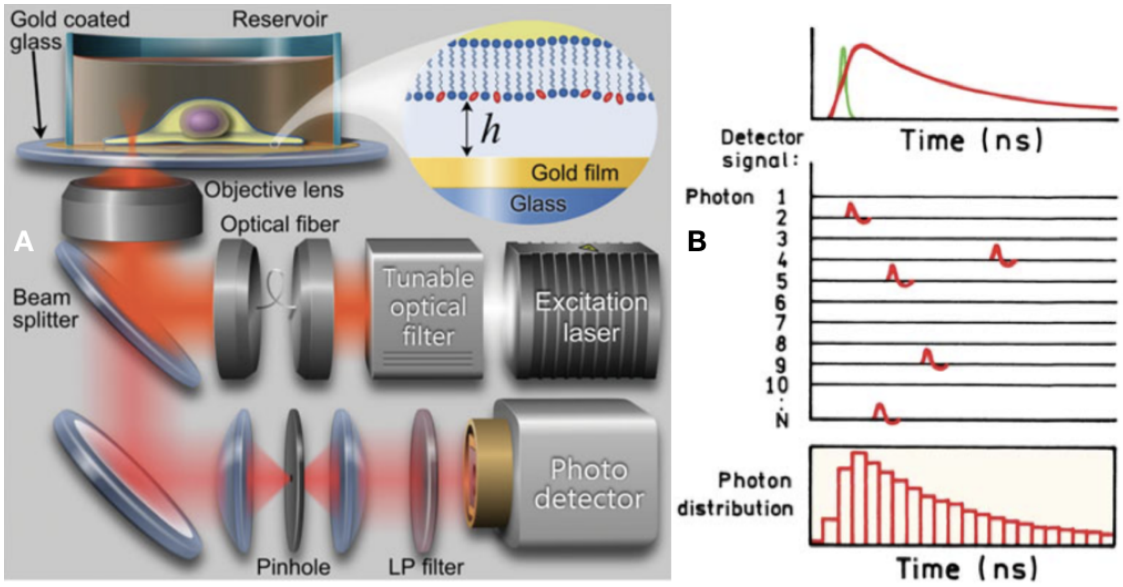


Figure 3.6.: (A) shows a schematic drawing of a confocal microscope with MIET setup. The excitation laser produces laser pulses of a defined wavelength. These pulses pass through different filters onto the beam splitter and are focused with the objective lens on the cell to excite fluorescent molecules. The emitted light is again focused on the beam splitter but has a longer wavelength and therefore can pass the beam splitter. The remaining light after the beam splitter is focused on the pinhole. Only light from the focus point can pass the pinhole and be detected by the photo detector. The slide is coated with a 15nm thin gold layer, which interact with the fluorescent molecule and causes the required lifetime change for the MIET measurement. From [61].
(B) shows a schematic drawing to visualize the TCSPC methode. The top figure shows the reaction of many fluorescence molecules (red line) to a light pulse (green line). The middle figure presents the detector signal after an initial light pulse (green line top figure) with just a few fluorescent molecules. To create the TCSPC histogram, in the bottom figure, the measurement is repeated multiple times. From [81].

MIET is carried out with a confocal microscope. The confocal microscope is designed to focus the emitted light beam onto a small spot of the probe and exclude

light for example of neighboring molecules by a pinhole as shown in Figure 3.6. The fluorescence molecules transit into the excited state due to excitation by the light beam and emit photons. Only emissions from the focus point pass the pinhole and can be detected. By reducing background noise, this technique increases the lateral and axial resolution. The resulting picture is shot by scanning the probe. A confocal microscope is a light microscope using the effect of fluorescence molecules to emit light after being excited by a different, shorter wavelength. Because of the wavelength change, the mingled light beam can be splitted as shown in Figure 3.6 (A). A dual label can be achieved by specific fluorescence proteins with a difference in their absorption and emission spectra. Two independent laser excite their respective molecules. Again, beam splitter are used to separate the excitation laser signal from the transmitted light and split the transmitted signals from the different labels. A common pairing, also used for this work, are the green- and red-fluorescent protein (GFP and mRFP/mCherry).

### 3.3.2. Time Correlated Single Photon Counting (TCSPC)

A sample labeled with fluorescence molecules would react to an excitation pulse by emitting photons. The resulting decay curve is shown in red, the excitation pulse in green, in the top Figure of 3.6. To achieve a high lateral resolution, the focus point of the excitation laser is between $200-300$nm, which limits the number of excitable proteins to estimated $0-10$, due to empirical values. The time correlated single photon counting (TCSPC) method determines the fluorescence lifetime of a probe with few fluorescent molecules in the defined laser spot.
The excitation laser is emitting light pulses with an interval of 50ns which are focused onto the sample and thereby stimulate fluorescence molecules. The arrival time of the first emitted photon between two excitation light pulses is detected and stored as a histogram as shown in the middle and bottom Figure of 3.6(B). For several measurements the distribution of the histogram displays the fluorescence decay function, which can be described by

$$I(t) = I_0 \cdot \exp(-t/\tau_f).$$

The fluorescence lifetime $\tau_f$ can easily be calculated as the time when the intensity is decreased to $I(t = \tau_f) = \frac{1}{e}$ of its initial value $I_0$ [81].

The accuracy of the fluorescence decay function and thereby of the fluorescence lifetime depends on the number of counts per pixel. Many counts smoothen the TCSPC curve and therefore increases the accuracy. Depending on the cell brightness, the measurement time per pixel is between $3-10$ms. This results in roughly $6-20 \cdot 10^4$ pulses per pixel. The error curve depending on the detected intensity per pixel is shown in Figure 3.7 (A).

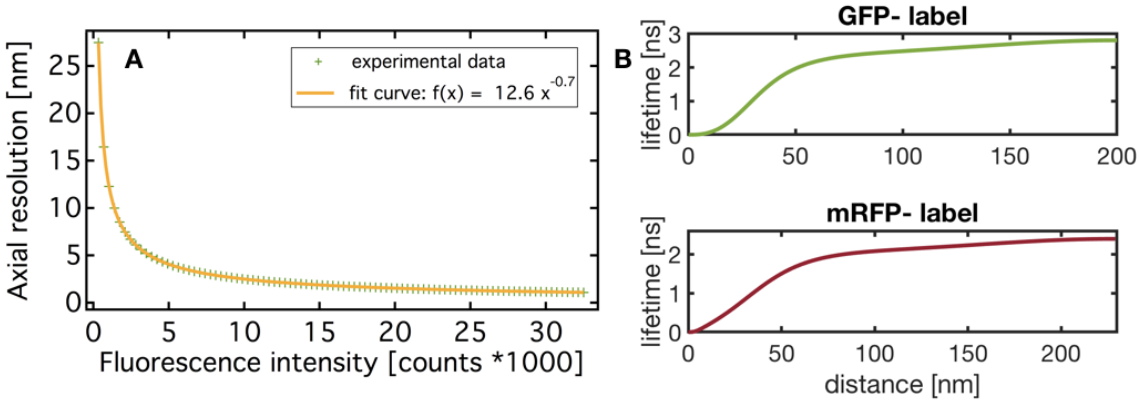


Figure 3.7.: (A) Experimental data shows the axial MIET resolution for a given fluorescence intensity. The results are fitted with $f(x) = mx^b$. (B) shows the calculated lifetime-distance curve for the two used fluorescence labels. The upper curve shows the GFP-label, the bottom curve shows the mRFP-label. The curves are calculated for the experimental setup. These plots show the monotonous region of the curve.

### 3.3.3. Experimental Setup

The object slide is coated with a gold layer of 15nm thickness by an evaporation machine. Measurements with an atomic force microscope done by *Alexey Chizik* detected the surface roughness of the metal layer lower then 1 nm. The cells need to sediment and adhere to the substrate for $15 - 30$min, before the measurement can be started. An example of a spreaded cell in the object chamber is shown in Figure 3.6. One defines the recording time per pixel by choosing an image section and lateral resolution for each image. The lateral resolution is defined as the resulting pixel size and hence needed to convert pixel position into a distance. To achieve high axial resolution, a high intensity and therefore long recording time per pixel are preferable. As such an area that covers one cell is defined and the shot is started. The confocal microscope scans the chosen area and creates the fluorescence decay function for each pixel. The mentioned pixel dimension for high lateral resolution is between $200 - 300$nm. For an image section of 30 x 30$\mu$m to comprise the cell body of *D.d.*, the resulting matrix will have a dimension between 80 x 80 and 120 x 120 entries. With a typical acquisition time of $3 - 10$ms per pixel, the time to record an image is in range of $20 - 145$s. A further increase in recording time per image to achieve higher axial resolution for example can cause a shift between the first and last recorded pixel due to cell movement. Prolonged irradiation of the probe can result in higher stress for the cell and a faster bleaching of the fluorophores intensity. As mentioned in section 2.5, experimental parameters like coating material and its thickness or mean fluorescence lifetime of unperturbed protein, are used to calculate the lifetime-distance curves for each fluorescence protein. The resulting curves are

shown in Figure 3.7 (B).
The resulting images, obtained from the measurement, is a $n$ x $m$ matrix, where $m, n$ are the position in $x, y$ direction in pixels. Each entry contains the TCSPC curve of both fluorescence channels. A *MATLAB* script is used to calculate the fluorescence lifetime for each pixel, as shown in section 3.3.2, for each channel. The resulting lifetime images, are transformed with the calculated lifetime-distance curves as in figure above in matrices containing the height information. With the noted lateral resolution, the pixel position can be transformed into a distance.

# 4. Results

The aim of this work is to investigate the influence of clathrin on the adhesion process of *D.d.*. Therefore a dual strategy is pursued, by investigating force curves from SCFS and by analysing the height matrices generated through MIET microscopy. The results are compared between wild-type and knock out or different labeled cells to get a closer insight on the position and functions of clathrin coats as well as the colocalisation and interplay with actin foci and membrane position. A short overview of the analytical methods used in this thesis can be found in Section A.

## 4.1. Single Cell Force Spectroscopy (SCFS)

### 4.1.1. Force Curve Parameters

As shown previously for *D.d.*, the stochastic step like rupture events visible upon cell retraction from the surface rely on collective unbinding of adhesion proteins in bond clusters [2]. Therefore this methode is ideal to investigate the influence of clathrin on adhesion clusters, by knocking out clc and comparing the extracted adhesion properties to WT cells. Figure 4.1 shows exemplary chosen force-distance curves for WT cells in (A) and clc- cells in (B).

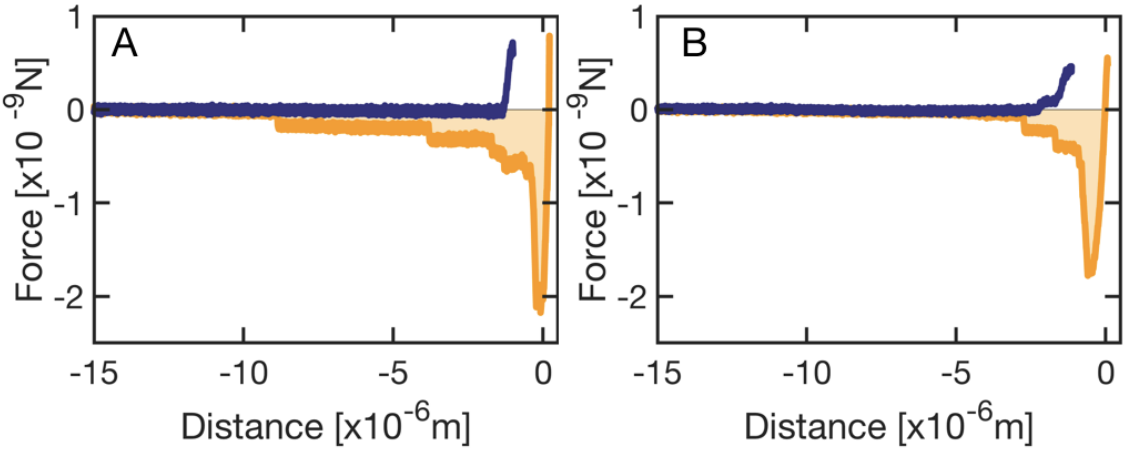


Figure 4.1.: The figures show examplary chosen FDC for WT cells in (A) and clc KO cells in (B). Each figure contains a trace curve in blue and retrace curve in orange. $W_{Adh}$ is highlighted in orange as the area between the retrace curve and the baseline.

In direct comparison, the WT curve shows slightly higher $F_{Max}$ and a larger $l_{Pull}$. The WT in this particular curve, shows also more small rupture events near $F_{Max}$ and a higher $W_{Adh}$.
The parameters are extracted from the force-distance curve with the procedure described in Section 3.2.4. Possible errors that can occur while recording force-distance curves are excluded. Errors that might have influenced the recording are possible contact and thus contribution of multiple cells to the force-distance curve or a possible cantilever substrate contact. These errors can appear in force-distance curve through multiple $F_{Max}$ peaks comparable to a saw tooth or trough a comparable high $F_{Max}$, which were controlled with the recorded bright field image and excluded if necessary. Also artefacts like hydrodynamic flow, electrostatic interaction, impurities or external vibrations influencing the cantilever movement, which can be visible in the linear approach and retraction phase of the force-distance curve, were excluded. The quantified parameters are $F_{Max}$, $W_{Adh}$ and the step properties $l - Position_{Step}$, $F - Position_{Step}$, $l_{Step}$, $F_{Step}$, $N_{Step}$, $l_{Pull}$ and the cell diameter, which are shown in Figure 3.5 (B) and (C). The number of analysed force-distance curves are shown in Table 4.1. The results of the extracted parameters are

| | WT NC4A2 | NC4A2 CLC- |
|---|---|---|
| # experiments | 10 | 8 |
| # cells | 52 | 40 |
| # curves | 210 | 258 |

Table 4.1.: Statisics of SCFS experiments for WT and clc- cells. The number of experiments refers to a new experimental setup with freshly received cells but where multiple experiments a day are possible. The number of cells and curves refer to the number of evaluated cells/curves and not the total number of recorded force curves. Force-distance curves, where no substrate was found, cell contact was unsure, the possibility of multiple cells being attached to the cantilever existed or artefacts were visible in the linear approach/retraction phase were manually excluded of this statistic.

transferred for further analysing into the scientific data analysis program *IGOR Pro* developed by *WaveMetrics Inc.*. To analyse significant differences in the probability distribution of the extracted parameters, the respective distributions of WT and KO cells are compared with a significance test. To chose the required test, knowledge about the distribution shape is necessary. For instance a normal distributed parameter would be compared with the *Two-Sample T Test*, where the *Wilcoxon Rank-Sum Test* is used for other distributions. For the statisical analysis a short overview of the moments describing a probability distribution as well as the tests implemented in *IGOR Pro* to select the appropriate test and to interpret the test outcome is given in Section A.2 and A.3.

### 4.1.2. Overall Adhesion Properties

This section discusses the parameters characterizing the appearance of a force-distance curve and therefore the overall adhesion. For the presentation of the results the box plot is chosen. The box parameters used are explained in Section A.4. The distribution of the maximum adhesion force is a non normal distribution with a long tail towards higher force values. The distribution median is reduced significantly from 1.39 x $10^{-9}$ N for WT, to 1.14 x $10^{-9}$ N for clc- cells, which is shown in Figure 4.2 (A) with the respective results listed in Table B.1. Interestingly, the box parameters for both types have the same size with $\Delta^{+}_{F_{Max}} = 0.78$ x $10^{-9}$ N to 0.76 x $10^{-9}$ N and $\Delta^{-}_{F_{Max}} = 0.54$ x $10^{-9}$ N to 0.52 x $10^{-9}$ N. Therefore both distributions coincide in their shape, but the KO distribution is shifted to smaller values.

The adhesion work distributions, shown in Figure 4.2 (B), have a long tail, which

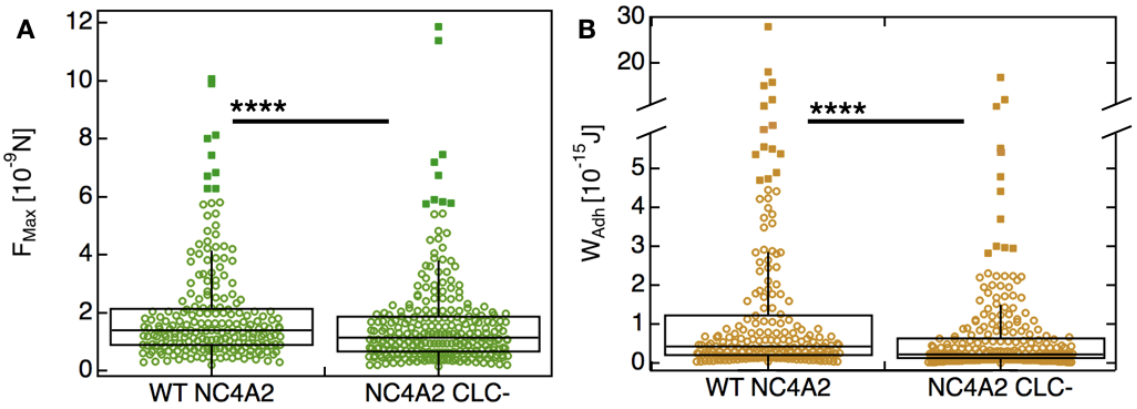


Figure 4.2.: Box plot and significance level for the WT NC4A2 and the NC4A2 clc- cells for the maximum adhesion force (A) and adhesion work (B).

can also be deduced from the $\Delta^{+}_{W_{Adh}}/\Delta^{-}_{W_{Adh}} = 3.5$ ratio for the box parameters of the WT. Even though this ratio is comparable to that of the KO $\Delta^{+}_{W_{Adh}}/\Delta^{-}_{W_{Adh}} = 3.7$, the box width is drastically reduced by a factor of 2, which can be seen in Table B.1. This indicates, that the $W_{Adh}$ probability density of the KO is more centered around its median value. Furthermore, the KO median value is significantly decreased from 0.42 x $10^{-15}$ J for WT, to 0.22 x $10^{-15}$ J. If we were to assume a peak-like force-distance curve, a reduction in $F_{Max}$ would also lead to a decrease in $W_{Adh}$. However, this comparatively small 18% reduction for $F_{Max}$ can not explain the factor two loss in the work integral. Furthermore, the additional reduction of the interquartile range $IQR$ for the KO shows drastic changes in the stochastic part of the force-distance curve and the step appearance.

Bright field images provide additional information about the cell diameter at the contact area. The results are shown in Figure 4.3 with a significant increase in the cell diameter median for KO cells, results listed in Table B.1. The performed *JB Test* did not reject the hypothesis of an underlying normal distribution, however

the *W Test* was performed due to differences in the variances of the data sets, with results shown in Table B.2. The cell diameter is determined at two points, where both straight lines running through the center of the cell. The resulting cell diameter is the average of both measurements. The error is defined as the associated standard variation. Due to the underlying normal distribution, the mean value is given with $(12.6 \pm 2.6)$ x $10^{-6}$ m for WT and $(14.2 \pm 2.3)$ x $10^{-6}$ m for KO cells.

By assuming a circular cell shape it is possible to calculate the ratio between the

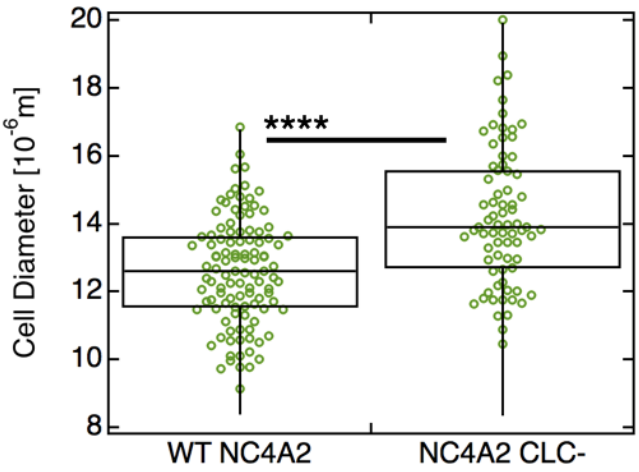


Figure 4.3.: Box plot and significance level for WT NC4A2 and NC4A2 clc- cells for the cell diameter.

maximum adhesion force and the detected area as well as the adhesion work to area ratio, which is shown in Figure 4.4. This reduces the impact of the detected size difference on the unspecific adhesion parameters which depend on the contact area. Due to the enlarged cell diameter, the tendencies detected and described in Figure 4.2 are even more visible. The maximum adhesion force per area decreases significantly in their median value from 12.2 N/m$^2$ to 7.7 N/m$^2$ for the KO and the box width is decreased for the KO describing a more centered distribution, with respective values listed in Table B.3. The long tail region of the KO containing outliers and far outliers is less pronounced.

The adhesion work per area shows the same tendencies in Figure 4.4 (B). With a significant decrease in median value for clc- cells from 0.42 x $10^{-5}$ J/m$^2$ to 0.19 x $10^{-5}$ J/m$^2$, as well as a 2.3 times smaller box width and thus a way more centered, leptokurtic distribution with reduced long tail range.

As a result the clathrin light chain KO shows impressively the impact on the overall force-distance curve appearance. This is highlighted by a reduction in maximum adhesion force (per area) and therefore a change in the continuous part of the curve, where the whole contact area is contributing to $F_{Max}$. The light chain KO also impacts on the adhesion work (per area), which can be described as the work needed for de-adhesion. To investigate the detected changes in adhesion work in

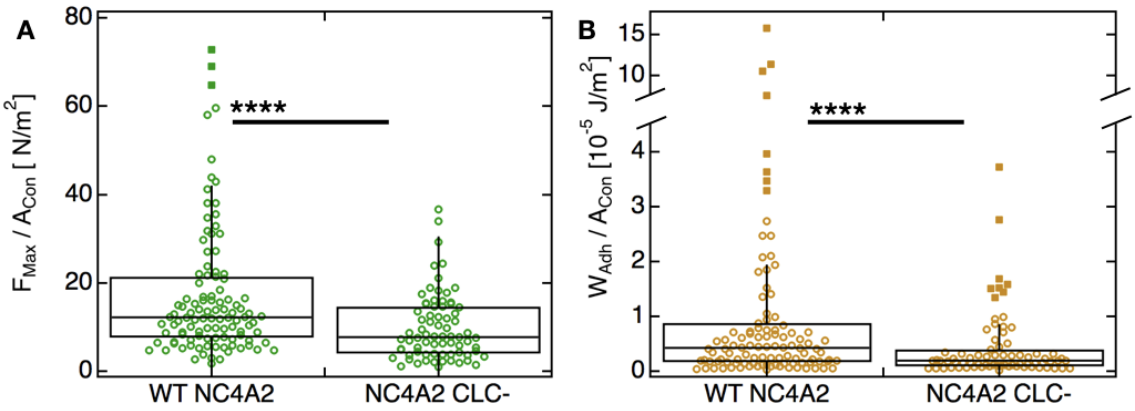


Figure 4.4.: Box plot and significance level for the WT NC4A2 and the NC4A2 clc- cells for the maximum adhesion force per area (A) and adhesion work per area (B).

the stochastic part of the force-distance curve, the following section deals with step properties and appearance, to get a closer insight into the KO impacts on adhesion clusters.

### 4.1.3. Step Properties

The statistics of extracted step properties from the stochastic part of the force-distance curves is shown in Table 4.2. In this experiment, 39 WT cells show steps in

| | WT NC4A2 | NC4A2 CLC- |
|---|---|---|
| #cells showing steps | 39 (52) | 18 (40) |
| #curves showing steps | 92 (210) | 40 (258) |
| #steps | 268 | 90 |

Table 4.2.: Step statistics for SCFS experiments of WT and KO cells. The #cells showing steps entry referes to the number of cells showing a step at least in one curve. Also listed are the total number of curves, where steps could be detected, and the total number of detected steps. The values in brackets indicate the total number of cells and curves and serve for comparison.

at least one recorded force curve, which accounts for 75% of the total cell number. On the other hand, only 45% which equals a number of 18 cells, show steps for the KO. This shows impressively that the clathrin knock-out affects the ability to show steps and therefore indicates a malfunction of the adhesive clusters formation. Out of all the curves showing steps, the same tendency is visible for 44% of WT and 16% KO curves. If a step is detected on a curve, the curve has on average 2.9 steps per

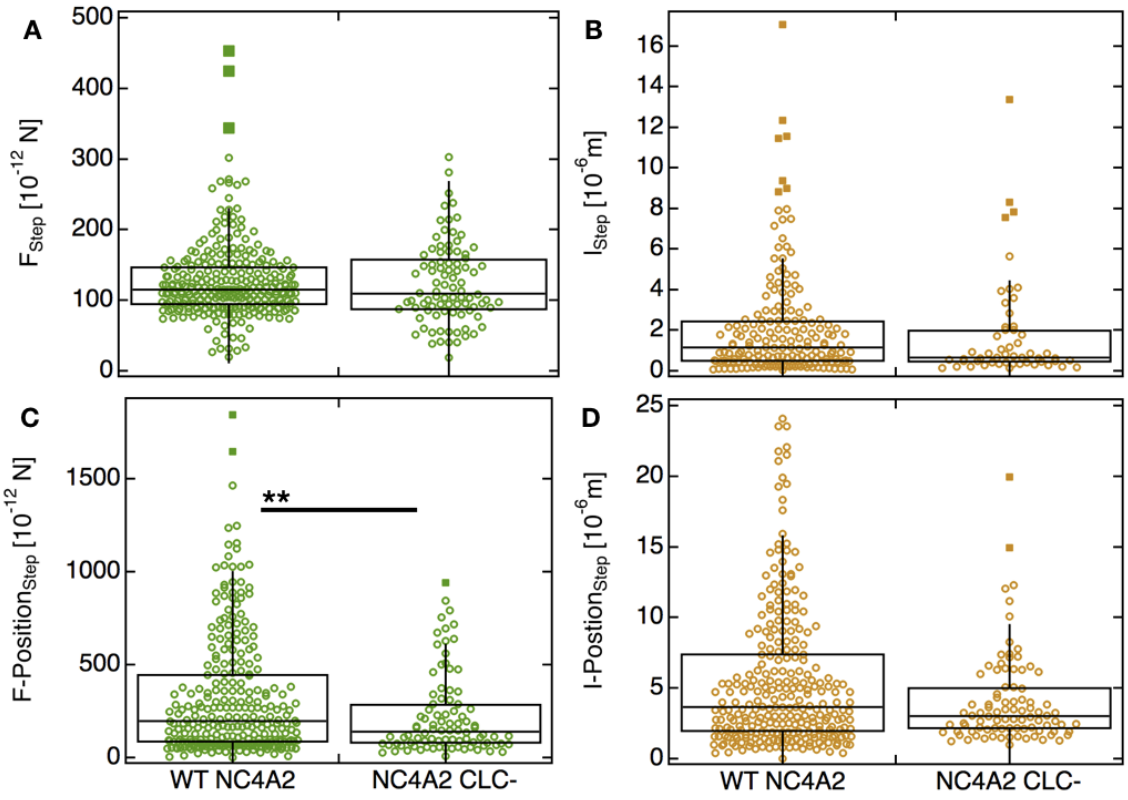


Figure 4.5.: Box plot and significance level for WT NC4A2 and NC4A2 clc- cells of step force (A), step length (B), step position in force direction (C) and step position in separation direction (D).

curve for WT and 2.3 for KO cells.

To get a closer insight into step appearance, Figure 4.5 and 4.6 show the extracted step parameters. The significance test recommends equal median for the step force with 114.9 x $10^{-12}$ N for NC4A2 to 109.3 x $10^{-12}$ N for NC4A2 clc-. Also the upper to lower box ration seems comparable with slightly larger box width for the KO, as visible in Figure 4.5 (A) with the results shown in Table B.4. Interestingly, the performed *W Test* also recommends equal median for the step length with 1.15 x $10^{-6}$ m to 0.65 x $10^{-6}$ m for the KO. The $\Delta^{-}_{l_{Step}}$ value is decreased for the KO from 0.71 x $10^{-6}$ m to 0.25 x $10^{-6}$ m hinting at a distribution shifted to smaller step lengths, which is confirmed at Figure 4.5 (B). The outliers and far outliers show steps with a step length range comparable to the WT and therefore hint at tether formations for both cell types. With the *W Test*, the far outliers of the KO achieve high ranks. Combined with the sample size of 50 data points for the KO to 176 data points for the WT, the outlier ranks shift the KO rank sum to higher values. This possibly explains the acceptance of equal median hypothesis due to tether appearance, while detecting a median decrease to 56% of the WT value and

thus shows in comparison to the WT an increased occurrence of data points at lower step length values.
The median step position is significant decreased for KO cells from 196.1 x $10^{-12}$ N to 109.3 x $10^{-12}$ N in force direction as shown in Figure 4.5 (C) and no difference in separation direction with 3.65 x $10^{-6}$ m to 3.01 x $10^{-6}$ m for the KO in Figure 4.5 (D). In both cases, however, the distribution in WT cells is spread wider, which can be deducted from the increased box width parameters listed in Table B.4 and the more pronounced long tail regions and thus an increased likelihood for step appearance at positions of higher values. The step parameters visualized in this way only allow a one-dimensional analysis therefore, the next section shows probability density maps to discuss interdependences between the extracted parameters.
The pulling length, after which the cell is completely detached from the substrate

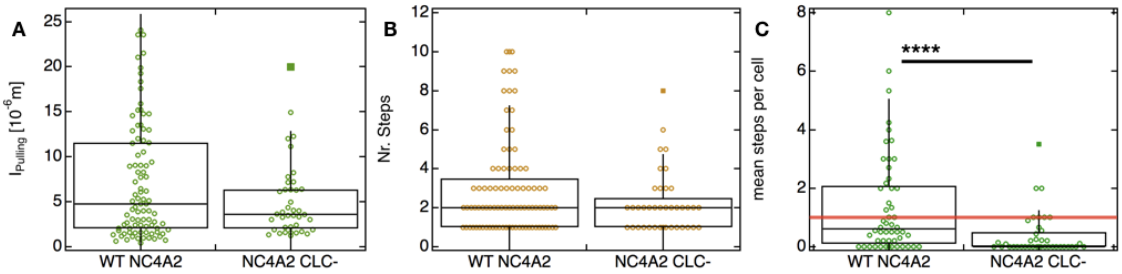


Figure 4.6.: Box plot and significance level for WT NC4A2 and NC4A2 clc- cells for the pulling length (A) and the number of steps per curve (B). The number of steps box plot excludes the curves showing no steps. (C) shows the mean step number per cell. The red horizontal line symbolises the point where every curve of the cell on average shows one step. The box plot also contains cells which show no steps.

shows no significant difference between the medians of both distributions, with results listed in Table B.6. However the upper box of the WT spans a wider range with $\Delta^{+}_{l_{Pulling}}$ from 6.89 x $10^{-6}$ m to 2.76 x $10^{-6}$ m for the KO as shown in Figure 4.6 (A). This results in a wider inner fence rang of the box plot, which coveres all data points of the WT distribution, while for the KO outliers occure. This shows that, while both distributions are centered around a comparable median, the 50% data points range larger then the median value is spread wider. Thus, if the pulling length of the cell exceeds the median, the probability for higher values increases for the WT, while the KO distribution is comparatively closer to the median. The number of steps follows the same behavior, for all curves showing at least one step, which is shown in Figure 4.6 (B). The median and $\Delta^{-}_{\#Steps}$ shows no difference for either types, results shown in Table B.6, while the upper box spans a wider range for the WT with $\Delta^{+}_{\#Steps} = 1.75$ to 0.75 for the KO.
However, this way of presenting the step number does not cover the cells and curves not showing any steps. The WT shows more steps and has a more pronounced long tail in the number of steps distribution, even though both distribution are centered

around the same median. Another way to visualize the ability to express steps that captures all curves of a single cell is shown in Figure 4.6 (C). In this figure each point $\overline{\#Steps_i}$, represents the mean number of detected steps per curve for the $i$th cell, calculated with

$$\overline{\#Steps_i} = \frac{1}{M_i} \sum_{j=0}^{M_i-1} \#Steps_{i,j} \tag{4.1}$$

and $M_i$ the number of evaluated curves for the $i$th cell, which is limited to a maximum of $M_i^{max} = 10$ curves per cell. With this representation it is possible to show, how many cells express steps and if so, how many steps they show on average. The median of the average number of steps per cell shows a significant decrease from 0.61 for WT to a distribution centered around 0 value for KO cells. The upper box decreased as well with $\Delta^{+}_{\#Steps} = 1.75$ for the WT to 0.75 for the KO. The box-plot also contains a horizontal line around the value where each curve shows on average one step. Interestingly, only three KO cells show more then one step per curve in comparison to 19 WT cells showing on average more then one step per curve.
In a summary, even if there are little differences for the median of most step properties, the greater part of the clc- cells expresses few steps and only a small proportion of 7 cells, which are showing on average at least one step per curve, are producing the majority of the detected steps. Also, in most cases, the KO distribution is more centered around the median and the WT shows a more pronounced long tail region with increased probability of higher values. The exceptions are the step force distribution and step length, while the comparable long tail regions in the step length distribution hints at the occurrence of tether.

### 4.1.4. 2D- Probability Density Map of Step Properties

A probability density map of the step coordinates as shown in Figure 4.7, visualizes step appearance in the stochastic part of a force-distance curve and thereby can help examine interdependences between parameters. An enveloping function was chosen to visualize the limitation of step appearance in the force-distance space. Interestingly the WT spans a wider space with an area of 11.3$\mu$m nN compared to 5.5$\mu$m nN for the KO. Outliers can be found for the wild- type cells, for step positions larger than the covering function, whereas the step appearance of the KO is well described by the covering function and seems to be limited to step appearance closer to the origin. The long-tail above the covering function for small force values shows the probably last steps before the cell is detached from the substrate, while the large separation from the substrate indicates possible pulling of membrane tether. Thus the occurrence of steps for small step positions in force direction higher than the covering function may indicate tether and can be found on both density maps.

A probability density map for the step force and step position in separation direction shows a distribution centered around the step force median, which is

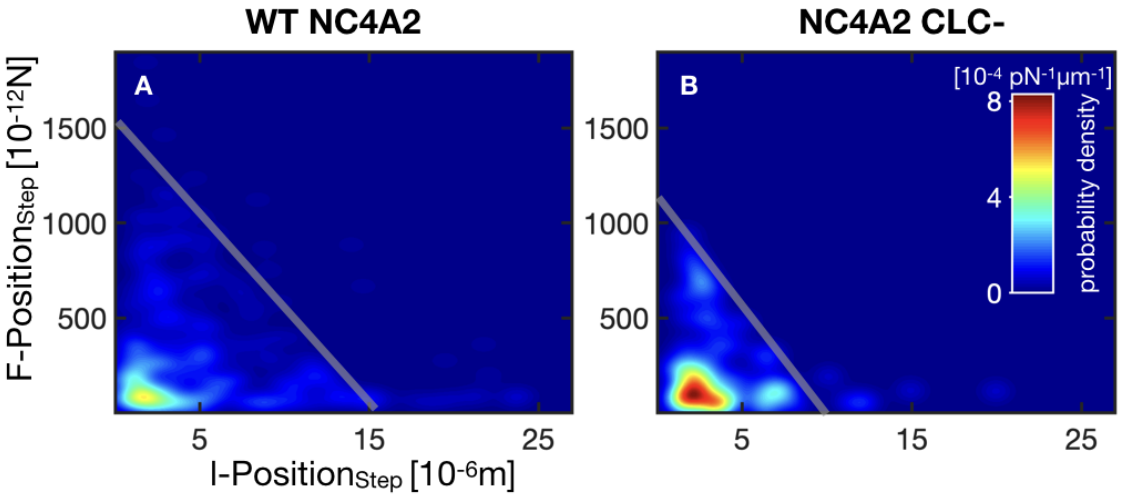


Figure 4.7.: Probability density map for the step position in force and separation direction for the WT on the left side and the clc KO on the right side. The grey line is drawn for the WT between
(0$\mu$m , 1.5nN) and (15$\mu$m , 0nN) and for the KO between
(0$\mu$m , 1.1nN) and (10$\mu$m , 0nN), to visualize that the function covers most of the appearing steps.

detected from the box plot, visualized as grey horizontal line as it is shown in Figure 4.8 (A) and (B). For the WT, at small separation the step force distribution is spread over a range up to 240pN from which on outliers occure. With increasing separation the step force distribution is more centered around the median. In separation direction the map shows a continuous distribution up to a separation of 25$\mu$m.
The knock- out distribution seems not centered around its median but shows a maximum below the median line, while a second maximum is present above the median line. Also, while the WT distribution converges for larger separations towards the median line, the KO cells show no separation dependent convergency. Instead step forces higher 200 pN where detected until a 9$\mu$m seperation. However the probability density map of the KO appears to be centered around the median for smaller separation values up to 9$\mu$m, also in accordance with the enveloping function from Figure 4.7.
A probability density map of the step force and position in force direction is shown in Figure 4.8 (C) and (D). The most common steps of WT cells appear around the median symbolized by grey horizontal line at the origin of step position in force direction. The probability density map shows the step force distribution centered around the median with a high probability of step appearance for positions up to 0.4 nN and is continuously distributed for position values up to 1.3 nN.

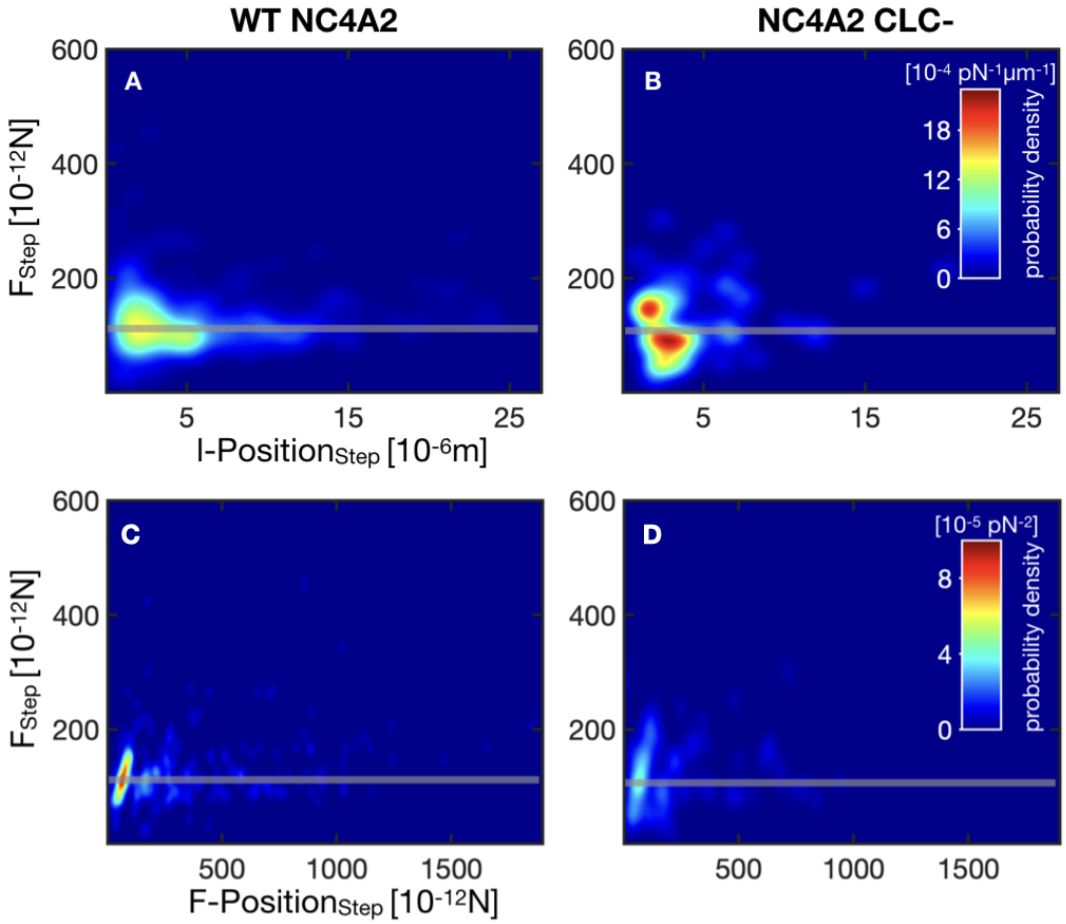


Figure 4.8.: Probability density map for the step force and position in separation direction for the WT in (A) and the clc- in (B). The probability density map for the step force and position in force direction is shown for the WT in (C) and the clc- in (D). The grey line represents the detected step force median from the box plot as listed in Table B.4 at 114.9 pN for the WT and 109.3 pN for the KO.

The distribution shown by the KO is continuous with a heightened probability centered around its median for a position value up to 0.2 nN and scattered steps around the median, up to 1.0 nN. These probability density maps containing the step force impressively show, that even if the step force in both distributions is centered around an equal median, the probability of steps appearing away from the origin is much larger for WT cells and thus they span a wider range in the step position map.

## 4.2. Metal Induced Energy Transfer (MIET)

The MIET microscopy method provides a matrix with the intensity values of the label and a matrix with the corresponding heights for each label as well as the pixel size for each image. In a first step, the contact areas of the different label combinations are detected and the height distribution in the contact area are compared between different labels. Afterwards foci in the contact area are determined with a *Matlab* routine and the foci parameters, such as number and size, are compared. Furthermore the height distributions in the foci areas are compared with the height distributions of the adjacent pixel areas, which enables the detection of possible height changes in the area of increased activity.

### 4.2.1. Contact Area and Average Height

A *Matlab* script was written to define the outline of the contact area in order to generate a binary matrix of the contact area. Further, it is useful to separate cell contour and cytosol, for the height analysis of the contact area and for actin foci detection. Along the cell contour the membrane bends away from the contact area. The resulting height map shows higher areas near the cell outline which is shown in Figure C.6. The actin activity along the cell outline during pseudopodia formation could be detected as a local maximum and thus counted in the actin foci detection. Vacuoles are visible in the actin intensity matrix showing a comparatively low intensity, which leads to inaccurate ventral membrane height and thus generates error. A *Matlab* script is used to exclude the described areas based on the LimE label, resulting in matrices with the intensity and height values of a cytosolic contact area without vacuoles. The working principle to detect the cytosolic contact area is explained in Section C.1, the removal of the vacuoles is explained in Section C.2. The resulting statistics are listed in Table 4.3. The carA-label in some cells shows

| | # experiments | # Cells | # Images |
|---|---|---|---|
| LimE-GFP | 3 | 18 | 108 |
| carA-mCherry | | | 106 |
| LimE-GFP | 3 | 20 | 112 |
| clc-mRFPmars | | | 112 |
| LimE-GFP (clc-) | 3 | 16 | 73 |

Table 4.3.: Statistics of detected contact area for the different labels and knock-out combinations of *D.d.* NC4A2 cells. The number of experiments refers to new experimental setup with freshly received cells. The number of cells and images refer to the number of evaluated cells/images and not the total number of recorded images.

a comparatively high number of *Not a Number* (NAN) entries, where the actual pixel height could not be calculated. Cells with more then 20% of NAN pixel at the

detected contact area are excluded from the statistic.
The contact area is calculated as product of the sum of non-zero elements in the binary image and the pixel area. The results are shown for the different label combinations in Figure 4.9 (A), with the results listed in Table C.1. In direct comparison, carA and LimE dual labeled cells show the smallest median contact area with 121.8 x $10^{-12}$ $m^2$. The clc and LimE dual label show a significant increased

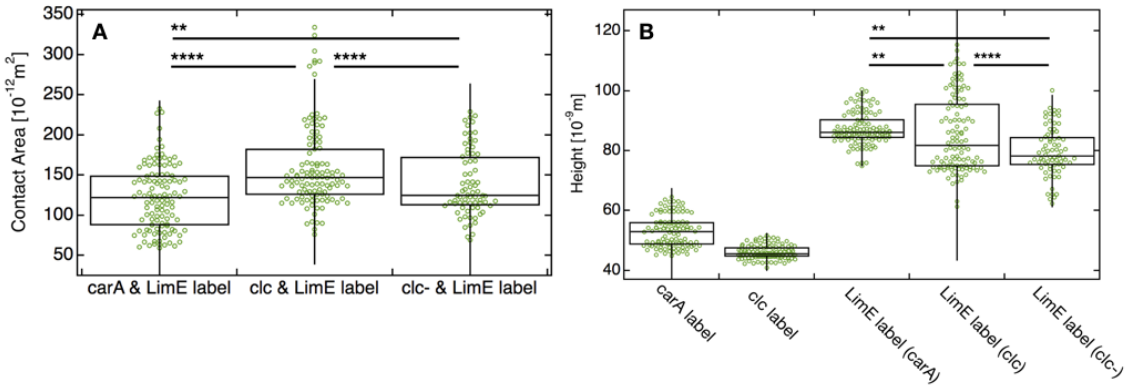


Figure 4.9.: (A) Box plot and significance level of the contact area of NC4A2 wild-type cells with a carA and LimE label on the left, clc and LimE label in the middle and NC4A2 clc- cells with a LimE label on the right. (B) shows box plot and significance level of the weighted mean heights at the contact area without contour and vacuole area. The expression in brackets behind the LimE label, refers to the second label or the knock-out.

median with 146.7 x $10^{-12}$ $m^2$ and also clc knock-out cells with LimE label show a significant increase with 124.5 x $10^{-12}$ $m^2$. The ratio $\Delta^{+}_{contactArea}/\Delta^{-}_{contactArea}$ is 0.8 for carA and LimE labeld cells and 1.6 for clc and LimE labeld cells. Therefore the distribution of both label combinations is comparatively symmetrical around the median. The ratio of the knock-out cells is asymmetrical with 3.9 and shows a long tail towards higher contact areas, while the lower box width indicates that the data points are close to the median.
In a first approach to determine the average height of the respective label, the error weighted mean height is calculated:

$$\bar{h} = \frac{\sum_{i=1}^{N} h_i/\sigma_i^2}{\sum_{i=1}^{N} \sigma_i^{-2}}, \tag{4.2}$$

with $h_i$ the $i$th element of the list of height values from the cytosolic contact area without vacuoles and $\sigma_i$ the corresponding height error. The results are shown in Figure 4.9 (B) and listed in Table C.2 and C.3. Interestingly, the carA membrane label shows a median height of 52.9 x $10^{-9}$ m and is therefore higher than the clc label with a median of 45.5 x $10^{-9}$ m. The clc weighted mean distribution has a

$IQR$ of 3.2 x $10^{-9}$ m while the membrane label has a $IQR$ of 7.6 x $10^{-9}$ m and thus in comparison showing a wider spreading behavior. The LimE label as indicator for freshly polymerized actin has a median average cell height of 86.1 x $10^{-9}$ m for the cells with carA as second label and thus with unperturbed clathrin processes. A significant decrease of the modulus can be detected for the LimE label with knocked-out clc to 78.2 x $10^{-9}$ m. The average height distribution of the LimE label with restored clc has in direct comparison the largest $IQR$ of 21.3 x $10^{-9}$ m and thus a 2 times larger $IQR$ than the knock-out cells and a 3.3 larger $IQR$ than the LimE label with unperturbed clathrin. The median differs significantly from the median of the other mean height distributions and lies between those values with 81.7 x $10^{-9}$ m.
However, for example a skewed distribution shifts the mean value towards the long tail of the underlying distribution and thus does not show the most common pixel height and neither does a box plot take a possible multi-modal shape of the result distribution into account. The box plot shows tendencies for the height distribution and differences between the weighted mean heights at the contact area for different labels, while the next section gives a closer insight into the height profiles of the individual label.

### 4.2.2. Individual Height Profiles at the Contact Area

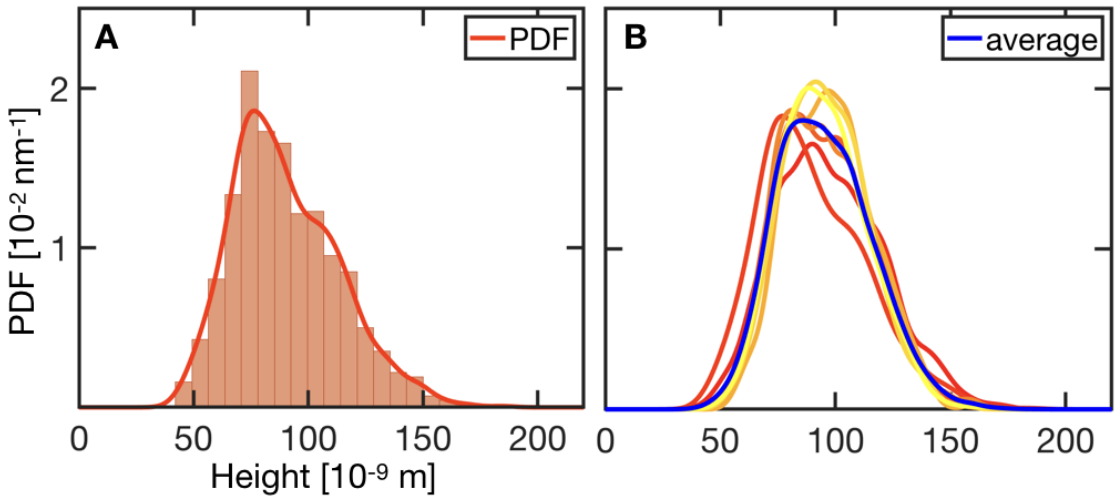


Figure 4.10.: The micrographs visualize the procedure to determine an average PDF of a height distribution from one fluorescence label. (A) shows the histogram of a height distribution from the contact area with excluded contour and vacuole area of one exemplary time point chosen cell matrix. Also shown is the corresponding PDF using a kernel density estimation. (B) shows the PDF of the 6 recorded images for the exemplary chosen cell and their average in blue.

To calculate the height distribution of the cytosolic contact area matrix without

vacuoles for each label, the PDF is estimated with the $KDE$ routine, introduced in Section A.5. The $KDE$ is evaluated on a vector of height values from 0 nm to 220 nm with an increment of 0.01 nm. The resulting PDF is shown for an exemplary data set of an actin height map in Figure 4.10 (A) with the associated histogram. The optimal number of bins for the histogram was calculated, using the *sshist* function. The resulting PDFs are averaged for all images of all cells from a label of a label combination, which is exemplary shown in Figure 4.10 (B) for the LimE label of one cell with the mean PDF in blue. The standard deviation is calculated for each point of the PDF and shown in the following figures as error range around the average PDF.
The results of the indivudal label combination as recorded from the cell types are shown in Figures C.3, C.4 and C.5. In order to compare the height distribution of the respective labels in the cyostolic contact area without vacuoles between the individual labels, the averaged PDFs of the carA, clc and LimE labels are displayed together, as shown in Figure 4.11 (A). For the LimE label, the averaged LimE PDF with carA as second label was chosen, because in this case an influence of the clc label on the clathrin function and a possible indirect influence on the actin behavior can be excluded. In case of the carA and clc label, the PDF is unimodal distributed and, therefore, the modulus of the mean PDF sets one distribution center as most common pixel height, which is shown in Figure 4.11 (A). To determined the error of the modulus, a tangent to the maximum of the function is created. The error in positive or negative height direction is defined as the distance between modulus and intersection of the tangent with the error range as boundary. The error of the 25% and 75% quartile is determined by a horizontal line intersecting the PDF at the respective position. The quartile error is set as distance between the PDF and the error range as boundary in positive direction for the 75% quartile and in negative direction for the 25% quartile, because in opposite direction the horizontal line would intersect the PDF instead of the opposite boundary of the area. The results of the modulus and quartile position are shown in Table C.4 for the carA and clc label. The carA height distribution starts with values at roughly 25nm and ends in a long tail up to 100nm. The modulus of carA is $(41.0, +10.2, -14.5)$ x$10^{-9}$ m and thus 5.5nm closer to the substrate than the clc modulus with $(46.5, +5.2, -3.6)$ x$10^{-9}$ m. Also, the clc label shows a centered distribution close to its modulus with an $IQR$ of 6.7 x$10^{-9}$ m, while the membrane label shows a comparatively wide spread cytosolic contact area height distribution, which can be seen by the $IQR$ of 17.8 x$10^{-9}$ m. So it can be said that the membrane label height distribution begins nearer to the substrate than the clc height distribution and the maximum is also nearer to the substrate. However, the membrane label shows a long tail that reaches up to roughly 100 nm and is not as pronounced in the clc label.

In comparison to the actin activity is noticeable, that the LimE label with carA as second label has an even wider spread height distribution, which can be seen considering the $IQR$ of 34.9 x$10^{-9}$ m. This shows that actin is active in the contact area over a large height range of about $50 - 150$ nm, while the overlap with the averaged carA and clc PDF indicates that actin may also be active at the height or

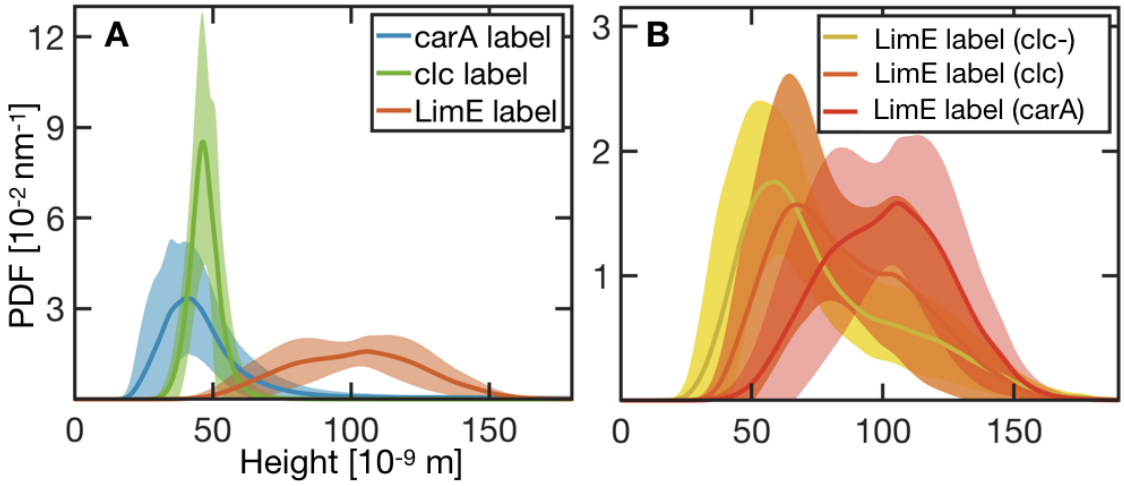


Figure 4.11.: Average PDF of height maps from different fluorescence labels are shown. The colored area around the PDF indicates the standard deviation. (A) shows the height distributions of the clc, carA and LimE labels. The LimE PDF is represented by the LimE label from the carA and LimE dual label. (B) shows the actin height maps with different second labels or with a clc knock-out.

close above the respective label. Furthermore, the LimE-GFP label is present in the different label combinations as well as the clc knock-out, which allows a comparison between the averaged LimE PDFs, as shown in Figure 4.11 (B). In all three cases the averaged PDF shows a possible side maximum, which indicates a multimodal distribution. Besides the side maximum, the positive boundary of the error area also shows a second maximum for the averaged LimE PDF at the position of the side maximum, for both dual label combinations. This possible multimodal distribution can occur because the individual PDFs from which the averaged PDF is derived are also multimodal distributed, which would mean that in all PDF actin occurs more frequently at certain levels than at others. The modulus of the LimE distribution with a carA second label is at $(105.7, +23.6, -35.7)$ x$10^{-9}$ m, with a possible second maximum at a smaller substrate distance. The LimE height distribution of the clc knock-out cells shows a pronounced single maximum at $(58.0, +13.7, -19.2)$ x$10^{-9}$ m and thus a significantly smaller substrate distance for the most common height value. Also the distribution shows an pronounced long tail up to the same range as the other distributions but without second maximum. This clearly shows that LimE with clc- is active closer to the substrate and that actin is less strongly represented in the height range where LimE with carA as a second label shows its maximum. Interestingly, the LimE label of the clc knock-out with reinstated clc-mRFPmars shows a mixture of the other two LimE labels in its height distribution, with a modulus of $(67.0, +22.1, -18.2)$ x$10^{-9}$ m and thus close to the clc knock-out case but with a possible side maximum at the position of the LimE maximum with carA as second label.

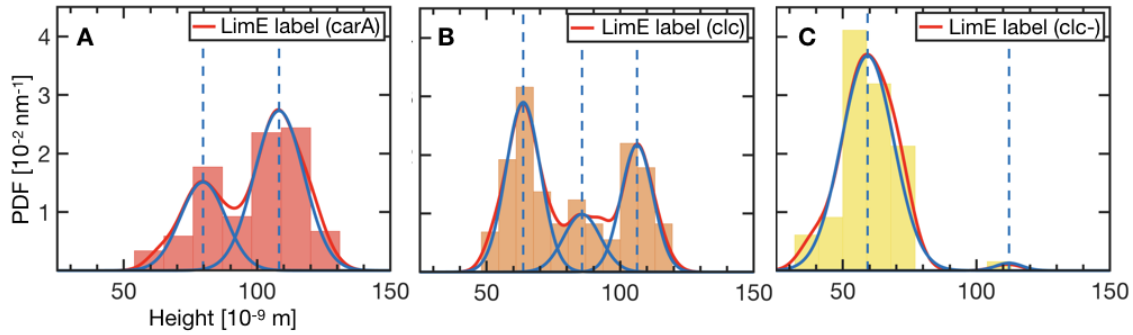


Figure 4.12.: The histograms show the distributions of the modulus, which has been extracted from the actin height PDF of each individual matrix. The red line indicates the PDF, which is found using a kernel density estimation. The blue gaussian functions are fitted to the local maxima with their mean values indicated by vertical dashed blue lines.

As already mentioned, a multimodal distribution can be obtained by the averaging of multimodel distributions. Additionally there is the possibility that a multimodal distribution is created by averaging over unimodal distributions that are distributed around the two maxima that appear. To get a closer insight into the maxima of the averaged multimodal LimE distributions, the modulus of each individual PDF is detected and plotted separately for each label variation in a histogram, shown in Figure 4.12. The PDF of the modulus distribution is estimated as mentioned before and shown as red line. The individual peaks are fitted with a Gaussian function, defined as follows:

$$f_i(h) = \frac{a_i}{\sqrt{2\pi}\sigma_i} \exp -\frac{1}{2}\left(\frac{h-\mu_i}{\sigma_i}\right)^2, \tag{4.3}$$

with the mean $\mu_i$, variance $\sigma_i^2$ and the factor $a_i$ as fit parameters for the $i$th Gaussian function. The resulting fits are shown in the Figure 4.12, with the parameter results listed in Table 4.4.

Interestingly, both dual labels shown in Figure 4.12 (A) and (B) have a peak for the most common actin height close to 108 x $10^{-9}$ m, which is shown in Table 4.4 in segment Gaussian 3. The clc knock-out cells show in a small proportion a distribution with a modulus at a height of 112.2 x $10^{-9}$ m, shown in Figure 4.12 (C) as the second small maximum and thus at a comparable mean height as the other two distributions. The clc knock-out and the clc label both have a comparable peak postion which is shown in Table 4.4 in segment Gaussian 1, while the knock-out has moduli at even smaller substrate distances which is shown in the Figure 4.12 (C) as difference between the PDF and the fit. The LimE height distribution with carA as second label shows a further peak, which is listed in Table 4.4 in segment

| | | LimE label (carA) | LimE label (clc) | LimE label (clc-) |
|---|---|---|---|---|
| Gaussian 1 | $a_1$ | | 0.47 | 0.90 |
| | $\mu_1$ | | 63.7 x $10^{-9}$ m | 59.3 x $10^{-9}$ m |
| | $\sigma_1$ | | 6.5 x $10^{-9}$ m | 9.8 x $10^{-9}$ m |
| Gaussian 2 | $a_2$ | 0.32 | 0.17 | |
| | $\mu_2$ | 79.7 x $10^{-9}$ m | 85.7 x $10^{-9}$ m | |
| | $\sigma_2$ | 8.5 x $10^{-9}$ m | 6.9 x $10^{-9}$ m | |
| Gaussian 3 | $a_3$ | 0.64 | 0.33 | 0.02 |
| | $\mu_3$ | 108.2 x $10^{-9}$ m | 106.3 x $10^{-9}$ m | 112.2 x $10^{-9}$ m |
| | $\sigma_3$ | 9.3 x $10^{-9}$ m | 6.0 x $10^{-9}$ m | 5.0 x $10^{-9}$ m |
| | # | 108 | 112 | 73 |

Table 4.4.: Results for the fit parameters for the modulus extracted from the actin height PDF of each individual matrix. The results are sorted in rows of a comparable mean fit parameter.

Gaussian 2. The LimE and clc dual label also shows moduli values between the two main maxima, which are fitted with a third gaussian function. This fit is of similar height position, compared to the second peak of the LimE and carA dual label and therefore listed in the same segment Gaussian 2 of Table 4.4.
It can be said that the occurrence of a multimodal distribution in the averaged PDF can be explained by grouped moduli of individual PDFs around the detected maxima. Instead of an overall height distribution, the moduli height distribution is focusing on the local maxima and thus does not take the individual distributions into account. However, the comparison between the dual-label and the knock-out cells show a clear trend. While the LimE height distribution with carA as second label, shows two states of most common actin heights, the LimE distribution of clc knock-out cells is mostly centered around one states, which is closer to the substrate. Cells with clc label show a mixture of both behavior, with the most pronounced peak at the same position as clc knock-out cells but with LimE height peaks at positions similar to the LimE moduli distribution with carA as second label.
The height analysis of individual labels in the focus area can provide more detailed information about adhesion behavior, while the comparison to the clc knock-out can provide further information about a changed phenotype of the knock-out at the ventral cell side, which is shown in the next section.

### 4.2.3. Foci Detection and Sorting

A matlab script is applied to detect foci in the intensity image and to define their size. For this, regional maxima are determined in the intensity matrix, as a pre-selection of possible focis, which can be seen exemplary in Figure C.6. The maxima are selected, which clearly distinguish from the background and are not detected for example due to actin activity in pseudopodia area. Afterwards, the focus extent is

determined for each individual focus, based on the intensity of its surroundings and the focus extent threshold. Furthermore the focus adjacent pixels are determined. The described routine is used for all labels to detect possible foci in the contact area. Depending on the label, the parameters for the focus extension detection are varied. A more detailed description of the focus detection routine and the label depended parameter variation can be found in Section C.4. The resulting statistic containing

| | # Cells | # Images | # Foci |
|---|---|---|---|
| LimE foci (carA) | 18 | 100 | 535 |
| carA foci (LimE) | 18 | 100 | 340 |
| LimE foci (clc) | 20 | 109 | 486 |
| clc foci (LimE) | 16 | 88 | 775 |
| LimE foci (clc-) | 16 | 73 | 747 |

Table 4.5.: Statisics of detected foci for labeled and knock-out cells. The number of cells/images refers to the number of evaluated cells/images, not the total number of recorded images. Foci were extracted by the routine explained in Section C.4. Some clc-labeled cells show a uniform and high intensity distribution. For these intensity images, the distinction between a focus and its background was not possible and thus they were excluded.

the number of evaluated cells and images as well as the total number of detected foci is shown in Table 4.5. The clc-labeled cells show variation in the appearance of the intensity matrix. The majority of cells show an medium intensity with prominent clc foci as it is shown in Figure C.15. However, focus detection was not possible with cells of constantly high intensity, which is why 4 cells are excluded from the statistics.
For each focus, the intensity and height of the pixels in the focus area and the pixels adjacent to the focus are given. Furthermore, this data is given for the label for which the focus has been determined and additionally the data is given for the second label. This makes it possible to determine whether the second label also shows increased intensity in the focus area of the first label. This would indicate that the second label also contains a focus and that both foci colocalize. To evaluate this, the average intensity in the focus area and the average intensity of the focus neighboring pixels are calculated for both labels of one cell-type. The focus-neighbour intensity ratio gives a multiplication factor, which is a measure of whether, on average, the intensity in the focus area of the second label is increased or decreased. In order to determine whether there are groups that show increased activity in the second label, the intensity ratio of the secondary label is plotted against the ratio of the first label, as shown in Figure 4.13, as a 2-dimensional probability density map plotted by the method mentioned in Section A.5 on a grid from 0 to 15 with an increment of 0.015. The horizontal axis shows the ratio of the label where the foci were determined, the vertical axis shows the ratio of the second label.

A threshold is defined that selects whether foci in the respective second label,

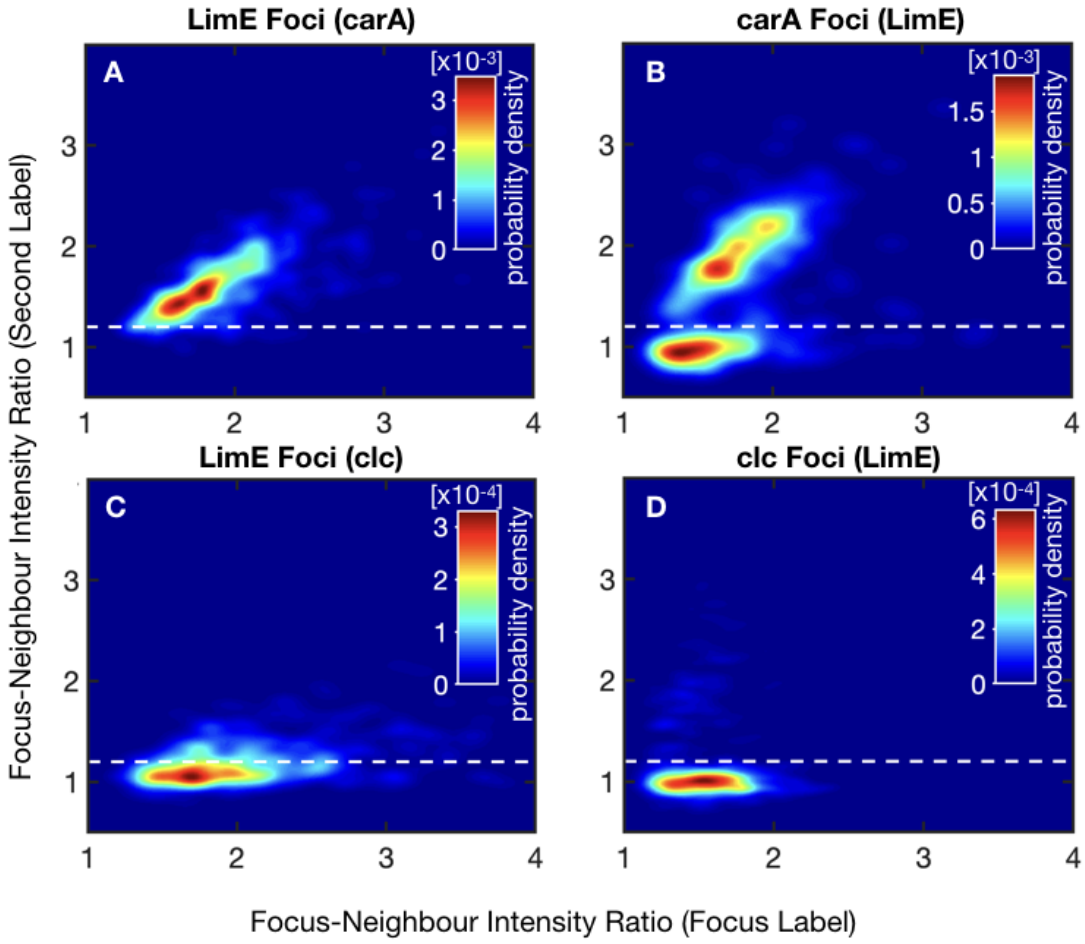


Figure 4.13.: The probability density maps show the Focus-Neighbour intensity ratio of the secondary label, against the Focus-Neighbour intensity ratio of the foci, where the focus routine was performed on. The Focus-Neighbour intensity ratio is defined as the ratio between the average intensity of the detected focus area and the average intensity of the focus adjacent pixel. (A) and (C) shows the detected LimE foci with carA and clc as secondary label, while (B) and (D) shows carA foci and clc foci with LimE as second label. The dashed line shows the threshold for the applied sorting routine.

have an average focus intensity higher than 1.2 times their average adjacent pixel intensity, which is shown as dashed horizontal line at the probability density maps. The detected LimE foci with carA as second label (Figure 4.13 (A)) show that the majority of the distribution lies above the marked threshold and only a tail of the distribution cut the threshold, while all points show a ratio $> 1$ for the second label. Interestingly the carA intensity ratio increases with a higher LimE focus-neighbour intensity ratio. In contrast, the detected carA foci (Figure 4.13 (B)) show that

there are also carA foci that have an increased LimE activity and are comparable to the LimE foci with carA as second label (Figure 4.13 (A)). However, there is also a group of carA foci which do not show increased LimE activity and which are separated by the described threshold. Further it can be seen, that the distribution of focus-neighbour intensity ratio in 4.13 (C) and (D) is close to 1 in vertical direction, representing no intensity increase. However, the applied threshold separates the bulk of the distribution from intensity outliers in positive vertical direction. This shows impressively that the selected threshold value enables to differentiate between foci with increased intensity in the second label from foci without detected increase. Due to the mentioned separation of the focus-neighbour intensity ratio by the threshold, the LimE and clc label combination is sorted in foci with larger and smaller second label intensity ratios. The resulting foci combinations are: LimE foci with increased clc intensity in the following referred to as LimE & clc Foci, LimE foci with no detected clc intensity increase in the following referred to as LimE Foci (clc), clc foci with increased LimE intensity in the following referred to as clc & LimE Foci and clc foci with no detected LimE intensity increase in the following referred to as clc Foci (LimE). Furthermore, the carA foci are also classified into groups, while the LimE foci with carA as second label are not splitted due to the missing distribution below the threshold. The resulting foci combinations are: LimE foci with carA as second label in following referred to as LimE Foci (carA), carA foci with increased LimE intensity in the following referred to as carA & LimE Foci and carA foci with no detected LimE intensity increase in the following referred to as carA Foci (LimE).

The results for the number of detected foci groups and the number of matrices in which at least one focus of the respective group has occurred are shown in Table 4.6.

| | # Images | # Foci |
|---|---|---|
| LimE Foci (clc) | 95 | 300 |
| LimE & clc Foci | 61 | 186 |
| clc Foci (LimE) | 86 | 648 |
| clc & LimE Foci | 53 | 126 |
| LimE Foci (carA) | 100 | 535 |
| carA Foci (LimE) | 61 | 122 |
| carA & LimE Foci | 79 | 219 |

Table 4.6.: Results for the detected foci groups. The number of images refers to the images showing at least one focus of the respective group and not the total number of recorded images. Foci, were extracted by the routine explained in section C.4 and are sorted into groups according to the intensity of the second label. Foci with 1.2 times higher intensity in the focus area are compared to the averaged adjacent pixels intensity are referred to as focus with colocalized focus at the second label.

### 4.2.4. Foci Properties

As property of the contact area, the number of detected foci in one image is evaluated. First, the number of foci per cell is compared between the actin foci detected with different secondary label or knock-out, with results shown in Figure 4.14 (A). In direct comparison the detected LimE foci with appropriate secondary labeling have a similar median value, although a significant decrease of the median is detected for the foci number of clathrin-labeld cells.

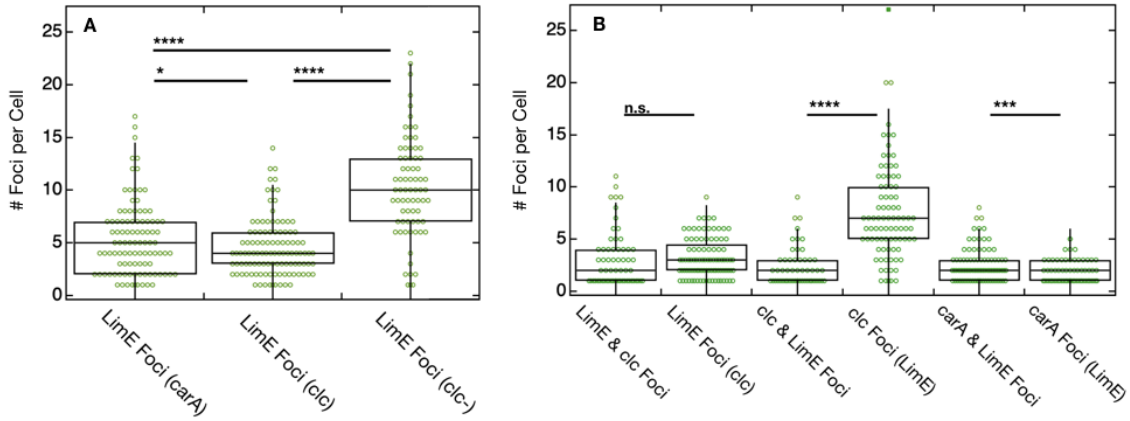


Figure 4.14.: Results for the amount of detected foci at the contact area and significance levels. Each point refers to the detected number of foci per cell. (A) shows the boxplots of the detected LimE foci with different second labels, which are listed in brackets. (B) shows the boxplots of the sorted foci, which are sorted by the routine described in Section 4.2.3. The representation of LimE foci (carA) in (B) is not included because it is already shown in (A).

The LimE labeled cells with clc knock-out shows a significantly increased number of 10 LimE foci per cell and thus a twofold increase compared to the median of the dual labeled cells. The boxplot parameter and results are listed in Table C.6.
Additionally, the number of foci per cell of the respective foci groups from Section 4.2.3 are compared, which is shown in Figure 4.14 (B), where each point represent non-zero elements of this group. The clc Foci (LimE) shows the most foci per cell compared to the other foci groups with a median of 7 and also shows a significant increase to the foci per cell median of 2 for the clc & LimE Foci, with further results listed in Table C.11. A significant difference in the distribution can also be observed for the carA label, where the median is constant for both distributions with 2 foci per cell, while no significant change could be observed for the sorted LimE foci with a median decrease from 3 foci per cell for LimE Foci (clc) to 2 foci per cell for LimE & clc Foci, with results listed in Table C.12 and C.10.
Furthermore the focus area could be calculated from the product of the number of existing pixels in the focus and the pixel area. The results for the LimE focus area

with different secondary label and knock-out are shown in Figure 4.15 (A), with results listed in Table C.7. Interestingly, the LimE Foci with carA as secondary label shows the smallest focus area median with 0.36 x$10^{-12}$m$^2$. With a median of 0.53x$10^{-12}$m$^2$, the focus area of the rescued cells significantly increase and knock-out cells show a significant increase with 0.45x$10^{-12}$m$^2$ to the LimE focus area with a carA label. While no significant difference can be detected between clc rescued and knock-out cells. The focus area shows a significant difference between all sorted

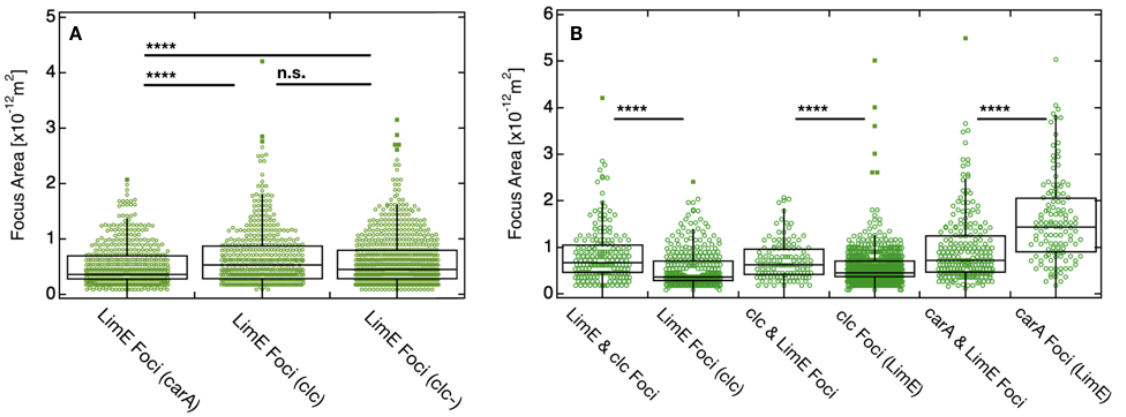


Figure 4.15.: Results for the area of detected foci at the contact area and significance levels. Each point refers to the detected number of foci per cell. (A) shows the boxplots of the detected LimE foci with different second labels, which are listed in brackets. (B) shows the boxplots of the sorted foci, which are sorted by the routine described in Section 4.2.3. The representation of LimE foci (carA) in (B) is not included because it is already shown in (A).

foci groups, shown in Figure 4.15 (B). The LimE and clc label combinations shows a decrease of the median area from 0.67 x$10^{-12}$m$^2$ for focus with colocalized focus to 0.36x$10^{-12}$m$^2$ for the LimE foci with results listed in Table C.13, and from 0.62 x$10^{-12}$m$^2$ for focus with colocalized focus to 0.45x$10^{-12}$m$^2$ for the clc foci with results listed in Table C.14. However, the LimE carA label combination shows an increase from 0.71 x$10^{-12}$m$^2$ for carA foci with colocalized focus to 1.43x$10^{-12}$m$^2$ with results listed in Table C.15. Interestingly the groups of, LimE foci, clc foci and carA foci, all with colocalized focus show a similar focus area median.

### 4.2.5. Height Distribution at LimE and carA Foci

Based on the sorting in Section 4.2.3, it is possible to distinguish between independent foci and colocalized foci. This and the next section focuses on the height distribution in the focus area and compares the height distribution between the different foci groups. While this section considers the LimE and carA dual label, the next section focuses on the LimE and clc dual label.

Since for each pixel not only the intensity information but also the height information for both labels are available, it is possible to visualize the height information in a 2-dimensional probability density map. This makes it possible to determine in which heights which label is active at the foci area and furthermore it is possible to set the heights of the labels in relation to each other. Furthermore, these information are also available for the foci adjacent pixels. This allows a comparison between the height distribution in the foci areas and the height distribution in the neighbouring areas. Therefore, 2-dimensional probability density maps are estimated to detect dependencies between the height information of both labels, which is plotted by the method mentioned in Section A.5 on a grid from 0 to 220 nm with an increment of 0.11 nm. The neighbours height distribution shows the distribution of the pixel adjacent to the foci. The combination of foci height distribution and neighbours height distribution is shown in Figure 4.16 (A) and (B) for LimE Foci (carA).

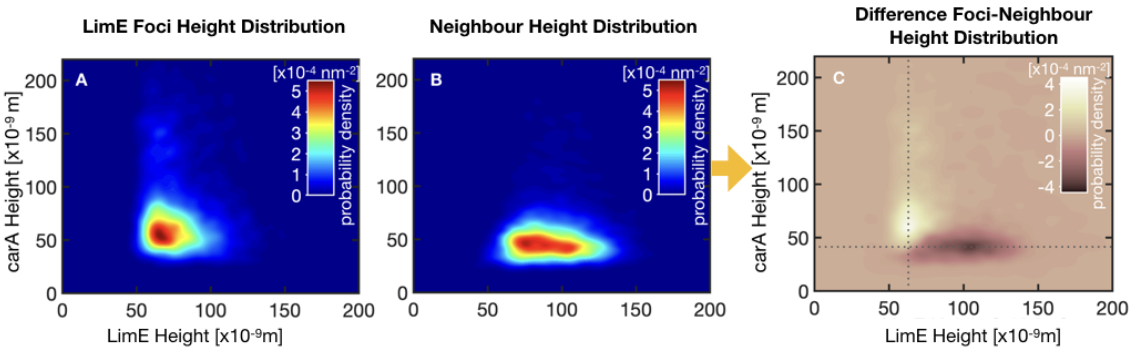


Figure 4.16.: Probability density map shows the height of the carA label against the LimE label height in reference to the substrate. The map in (A) shows the distribution for the pixels at the position of the detected actin foci and (B) shows the distribution for the pixel adjacent to the foci. (C) shows the difference between the LimE foci height distribution (A) and the neighbours height distribution (B). The dotted horizontal and vertical lines run through the local minimum and maximum of the map and are plotted for orientation purpose.

The maximum of the foci height distribution is at 65.9x10$^{-9}$ m for LimE and at 54.3x10$^{-9}$m for carA and thus LimE is 10 nm above carA for the most common pixel heights. The maximum of the neighbours distribution is at 75.6x10$^{-9}$m for LimE and at 46.3x10$^{-9}$ m for carA, indicating that while the membrane maximum of the neighbours distribution is closer to the substrate, the actin maximum is further away from the substrate, with results listed in Table C.8. These two maps describe the individual distributions. However, a comparison between the two maps is only possible in an indirect way. Consequently, it is not clear whether parts of the distribution are exclusively reserved for the focus distribution or whether they are also present in the neighbours distribution.
To be able to identify if areas of the foci distribution are more pronounced compared

to the neighbours distribution, the difference between the two distributions is drawn, which can be seen in Figure 4.16 (C) and is referred to as difference foci-neighbour height distribution in the following. The white areas show the parts of the distribution that mainly appear in the foci distribution and the black areas show the parts that mainly appear in the neighbours distribution. Regions that occur in both distributions receive a lower probability density. The dotted horizontal line is plotted through the minimum in carA direction at 41.7x10$^{-9}$ m, which nicely shows that the LimE distribution of adjacent pixels is spread around this value, results for the maximum and minimum of the difference distribution are listed in Table C.8. The range of the adjacent pixel distribution at the dotted line is roughly between $60 - 140$ nm. On the contrary, the positive range (white area, more pronounced

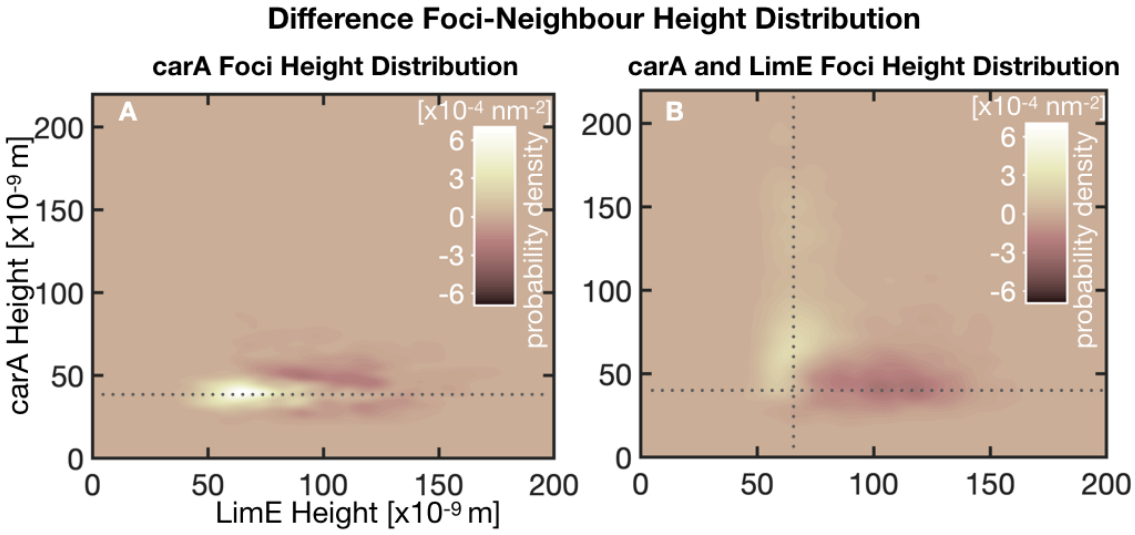


Figure 4.17.: Probability density maps of the difference between the carA foci height distribution and the neighbours height distribution of the LimE, carA label combination. (A) shows the height map of detected carA foci with no detected increase of the averaged LimE intensity at the foci area compared to the neighbour intensity, (B) shows the height map of detected carA foci with an increased average LimE intensity. The dotted horizontal line runs through the local maximum in (A) and the local minimum in (B) , while the vertical line runs trough the local maximum of the map.

foci distribution) of the difference plot is spread around the vertical line, running through the LimE maximum of the distribution at 62.8x10$^{-9}$m. The positive LimE distribution spans a much smaller value range between $40 - 70$ nm and thus much closer to the substrate. While the maximum of the membrane label is at 59.6x10$^{-9}$ m, which shows that LimE and carA are active at roughly the same height for the maximum and thus the most common point of the difference distribution. The carA distribution rang is up to 200 nm and thus well above the activity height of the

LimE label. Thus the plots shows, that at the foci area, the LimE activity is closer to the substrate than neighbouring regions are and that LimE is active at and below the height of the membrane label.
Furthermore, carA foci are detected and the above mentioned selection routine showed that two groups of carA foci exist, foci with increased LimE in the focus area and foci without. In order to analyze the height distribution of the respective carA foci group, the foci distribution and the neighbour distribution are estimated similar to the LimE foci (carA). In addition, the difference of both distributions is calculated again. For the reason of better readability, only the difference foci-neighbour height distribution is shown. The individual distributions are appended and can be viewed under C.16 and C.17. The results of the individual and the difference distribution are listed in in Table C.8.

The difference foci-neighbour height distribution for carA & LimE foci is shown in Figure 4.17 (B). The distribution shows many similarities to the difference foci-neighbour height distribution of LimE foci (carA). Examples of this are that in the focus area, actin is active closer to the substrate than in the neighbour area and that in the focus area the membrane is further away from the substrate than in the neighbour area. Furthermore the distribution shows that in the focus area, actin is active at the same level as the membrane or even closer to the substrate than the membrane. To detect the foci, the same images are analyzed for both labels. Thus it is possible that the LimE foci (carA) and carA & LimE foci group partly represent the same foci detected by different labels. This might explain why both distributions have a similar appearance.
Also, the difference foci-neighbour height distribution for carA foci (LimE) are determined, which can be seen in Figure 4.17 (A). The distribution shows a pronounced maximum at actin heights close to the membrane at $39.9\text{x}10^{-9}$ m for carA and $64.5\text{x}10^{-9}$ m for LimE. The neighbours distribution (black area) envelope the foci distribution (white area) for larger actin heights with its minimum at $50.2\text{x}10^{-9}$ m in carA direction and $91.5\text{x}10^{-9}$ m in LimE direction. Thus the membrane and actin distribution in the focus area is closer to the substrate than in the neighbour area. This behavior can also be observed by comparing the maxima of the individual foci and neighbour distributions, although this is less distinct (Table C.8).

### 4.2.6. Height Distribution at LimE and clc Foci

In addition to the LimE and carA label combination, a LimE and a clc dual label is selected and the intensity foci for the respective label are detected. The groups of foci with colocalized focus in the second label and foci without intensity increase in the second label are obtained according to the described sorting routine (Section 4.2.3). To analyze the label heights in the focus area, the height distribution in the focus area and in the focus adjacent area is calculated. To compare the height distribution in the focus area with its surroundings, the difference foci-neighbour height distribution is determined similar to Section 4.2.5, which is shown for all foci groups in Figure 4.18.

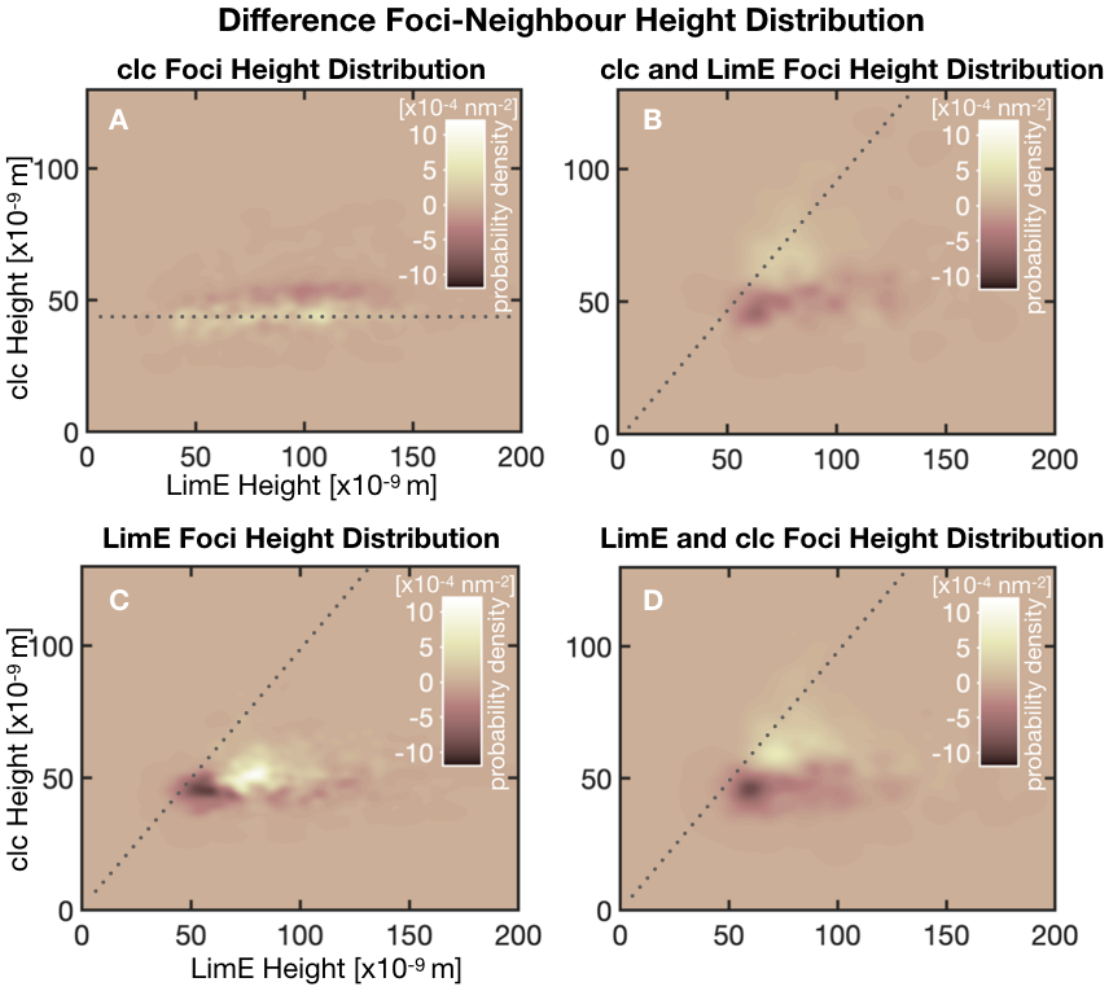


Figure 4.18.: Probability density maps of the difference between the foci height distribution and the neighbours height distribution for the different foci groups of the LimE, clc label combination. (A) shows the height map of detected clc foci (LimE), (B) shows the height map of clc & LimE foci, (C) shows the height map of LimE foci (clc), (D) shows the height map of LimE & clc foci. The dotted horizontal runs through the local maximum of the map and are plotted for orientation, the line with a positive slope shows the value where the pixel heights of both labels are located at the same height position above the substrate.

The individual foci and neighbour distributions can be found in the appendix, additionally the abbreviation (ind. dis.) refers to the individual distribution. The results for the maximum and, if applicable, minimum of the distributions are listed in the Table C.8. At first the clc foci are considered. The neighbour distribution in both cases extends from roughly $50 - 140$ nm, which is comparable to the neighbour distribution extent of the carA label. The difference foci-neighbour height distribution of the clc foci (LimE) is shown in Figure 4.18 (A, ind. dis. Figure C.11). The individual distributions show only a marginal difference between the maxima of the foci and neighbour distribution in the clc direction, where the maximum in the focus area is closer to the substrate. This detected difference becomes more visible in the difference plot, with a maximum at $43.8\text{x}10^{-9}$ m, shown as dotted horizontal line, and a minimum at $53.5\text{x}10^{-9}$ m. Furthermore, it is noticeable that the clc is more likely to appear closer to the substrate (white area) compared to the neighbour distribution (dark area) over the entire spectrum of actin activity.
The difference foci-neighbour height distribution of the clc & LimE foci is shown in Figure 4.18 (B, ind. dis. Figure C.12). The difference map shows the neighbours distribution as dark area at 50 nm in clc direction ranging from $50 - 140$ nm. The heights, which occur more often in the foci area, are shown as positive colorbar range. This range is visible between $55 - 100$ nm in clc direction, with its maximum at $64.4\text{x}10^{-9}$ m and is located above the dark area of the neighbours distribution. The dotted line indicate the position, where both labels are active at the same height. It can be seen that in a value range of $55 - 100$ nm in LimE direction, the dotted line intersects the part of the distribution assigned to the foci area. This means that in the foci area, LimE is partially active at the height of clc and that even clc can be found at a greater distance from the substrate than the LimE label. Therefore it can be said, that for clc & LimE foci, both proteins are active in a range from $55 - 100$ nm at the foci area and that the clc is active in higher distances from the substrate in comparison to the neighbours distribution.
Furthermore, the height distribution of LimE foci are examined. Interestingly, the difference foci-neighbour height distribution of LimE & clc foci, shown in Figure 4.18 (D, ind. dis. Figure C.14), has a similar shape as the clc & LimE foci distribution (Figure 4.18 (B)). Following the same argumentation as before, the agreement between the distribution of two foci groups, could be due to the fact that the same images have been analyzed to determine the LimE and clc foci. Thus, the same foci could have been detected by different labels. Comparable accordances are the neighbours distribution centered around the minimum clc value of $46.3\text{x}10^{-9}$ m ranging from $55 - 140$ nm in LimE direction, the occurrence of clc at the foci area at heights above the neighbour distribution and the clc occurrence at height and above the LimE activity for a LimE range from $55 - 100$ nm.
The difference foci-neighbour height distribution of the LimE foci (clc) is shown in Figure 4.18 (C, ind. dis. Figure C.13). Considering the distribution, it is noticeable that the light range also occurs between $55 - 100$ nm in LimE direction and is above the neighbours distribution in clc direction, with a maximum of $59.4\text{x}10^{-9}$ m to a minimum of $45.1\text{x}10^{-9}$ m. However, the height difference in the clc direction is less

pronounced than for the LimE & clc foci.

### 4.2.7. Height Distribution at LimE Foci of clc- Cells

Although the dual label combinations have already provided informations about the heights of the respective labels in the foci areas, it is not possible to directly compare this maps with the LimE label of clc knock-out cells. To enable a comparison between dual labeled cells and knock-out cells, the probability density function of the LimE heights in the focus region is determined for the different label combinations, LimE foci groups and the clc-, as shown in Figure 4.19. Furthermore, comparable to the two-dimensional case shown in the Section 4.2.5, the LimE height distribution of the focus adjacent pixels is estimated and the difference to the focus height distribution is drawn, which is shown in Figure 4.19 (B, ind. dis. Figure C.18 and C.19) for all LimE foci groups. The 1-dimensional PDF is estimated with the routine described in Section A.5 on a vector ranging from $0 - 220$ nm with an step size of 0.1 nm. The LimE distributions of the dual-label cells are only used for comparison

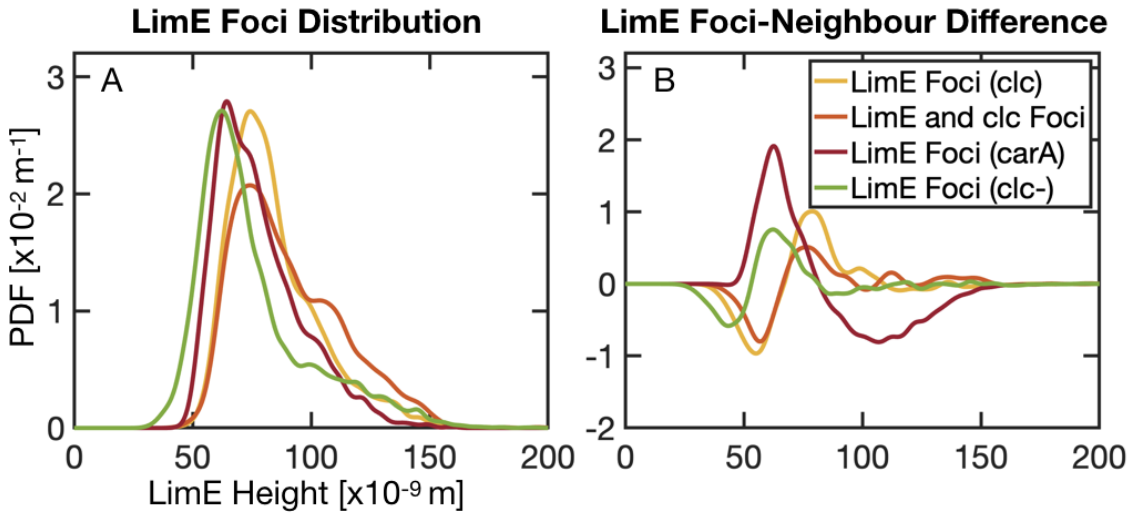


Figure 4.19.: PDF plots of the different LimE foci height distributions are shown in (A) and the difference between a LimE foci height distribution and the neighbours height distribution is shown in (B), for different label and knock-out combinations as well as for sorted points of an additional clc foci.

with the knock-out. The LimE distributions from the dual-label cells have already been described in the two-dimensional case and are not part of this section. If one compares the LimE foci distribution of the clc- cells with the other LimE foci distributions, it is clear that the maximum is closest to the substrate with $62.3\text{x}10^{-9}$ m. Considering the difference distribution (Figure 4.19 (B)), it is noticeable that the LimE distribution of the carA label, in the direction of increasing substrate

distance, shows a maximum and then decreases to a minimum afterwards. Thus, LimE in the foci area is closer to the substrate (positive probability density) than in the neighboring distribution (negative probability density). Furthermore, the other LimE difference distributions show less pronounced maxima and minima, indicating that the difference between the foci height distribution and the neighboring height distribution is less pronounced. Nevertheless, the minimum of the LimE foci (clc) difference distribution shows that the neighbour distribution is even closer to the substrate than the foci distribution.

### 4.2.8. Average Focus-Neighbour Height Difference

The difference foci-neighbour height distribution makes it possible to determine at which heights the respective labels are active in the focus area. While the comparison to the neighbour distribution allows to determine if the labels in the focus area occur at heights where the labels in the neighbour distribution do not occur and vice versa. However for this comparison, all pixels in the focus area must be pooled for all foci of the same group, the same applies to the neighbour distribution. Thus, the findings are valid for the entirety of pooled foci, but do not give evidence if the respective label of a single focus shows height changes with respect to its surroundings. Therefore, in this section the mean height in the focus area is compared with the mean height in the direct focus environment for each focus separately. To get information about

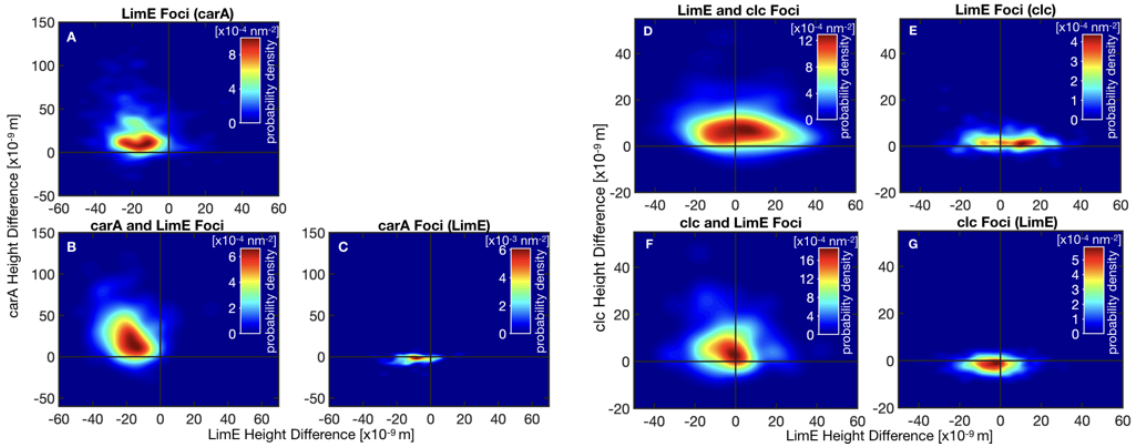


Figure 4.20.: Probability density maps of the height difference between the weighted average pixel heights at focus area and the weighted average pixel heights of the focus adjacent pixels. The horizontal axis shows the height difference in LimE direction, the vertical axis shows the height difference for carA (A-C) and clc (D-G). The height difference distribution is shown for LimE foci (carA) in (A), carA & LimE foci in (B), carA foci (LimE) in (C), LimE & clc foci in (D), LimE foci (clc) in (E), clc & LimE foci in (F) and clc foci (LimE) in (G).

the height change of a label in the focus area to its surroundings, the error weighted average height for the focus area and the neighbours area is calculated. Furthermore the difference between both values is calculated. For each focus the difference in height between focus and its surroundings is given for both labels. Now the 2-dimensional probability density function can be estimated for the height difference of all foci with KDE, which is shown in Figure 4.20 for the different foci groups. If the distribution is in the (I) or (II) quadrants of the coordinate system, hence in the positive range of the vertical axis, carA (A-C) or clc (D-G) in the focus area are on average further away from the substrate then their surroundings. Conversely, if the distribution is in the (III) or (IV) quandrants, the label is closer to the substrate in the focus area. If the distribution is in the (I) or (IV) quadrant, hence in the positive horizontal part of the coordinate system, LimE in the focus area is on average further away from the substrate than its surroundings. While it is closer to the substrate if the distribution is in the (II) or (III) quadrant.
The distribution of the LimE foci (carA) group (Figure 4.20 (A)) shows that the distribution lies almost entirely in the (II) quadrant. It can therefore be said that almost all foci of this group are further away from the substrate in carA direction and closer to the substrate in LimE direction, compared to the surroundings. The carA & LimE foci show a similar distribution (Figure 4.20 (B)). If one considers the carA foci (LimE), it appears that the distribution is located in the third quadrant. This means that carA and LimE are located on average in the focus area at lower heights relative to the substrate than in the surrounding area. However, the distribution is located close to the origin of the coordinate system, which means that the described differences are less pronounced than for the foci groups described before.
Now the LimE and clc label combination is examined, starting with the LimE & clc foci in Figure 4.20 (D). It is noticeable that the distribution is in the (I) and (II) quadrant, which means that for a large part of the foci, clc is on average higher in the focus area than in the surrounding area. Furthermore, this means that foci occure where LimE in the focus area is closer to the substrate ((II) quadrant) as well as foci, where LimE is further away from the substrate than their surroundings ((I) quadrant). A similar distribution can also be observed for LimE foci (clc), which is also located in the (I) and (II) quadrants, but the distance in clc direction to the origin is smaller, with results of the detected maximum of the distribution listed in Table C.16. The clc & LimE distribution in Figure 4.20 (F) is also mostly in the (I) and (II) quadrant, but it is noticeable that the distribution is more strongly represented in the (II) quadrant. It can therefore be said that for the majority of clc foci with colocalized LimE focus, clc and LimE are closer to the substrate than in the surrounding area. In addition, the clc foci (LimE), whose distribution is in the (III) quadrant, which means that for this group clc and LimE are closer to the substrate in the focus area than in the surrounding area.

The LimE label for the clc- cells is also available. To determine whether the LimE label of the knock-out is on average higher or lower than its surroundings, the difference between the mean height in the focus area and the mean height in the focus adjacent area is calculated. The PDF of the differences is calculated on a

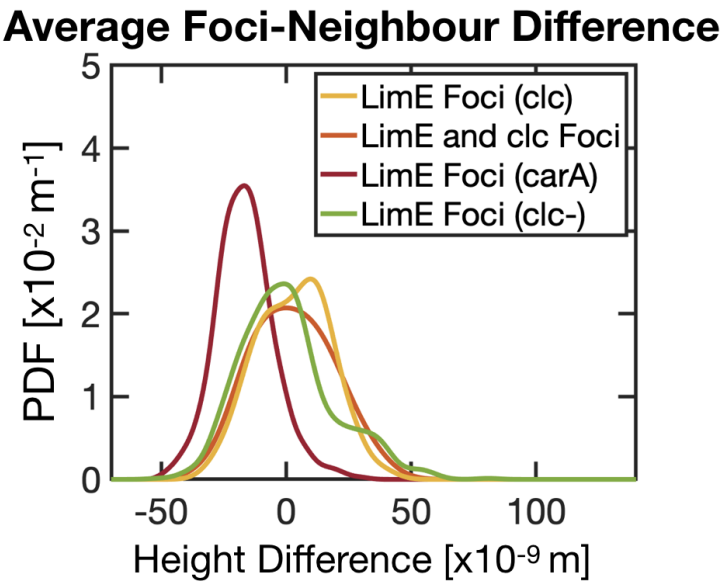


Figure 4.21.: PDF plots of the differences between weighted average height at the detected LimE foci area and the weighted average height at the detected neighbour area, for the LimE label of different label and knock-out combinations as well as for sorted points of additional clc foci.

vector from −150 to 150 nm with a step length of 0.01 nm for all LimE foci groups, which is shown in Figure 4.21.

While the distribution of LimE focus to neighbour difference with carA as second label shows the most differing behavior with a maximum at $-16.8\text{x}10^{-9}$m, the other three distributions are centered around the line of no detected difference. It can be said that although the distribution of the knock-out is centered around zero, for which no height difference between the average focus area and the focus adjacent area can be detected, the distribution shows that foci occur where the LimE is up to 40 nm closer to the substrate or further away from the substrate than the surrounding area.

Thus, by evaluating the average focus-neighbour height difference it is possible to determine whether the areas identified in the height distribution of the foci groups are generated by just a few individual foci or whether the entire foci group shows this tendency.

# 5. Discussion

The combination of AFM based SCFS with the systematic analysis of MIET height maps in the foci area allowed to investigate the influence of clathrin on the adhesion process, which is discussed in this section. Also, the height distribution of individual labels is discussed, before results of the foci detection are summarized. In the last section an exemplary dynamic behaviour for an active region is shown in a "timeline".

## 5.1. Impact of Clathrin Light Chain Knock-Out on the Adhesion Process

Upon the knock-out of clc, the SCFS based adhesion parameters can be compared between KO and WT cells. The height maps provide information on the activity range of the individual label and for the actin label in particular it enables the comparison of actin height distribution between WT and KO cells.

### 5.1.1. Step Parameters Reveal a Compromised Adhesion Cluster Formation

The maximum adhesion force, describes the maximum force that is opposed to the retracting cantilever before rupture events occur and the contact area is reduced, whereby the entire contact area contributes to the maximum adhesion force. The adhesion work, defined as integral over the force-distance curve, describes the work necessary to separate a cell from a substrate and is a measure for the extent of the discontinuous part of the curve. Interestingly, both parameters show a significant decrease of the median from WT NC4A2 to clc- cells. However, the comparison of the step parameters between WT NC4A2 and clc- cells shows only a significant difference in median step position (in force direction). While no significant difference was detected between the number of detected steps between wild-type and knock-out cells if at least on step was detected. However, only 45% of KO cells show at least one step, while for 75% of WT cells steps were detected, which shows that the probability of detecting adhesion clusters is reduced and thus hints at a disturbed adhesion process. The significant difference in step position is also clearly visible in the probability density map of the step positions (Figure 4.7). While the step appearance in the knock-out is limited to a smaller area around the origin, the WT spans a two fold larger area. The increased probability of step detection in the WT as well as the occurring probability density for step detection at a larger distance

from the origin contributes to the significantly higher adhesion work of the WT. This could be explained by the number of contributing adhesion clusters. If the WT cells expresses more adhesion clusters, the force per cluster would be smaller by the same applied constant retraction force, compared to cells with smaller amounts of contributing clusters. Thus the counteracting force to the clusters could be higher and therefore lead to a more extensive stochastic part of the force-distance curve. If more adhesion clusters are active at the contact area, it could increase the maximum adhesion force and thus could explain the differences between WT and KO in the box plots for adhesion work and maximum adhesion force.
The step force shows no significant difference between the distribution median for wild-type and knock-out cells. However, the $F_{Step}$ against l-Postion$_{Step}$ distribution (Figure 4.8) shows a possible bimodal distribution, with the $F_{Step}$ median in between. The high number of detected steps above 200 pN for the KO in comparison to its total number of 90 detected steps and the occurrence of two maxima around the median in the step force-separation map, are hinting at a malfunctioning adhesion cluster formation in the absence of clc. Thereby clatrhin can have an impact on the adhesion cluster in two ways; 1) through the absence of CME and the removal of adhesion proteins from the cluster, comparable to integrin endocytosis at focal adhesion points for mammalian cells [82]. The absence of CME and the associated regulatory function for the removal of adhesion clusters could lead to an adhesion clusters with increased lifetime, which could explain the increased occurrence of steps above 200 pN. However, it has been shown that although a light chain knock-out reduces clathrin assembly at the membrane, resulting in an increased number of cytoslic chc, a comparable rate of fluid-phase endocytosis to wild-type cells has been detected, whereas the chc- are defective [46]. This could imply that despite the lack of clc, at least for the fluid-phase endocytosis, clathrin coated vesicles could be formed. However, it has been shown that the clathrin light chain is involved in the endocytosis of some g-protein coupled receptors for mammalian cells [83]. It is therefore possible that the light chain is involved in the regulation of coat formation at the receptor cargo and that a receptor-based CME is only partially functional due to knock-out.
2) clathrin plaques were found as focal adhesion independent adhesion cluster for mammalian cells [21]. Thus it is possible, that the clc knock-out has an impact on the stability of the adhesion cluster. As described in Section 2.3.3, possible bond formation and cluster stability depends on membrane fluctuations and changes in the potential energy of the membrane due to membrane deformation by bond closure [29, 30]. However, since no extracellular interaction partner for vegetative D.d. adhesion proteins are known, which excludes a ligand binding similar to integrins, the adhesion of D.d. probably depends on DLVO interactions and is therefore distance dependent. For example, it has been shown that for substrates which enable a higher van der Waals interaction the $F_{Step}$ increases [2]. By coating an adhesion cluster, clathrin could for example reduce membrane fluctuations and thereby stabilize the adhesion region. This can explain the distribution below the median. The step force -separation map also shows the occurrence of step forces up to about 50 pN with

a high probability density, which are not as prominent in WT maps. This further supports the argument of unstable adhesion clusters. By a not fully functioning clathrin assembly, the adhesion cluster formation could be more susceptible to membrane fluctuations and thus ruptures earlier under constant retraction force. However, observation of the assembly structure of clathrin-coated plaques for HeLa cells, by rapid freezing of the cell and observation with an electron microscope, revealed defects in the hexagonal lattice formation of the flat coating structures [84]. It has been suggested that clathrin plaques form on rigid substrates due to strong integrin-ECM binding as a kind of frustrated endocytosis, preventing clathrin budding [21]. Thus it is possible that the prevented invagination of the clathrin coat causes the described defects in the lattice, which contradicts the stabilization theory of the clathrin coat at an adhesion cluster. To investigate the influence of a possible clathrin coat on *D.d.* adhesion clusters, additional SCFS experiments on substrates of varying stiffness could provide further information.

### Force-Distance Curve Section Uncovered by Step Detection Routine

Considering a FDC, it is noticeable that between the maximum adhesion force and the first detected step, events may occur, which are not detected by the routine because the step is too small and may therefore rated as a bad step because of the nonzero slope in between steps. It is possible that smaller adhesion clusters are located in this region of the FDC and cannot be detected due to their smaller size. In

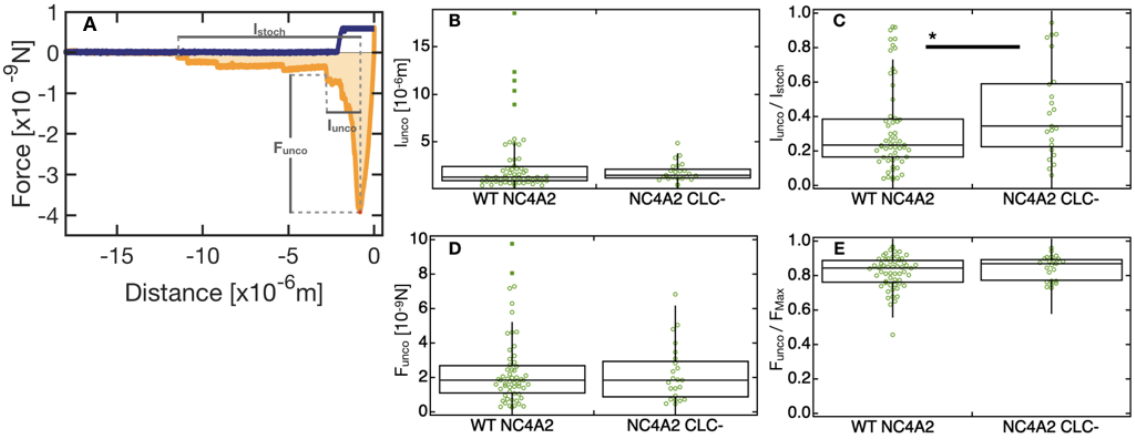


Figure 5.1.: (A) shows a exemplary force curve with marked calculated parameters. The box plot in (B) shows the distribution for $l_{unco}$, while (C) shows the distribution of the ratio between of $l_{unco}$ and $l_{disco}$. The box plot in (D) shows the distribution for $F_{unco}$ while (D) shows the distribution of the ratio between $F_{unco}$ and $F_{Max}$.

order to place this range in the context of the stochastic part of the force-distance curve, the difference between the position of $F_{Max}$ and the position of the first detected step is calculated for all curves, which have more than one step, which is

exemplary shown in Figure 5.1 (A) as $l_{unco}$ and $F_{unco}$. The results for the respective direction is shown in Figure 5.1 (A) and (C). Furthermore, the difference between the pulling length and the position of the maximum is calculated, which represents the length of the stochastic part $l_{stoch}$ of the force distance curve. The ratio between $l_{unco}$ and $l_{stoch}$ gives the proportion that the uncovered area has on the stochastic part of the FDC, which is shown in Figure 5.1 (B). The ratio between $F_{unco}$ and $F_{Max}$ represents the portion of the uncovered area in force direction and is shown in Figure 5.1 (D).
Interestingly, no significant increase in the median of $l_{unco}$ can be detected and the WT shows more outliers and far outliers. However, the knock-out distribution starts with higher $l_{unco}$ values, thus the KO distribution is shifted with reduced $IQR$. The results are listed in Table D.1. The $l_{unco}/l_{stoch}$ ratio shows a significant increase of the median value from 24% to 35% for the KO. This impressively shows that, although no significant difference between the medians of the uncovered areas was detected for both cell types, this area has a much larger proportion in the stochastic part of the FDC. Considering the difference of the force curve in force direction does not show any significant differences. Although it is not certain whether steps occur in this part of the FDC and further this method does not allow the detection of possible developing or less developed adhesion clusters, it clearly shows that the uncovered area of KO cells makes up nearly half of the stochastic part and thus contributes a large part to the adhesion work.

### Size differences for Clathrin Light Chain Knock-Out Cells

By the detection of the cell diameter at a state of slight compression, a significant increase in cell diameter was detected for clc KO cells. Osmoregulation problems have been described for clc- and especially for chc-, where cell lysis was observed after half an hour in a low osmotic environment of water for chc KO, whereas the clc- cells remain rounded with pseudopodia formations visible [46]. This osmoregulatory problem can be attributed to non-functional contractile vacuoles of the cell, whereas clc knock out cells show enlarged contractile vacuoles comparable to the KO of the adaptor protein AP180 [85]. Knock-out cells picked and adherent to cantilever show pseudopodia formations and movement on the cantilever between force curves. It was shown that also developed, chc- cells shows movement in buffer while they where described as rounder [86]. To reduce possible effects of osmotic swelling on the adhesion of clathrin mutants, an incubation of cells into a buffer presenting a more hospitable surrounding was proposed for chc- cells in [45] might also be useful for clc- cells. However, changing the buffer standardized for step spectroscopy would also mean a change in ionic strength and since *D.d.* shows reduced adhesion under increasing ionic strength [2], only a comparison between wild-type and knock-out in the same buffer would be possible.

### Comparison of the WT NC4A2 Adhesion Properties with Previous Publications

Since the evaluated force curves were performed with the same SCFS parameters under comparable conditions as in previous publications [2, 8, 39], a comparison of WT results is possible. In comparison to AX2, AX3 and DH1 evaluated in [39], the NC4A2 show major differences with a reduced number of steps, pulling length, maximum adhesion force and adhesion work, which are dependent on the number of detected steps as already mentioned. The force curve parameter which is of similar value to the other WT cells is the step force. It was stated by Bloomfield *et al.* [87], that phenotypic differences detected between the different strains might emerge due to their genetic variation. For example, different adhesion properties between AX2 and AX4 strains on adhesion-reducing substrates were observed [68]. The NC4A2 is said to be an axenic strain independently isolated from its parental strain NC4 [88]. While NC4A2 has some genetic differences to NC4, it contains a chromosome 2 duplication, which was also found in AX3 and strains that originated from it, for example DH1 [87]. However, it was found that NC4A2 appears to be more motile in the vegetative state then AX3, while both strains show opposite behaviours with the knock-out of pirA, a regulatory protein associated with SCAR. This results in a rounder appearence with less pronounced pseudopodia for NC4A2, while the knock-out in AX3 result in increased activity in pseudopodia formation and motility [89]. It also has been shown, that with increasing number of actin foci, cell velocity decreases [18]. In combination with the high colocalization of SadA to actin foci with 96% [39], it shows a possible correlation between the reduced number of detected steps and the increased cell motility for NC4A2 in comparison to the other WTs.
The detected step parameter of WT NC4A2 cells show outliers with increased values, however the majority of FDC shows less adhesion and thus a decreased probability to find cells of similar adhesion properties to the other WT cells. The parameterization of SCFS parameters was performed on AX3 cells [51]. With the detected difference in adhesion parameters between NC4A2 and AX3 cells, differences in the parametrization of NC4A2 cells might be detected which would require adaptation for this cell type in future work.

### Outlook for SCFS

The applying of 2-dimensional probability density functions allows to visualize possible correlations. While a significant difference was detected for one parameter in the 1-dimensional representation, the density maps enables the detection of a decreased range for KO cells where steps can occur and identifying an area where tethers are likely to occur. In addition, the method shows a bimodal distribution of the step force, which was not noticeable in the box plot. For example, for cells with integrin-based adhesion, it was possible to distinguish between jumps with a cytoskeletal anchor and membrane tethers due to dependencies between the slope before the

step discontinuity and the step position [79]. In the case of clathrin plaques for example, a cytoskeletal anchor to clc is needed for them to occur [84]. Especially the knowledge whether a cytoskeletal anchor was present for the step could thus be of interest for further anaysis of clathrins, impact on D.d. adhesions clusters.

### 5.1.2. MIET based Height Profiles at the Contact Area

MIET provides a momentary image of the intensity and height profile of fluorophores up to a height of 200 nm above the substrate and thus the corresponding height matrices of the contact area. By combining MIET with dual label microscopy, it was possible to determine the heights of actin, clathrin and/or the membrane at the contact area. For the analysis of the height distributions, the recorded contact area was segmented to exclude vacuoles, possible height changes of the cell contour and areas of increased actin activity in pseudopodia formation. The resulting height profiles for the respective labels are thus estimated from the fluorescence label heights within the cytosolic region of the contact area.
The carA label as transmembrane protein was used to track the height of the plasma membrane. The averaged height distribution, as well as its error range, starts at about 25 nm (Figure 4.11 A). This shows that the error range and thus for all individual carA height density distributions the minimum carA label-substrate distance is limited to this value. The carA label height density distribution shows a long tail, which reaches up to about 100nm. The standard deviation as a marked range of error around the averaged density function, shows that the long-tail region differs widely between the individual PDF. This long-tail may indicate membrane invaginations in the area of clathrin structures. This is further supported by the height distribution in the carA foci region (Figure 4.16 (C)), which shows membrane heights above 70 nm and thus in the area of the long-tail. Furthermore, it is possible that the contour extent of the cell matrix was chosen too small, this could result in the detection of the cell curvature at the periphery of the contact area and also contribute to the long tail.
The height density distribution of the clc label starts about 10 nm above the carA label at 35 nm. This difference can also be seen in the height difference of the moduli, where the clc label is 5.5 nm above the carA modulus. Although clathrin coats the membrane in some areas, there is a height offset between the minima of the substrate to label height differences for the two fluorescence label. It should be mentioned, that the clc label is embedded in a clathrin triskelion and thus the spatial structure of the triskelion creates a height difference to the membrane. Furthermore, clathrin coat assemble via adaptor proteins, which in turn can bind to the intracellular end of a transmembrane protein.
The fluorescent label of the carA is fused to the intracellular end of the transmembrane protein. Thus, the resulting carA height does not represent the direct membrane height, but instead is the sum of extracellular membrane to substrate distance, membrane thickness, height difference due to the intracellular structure of the carA receptor and fluorescent marker size. Assuming that both fluorescent markers have

a similar size and that the adaptor protein binds to a comparable intracellular transmembrane structure, the height difference between carA and clc labels can be assumed as the height differences generated by the adaptor protein and triskelion structure. Due to the measured label combination, no direct relative height difference between both label is available and only an indirect comparison between both height density distributions is possible.

### Actin Possibly Compensates for the Lost Clathrin Function

Because a LimE label was used in all three cell types, a comparison of the LimE label height distribution between the different label and knock-out combinations is possible. The same fluorescent marker was used for all LimE labels that are compared, thus avoiding possible differences that may occur due to different fluorescent markers [39]. The LimE & carA label combination, can be described as unbiased in terms of clathrin functionality, compared to clc labeled or knock-out cells. The LimE PDF of this label combination is distributed from roughly $50-150$ nm (Figure 4.11 (B)). Although the LimE PDF of the clc- also reaches up to about 150 nm, the distribution starts at about 30 nm and thus much closer to the substrate than the previous case. Furthermore, the modulus of the averaged LimE PDF is 47.7 x $10^{-9}$ m closer to the substrate for the clc- cells.
In summary, it can be said that the LimE label of the clc- is active much closer to the substrate and thus also to the membrane. Although the upper limit of the value range is comparable to the LimE & carA dual label case, the range for the knock-out is only found as a long-tail with low probability density. The average actin activity shifts towards the substrate and could show a possible compensation attempt of the knock-out, to counteract the loss of clathrin function. Actin could be applied close to the membrane to stabilize adhesions clusters and to reduce membrane fluctuations at the ventral cell side.

### Rescued Clathrin Cells vary in their Actin Height Distribution

The LimE distribution with clc shows a mixture of both distributions with a range which starts between both distributions at roughly 43 nm and ranges up to 150 nm. It also shows two maxima, one close to the maximum of the knock-out and a second close to the miximum of the LimE & carA label combination.
Due to calculating the average of individual PDF, a multimodal distribution can occur because each individual height density distribution is multimodal. Furthermore, it is possible that PDFs are grouped around different moduli, thus the calculated average would contain the maxima of all the respective groups of PDF. The moduli distribution (Figure 4.12), as a distribution of the moduli heights for all individual PDFs, was created to investigate a possible multimodal distribution based on grouping of individual PDFs moduli at certain height values and if this is the case, to determine the average group height. This distribution shows that for the knock-out almost all PDF moduli are centered around an average value, while the LimE & carA label

combination has two groups that are visible in the averaged PDF as a possible bimodal distribution. Since for the LimE & clc label combination an mRFPmars clc label was inserted into the KO, it was expected that the LimE height distribution is similar to that of the LimE & carA label combination. Nevertheless, for the moduli distribution of the LimE & clc label combination, three maxima are detected in comparable positions to the maxima of the LimE & carA and LimE with clc- distributions, for comparison see Table 4.4.
The clc label appears in a variety of intensity profiles ranging from low background intensity with prominent foci to high average intensity where no foci could be detected, which is exemplary shown in Figure 5.2 (A). Because no foci determination was possible for these cells, the average height profile of these 4 cells is determined with the method used in Section 4.2.2, which is shown in Figure 5.2 (B). The clc

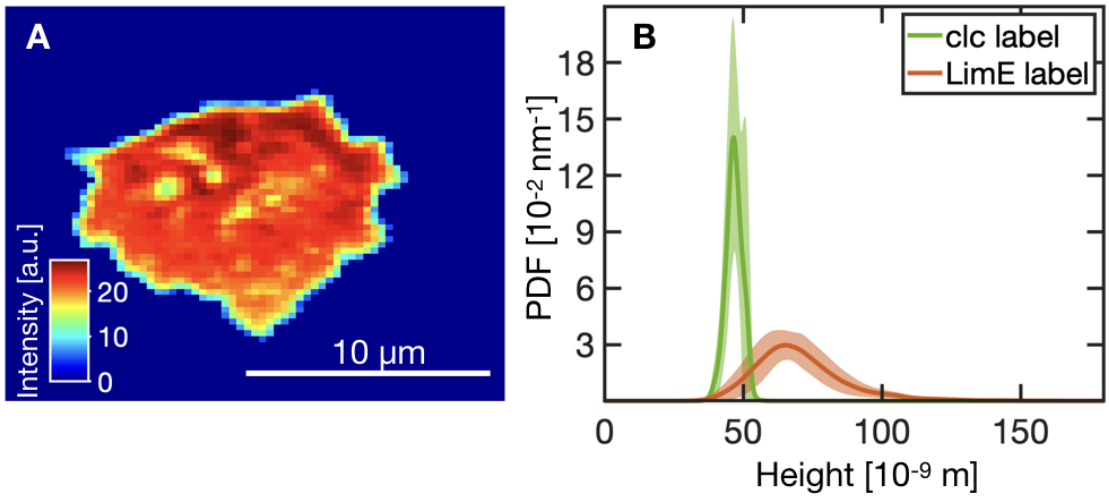


Figure 5.2.: The micrograph in (A) shows an exemplary intensity image from the clc label to which the foci routine was not applicable and (B) shows the height distribution as PDF for the clc and the LimE label for the cells sorted out.

label modulus of the averaged PDF function is with $(46.6, +4.8, -2.3)$ x$10^{-9}$m at the same height as the average of all PDF with $(46.5, +5.2, -3.6)$ x$10^{-9}$m. All the actin PDF of the selected cells, show their median close to the average median of $(65.2, +10.9, -11)$ x$10^{-9}$m, which is visible on the standard deviation area around the averaged PDF. The height distribution of the selected cells show the most frequent pixel height at the range of the first fitted Gaussian curve, (Figure 4.12 (B)) and thus show a comparable height distribution to the LimE label in the clc- cells.

Due to the comparable actin height distribution to the clc- and the unreasonable detectability of foci, there is the possibility that the rescue was not successful for these cells and that the light chain functionality is limited. This is additionally reinforced by the fact that for cells with LimE & carA label combination and without

a tampered clathrin apparatus, the actin range begins at higher values and the maximum of the first fitted Gaussian function is not present. Therefore the cells were excluded from the clc foci detection routine.
A possible explanation for the cells under consideration could be that the fluorescence label influences the function of the clathrin structure. It has been shown, that labelling of actin and myosin associated proteins affect the adhesion properties and cell phenotype [68]. An affected clathrin function due to a fluorescence label would, however, influence all cells. Furthermore it was shown that a fluorescence labelled light chain restores the phenotype of clc- and that the clc label appears in clathrin punctae [41]. Nevertheless, the clc label appears in different background intensity levels, ranging from cells with low background intensity and clearly definable foci, cells with medium intensity and still detectable foci and cells with high intensity for which no foci detection is possible. These background intensity levels vary in most cases from cell to cell. This would also allow a transition from a state with scattered and isolated clathrin punctae to a state with constant activity.
The excluded cells show impressively the variability of the label and that the exclusion of the images is useful in the analysis of clc foci. As a further step, it would be useful to sort the clc labeled cells into groups depending on their background intensity and consider them separately. In this way it would be possible to determine foci in cells with a low background activity comparable to the carA labeled cells with an enlarged matrix section, in order to determine the low intensity clc regions more precisely, comparable to the detection of carA foci which is described in detail in Section C.4. Additionally, it would allow to consider foci determined with a higher accuracy separately in order to exclude foci detected under possible phenotype changes due to a limited functioning rescue or a change of cellular state.

### 5.1.3. Foci Analysis of Clathrin Light Chain Knock-Out Cells

The observation of actin foci at the contact area by MIET, shows a signifcant increase in the number of detected foci per image for the KO (Figure 4.14 (A)). Also a significant increase in the foci area can be detected to LimE foci with carA as second label (Figure 4.15 (A)), both detected by the foci routine with same routine parameter. In the absence of the light chains, clathrin triskelion can still be formed but the number of heavy chains assembled on the membrane is reduced [46]. The increased number of detected actin foci can hint at a compensation effect, where the establishment of adhesion cluster or an endocytotic engulfment is attempted. Kamprad *et al.* found a comparable behaviour for a knock-out of SadA, by detecting a reduced number of steps and an increased number of actin foci [39]. Thus clc-cells show a comparative strategy to cells stripped by their major adhesion protein. The foci height distribution revealed (Figure 4.19 (A)), that the maximum of the LimE height distribution is closest to the substrate for the KO. However, the neighbours distribution show pixel with an actin activity even closer to the substrate. The actin label gives information about the general distribution of actin heights and clearly shows that for the KO, actin is active closer to the substrate to possibly

compensate for the loss of clathrin involvement in adhesion clusters. However, the foci analysis does not provide any clear evidence. An additional carA label for the LimE labeled and clc- cells could be useful. The carA label could help to detect if the actin activity closer to the substrate is accompanied by a general membrane height change for the knock-out. Further it might give evidence if the actin activity at the foci area implies an attempted endocytosis or a stabilization of adhesion clusters.

## 5.2. Height Profiles of Various Foci

By determining the intensity focus area and the MIET based information on the pixel intensities and heights in the focus area of the dual label, it was possible to differentiate between foci groups. Based on the fact that the clathrin focus occurs first, it is possible, in the case of the LimE & clc label combination, to classify the detected groups into temporal segments of the clathrin-actin colocalized focis, which is discussed in the next section. This assignment is not possible in case of the Lime & carA label combination, which is why the height density maps represent the entirety of the LimE foci. Areas of increased carA intensity were found, independent of the

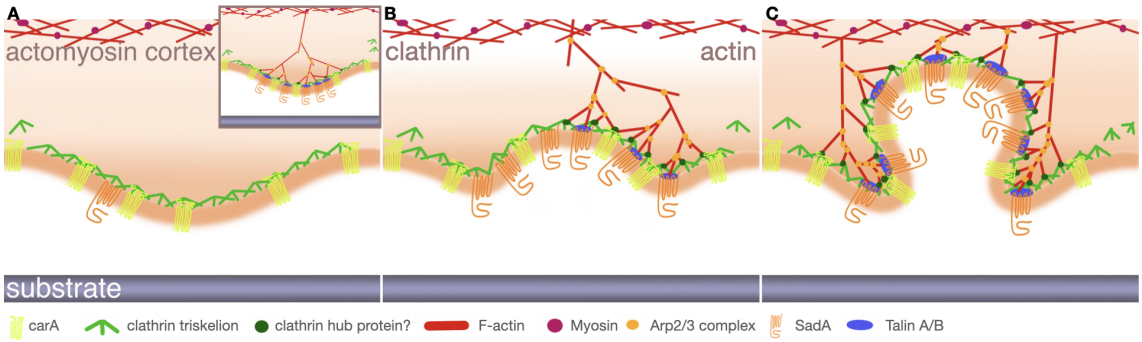


Figure 5.3.: A schematic drawing is shown to illustrate the findings.(A) shows the detected height change of the clc foci as clathrin coat assembly, which can also be accompanied by a membrane height change. The zoom-in window shows a possible assembled adhesions cluster, as a possible intermediate step to pit formation. (B) shows the pit formation. It is divided into the clathrin side, which emphasizes the clc height change compared to its surroundings and the actin side, which is active at the level of clathrin. (C) shows the advancing CME. The carA receptors in the pit are located above the actin activity at the edge. A clathrin coat is also present at the edge of the pit.

LimE signal, which are discussed together with the LimE & carA foci in the later section. Furthermore, it was possible to record time series of a living cell, which allows to consider areas with increased foci activity over a longer period of time, which is addressed in combination with an outlook at the end of the discussion.

Based on the results of the foci height analysis, a schematic drawing was created that summarizes the results, which is shown in Figure 5.3.

### 5.2.1. Focal Region Intensity Correlation Enables Grouping of States of the Foci Timeline

Starting with the clc foci height density distribution without increased LimE activity. The foci- neighbour difference distribution (Figure 4.18 (A)) shows that over the entire actin range, clathrin in a focus is active closer to the substrate than in its surroundings. Although the difference in height between the maxima of the foci and neighbour height density distribution is not as pronounced (Figure C.12), the difference between these two distributions shows that in the foci region clathrin is more frequently closer to the substrate than in the neighbour region and that a height difference of 10 nm is detected between the maximum and minimum of the difference distributions. This detected change in height can be explained by the fact that the clathrin coat and the membrane in the foci area are closer to the substrate. However, it is also possible that the coat assembly in the focus area result in a height difference from the cytosolic clathrin triskelion in the neighbours distribution to the assembled coat in the focus area. Previous TIRFM based analysis of height changes around the actin foci showed that the membrane around the focus is closer to the substrate [18]. Furthermore, a membrane substrate distance approach was detected during the clathrin foci appearance [39]. Thus the result of clathrin assembly closer to the substrate at the position of an clc foci are supported by previous findings. Therefore the schematic drawing in Figure 5.3 (A) shows both scenarios of a membrane and clathrin coat height change and of an assembling coat at the focus adjacent area.
The distribution of the difference between the average focus and the average focus adjacent pixel height (Figure 4.20 (G)) shows beside a clathrin height change also an actin height change towards the substrate. The distribution of averaged actin focus height to averaged adjacent pixel height goes up to $-20$ nm and thus is showing a much larger change in height than in clc direction, where a small average height change is detected. Considering that in the foci height density distribution for a constant clc height, LimE occurs in a range of $50-150$ nm (Figure 4.18 (A)), it can be argued that clathrin's height change occurs independently of the actin label. If one assumes that clahrin's change in height is produced by actin, this would mean that actin is active at the level of clathrin. But this would not explain the actin range of $70-150$ nm and thus an activity of $30-110$ nm away from the clathrin label. However, since there is also an actin height change, it can be argued that this height change occurs after the clathrin height change. This is illustrated in the schematic drawing by the micrograph (Figure 5.3 (A)), which is placed after the coat assembly and before beginning endocytosis.
The difference foci-neighbour height distribution of clc foci with LimE colocalized focus (Figure 4.18 (B)) shows that the foci height distribution in clc direction is above the neighbours distribution. Further it is noticeable that the actin activity is

limited to a range between $60 - 90$ nm and additionally that in this range actin is active in a height close to the clc activity. The dotted line indicates, that the LimE activity is also detected at heights closer to the substrate then the clc activity. In a direct comparison of the clc foci and the clc foci with colocalized LimE focus distribution (Figure 4.18 (A) and (B)), it is noticeable that the maximum of the distribution with detected LimE activity lies 20 nm further away from the substrate. These height changes are also included in the schematic drawing (Figure 5.3 (B)). In the clathrin area one can see that the clathrin coat in the pit formation lies over the surrounding area. Also the height change from membrane protrusion (A) to the beginning pit formation is shown. On the actin side it can be seen that actin is active at the same height as the clathrin coat. The average difference distribution (Figure 4.20 (F)) is placed in the graph, in the area of a positive clc height change and thus also shows that the average clathrin in the foci region is higher than in its surroundings. In summary it can be said that the focus range is higher compared to its surroundings and that actin is active at high levels of clathrin. This is also shown in the 3-dimensional reconstruction of the height map of a focus area in Figure 5.4 (A) and (B). While the height of the clathrin label decreases from edge of the map to center, two points are shown in the map center where the clathrin label is higher than its surroundings and points into the cell interior. The actin shows a comparable behaviour and seems to envelop the clathrin pit.
The clc foci with colocalized LimE focus and LimE foci with colocalized clc focus groups contain presumably large proportions of the same foci, which were detected by different labels. Interestingly, both groups show similar results with clc activity in the focus area above the neighbours distribution and an actin activity close to and below the clc heights.
The group of detected LimE foci without an increased clathrin activity is a mixture of foci not correlated to a clathrin focus and foci which correlate with clathrin focus, but where the clathrin focus is no longer present. Heinrich et al. found by individual tracking of clatrhin and actin foci that clathrin foci arise independently of actin foci but disappears after an actin focus arises at the same spot and that more than 80% of actin foci coincide with clc foci [59]. Based on coincidence value of 80% and the total number of detected LimE foci with clc as second label, roughly 2/3 of the foci in this group should have coincide with a clc focus. LimE at the foci area shows its activity in the range $60 - 100$ nm (Figure 4.18 (C)). The maximum in clc direction is still further away from the substrate then the minimum of the neighbour distribution. However, this difference is less pronounced than the difference in the LimE foci with a colocalized clc focus distribution. The LimE foci with colocalized carA label show membrane heights up to 180 nm (Figure 4.16 (C)), which are not shown in the LimE foci (clc) distribution. This difference could be explained by the theory that the clathrin coat is also active at the narrowed part of the pit formation and thus shields the detection of higher lying areas which is why the clathrin coat in Figure 5.3 (C) is also shown at the necking region.
It was discovered, that the averaged intensity maximum of clc foci appears 15 s before the averaged LimE foci intensity maximum. Foci observed with TIRFM in

combination with reflection interference contrast microscopy reveal that the membrane substrate distance shrinks with clathrin foci appearence and that with appearing actin foci, the clathrin foci disappears and afterwards the membrane-substrate distance increased again [39, 90]. Considering the number of detected foci per image (Figure 4.14), it is noticeable that clc foci occur 3 times as frequently as clc foci with colocalized LimE foci. This difference can be explained by the fact that a clathrin focus can appear a variable time before the actin focus and that the temporal overlap of both foci is comparatively short, whereby on average fewer clc foci with colocalized LimE focus could be detected.

### 5.2.2. carA Label as Marker for Membrane Height Changes

As already mentioned, while for the LimE & clc label combination it is possible to determine if a LimE and clc foci are colocalized, this distinction is not possible for the LimE & carA label combination. As described in the case of the clathrin label, actin and clathrin are active at comparable heights. Similar results are also detected in the difference foci-neighbour height distribution of the LimE foci with carA as second label (Figure 4.16 (C)). The central distribution has an actin activity between $55 - 90$ nm and the maximum at $62.8\text{x}10^{-9}$ m in LimE direction and $59.6\text{x}10^{-9}$ m in carA direction. The difference in height between maximum and minimum of 17.9 nm in the membrane direction shows that membrane height at the foci area is above the neighbours height. The membrane shows for a large proportion of the difference distribution an actin activity below its heights. The carA label is detectable at a height of up to 200 nm above the substrate and thus up to roughly 140 nm above actin activity. This is also exemplary shown in the 3-dimensional reconstruction of the LimE foci area in Figure 5.4 (C) and (D). In the central part, it is clearly visible that the membrane is invaginated and forms a pit, while the actin is active at the location closer to the substrate compared to its surroundings. It remains to be mentioned that the height detected by MIET represents an average of the fluorescence protein heights in the pixel area. The height detected here can either occur, by an invaginated membrane where actin is active at its edges or due to an endocytotic vesicle, whereby this requires that the carA receptor is only present in small quantities in the closed membrane area below the vesicle. Tubular like membrane invaginations were found for yeast cells with a diameter of up to 50 nm, a length of up to 180 nm and a clathrin coating on the tip, what is comparable to the membrane heights found in the focus area [91]. The CME vesicle diameter ranges between $50 - 100$ nm, the diameter for example was estimated as 50 nm for *D.d.* from fluid uptake [50]. This in turn shows that the vesicle and tube diameter cannot be resolved by the pixel size of $250 - 300$ nm. Instead the pixel represents an averaged height of the fluorescence proteins closest to the substrate in the pixel area. Nevertheless, in combination with the results from the LimE & clc dual label, it is impressively shown that in the area of the LimE foci, clathrin coated membrane invaginations and possible CME occure. Furthermore, it is shown that actin is active

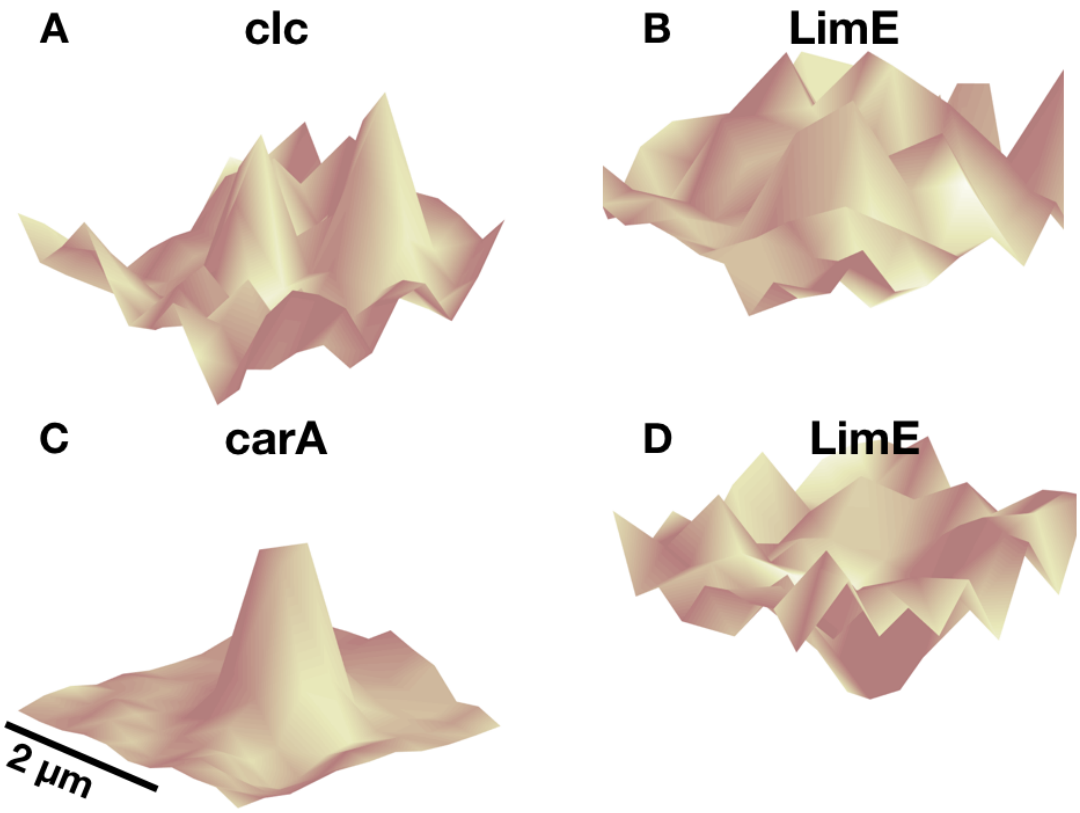


Figure 5.4.: 3-dimensional reconstruction of the fluorescent marker height at a focus area, with the focus at its center. (A) and (B) shows the respective label for a LimE focus with colocalized clc focus, while (C) and (D) show the respective label for a LimE focus with carA as second label.

in the area of the focus below the membrane and thus possibly drives the membrane invagination and the vesicle transport.
The carA label was chosen as an indirect label to gain height information of the membrane, thus the label was not originally intended to detect areas of increased activity or intensity foci. Xiao *et al.* have shown that the carA label of the developed *D.d.* is uniformly distributed on the cell membrane, although randomly occurring points with increased intensity were detected. In addition, by a 3-dimensional reconstruction an uniform distribution at membrane folds was observed [69]. The MIET observation is a 2-dimensional projection of the fluorescence label distribution. By assuming a uniform distribution, membrane folds, endocytotic cups or possible adhesion structures can lead via height changes to regions with a higher membrane surface and thus increased carA receptor concentration. For example, the projected area of a sphere would contain 4 times ($\frac{4\pi r^2}{\pi r^2}$) the membrane area and thus lead to an increase in intensity. This is also visible in the average focus to neighbour intensity ratio shown in Figure 4.13. The LimE foci and clathrin punctea ((C) and (D)), show a central distribution, while outliers of increased intensity are visible away from the

substrate in y-direction. However only the LimE/carA focus combination shows that with increasing ratio in LimE direction the carA ratio also increases. Under this assumption, the carA intensity was used as marker for membrane activity, to track regions of possible height changes. Furthermore, Islam *et al.* showed that carA also occurs in the vegetative state and is involved in the activity of G proteins [7]. It would be possible for carA receptors to occur as cluster in the area of the LimE foci. This could mean that actin foci serve as a signal platform, while the height change shows that carA receptors removed from the substrate by possible CME. It has been shown that developed cells have a reduced number of bound cAMP for a chc knock-out and that the down regulation of cAMP receptors is affected [45]. This shows that in the developed state, clathrin is involved in the function and regulation of cAMP receptors, whereby comparable mechanisms can also occur in the vegetative state. The ratio of detected carA foci with increased LimE activity and LimE foci is 40%.
The carA foci, with colocalized LimE focus, shows a similar distribution to the LimE foci difference map. However, a decreased number of carA foci with a colocalized LimE focus is detected compared to the number of LimE foci. Furthermore, the carA foci with colocalized LimE focus show a higher focus area with 0.71 x$10^{-12}$m$^2$ compared to LimE foci with 0.36 x$10^{-12}$m$^2$. It is possible that not all membrane intensity increases are detected by the foci routine, which are colocalized with a LimE focus. It can therefore be said that although a lower number of carA foci was found, the extension of the carA foci exceeds the extension of the LimE foci.
In addition to the carA foci which could be clearly assigned to a LimE foci, foci with a low intensity change to the surrounding area occurred which do not show increased LimE activity (Figure 4.13 (B)). These detected membrane foci show a height difference of 10 nm in carA direction between the maximum and minimum of the difference foci-neighbour height distribution (Figure 4.17 (A)). The maximum of the difference distribution is 39.9x$10^{-9}$ m and is therefore the maximum closest to the substrate compared to the other foci groups. Furthermore, the average focus to neighbour height difference map shows (Figure 4.20 (C)) that for the majority of detected foci the membrane and LimE activity is closer to the substrate than its surroundings.

### 5.2.3. Foci Detection Routine and Kernel Density Estimation

Due to the recording time of a MIET image, in combination with the adjustment of the image frame, the time difference between the images ranges from 20 s up to 2 min. Thus tracking of an focus throughout images is not possible. The MIET image recording time could influence the focus extent. As already mentioned in the Methods part, a shift is possible between the first and last pixel of the detected cell due to the acquisition time and the cell movement for longer recording times. As the lifetime of an actin focus is on average 13.5 s for AX2 [39], blurring of a focus is possible with an increased recording time.
An increase in time resolution would result in decreased intensity and thus z-range

resolution. Increasing the pixel size would result in fewer pixel per image and thus a shorter recording time but would also decrease x/y-resolution. A method was proposed, which enables the detection of dynamic process on the basis of MIET microscopy, which is called dynaMIET [92]. Provided by the fact that foci tracking would be possible, this method would enable observation of individual focus dynamics and could give a further insight into different label behaviours for actin foci.
The MIET measurements are performed on a gold coated substrate. To determine possible influences of the MIET substrate on the adhesion behavior of the cell, it might be useful to perform SCFS experiments to investigate influences on the adhesion parameters.

### Influences and uncertainties of the neighbours distribution

Due to the missing temporal resolution it is not possible to assign for example an occurring clathrin foci to a specific actin foci, instead MIET provides a momentary image of the intensity profile of the fluorescence receptors and their corresponding height matrices. Therefore a focus detection was implemented purely depended on the intensity matrix of one label, neglecting the second label. The same cells are evaluated to detect foci points of different label, thus an intersection of detected foci counted in both groups is possible between the foci group of LimE & clc foci and the group of clc & LimE foci. However, while two foci detected with different label can overlap in parts of the detected foci area, this does not necessarily mean, that these points correlate in their spatial focus appearance. This would mean, that pixel in the neighbours distribution can contain pixel of a focus, which in the second label is not fully covered by the focus extent. This for example is visible in the neighbours distribution of C.14 (B) and C.12 (B). Both show a larger value range of the distribution, which is not shown in C.13 (B) and C.11 (B). Furthermore, since it cannot be assumed that, for example, the extension of a focus correlates with the extension of an adhesion cluster, it may happen that the focus adjacent area contains activities that are attributed to the cluster. These example show that the neighbours distribution is possibly containing pixel belonging to the foci which thus biases the map. Additionally the height maps contain foci from different time points of the foci formation. In order to be able to make statements about the differences between the two distributions despite the influences and uncertainties of the neighbours distribution, the difference between the two maps is calculated. This makes it possible to detect areas that only exist in the respective map, while areas that are present in both maps cancel each other out.

### Foci Detection Routine

The size of the different foci groups was determined. The size of the clc foci is of particular interest, since this groupe represent the clathrin coat, whereby possible influences of an actin activity and beginning endocytosis can be neglected.

Assuming a circular focus, the focus diameter is calculated for the median of the focus area, resulting in a diameter of 760 nm. The size of the clathrin plaques in mammalian cells has been described with up to several hundred nanometers [84] and is therefore in a comparable range as the clathrin foci described here. High resolution microscopy methods enabled the detection of nascent integrin adhesion clusters with a size of about 100 nm and containing about 50 integrins [93]. The detection of the focus area is on one hand biased by the spatial resolution of the microscopy method, especially as the example for nascent integrin adhesion cluster shows that comparable structures might exist in the sub diffraction limit regime, bellow 250 nm. On the other hand, the size of the focus area is also biased by the foci detection routine and the applied threshold for the focus extent.
The individual label show differences in their appearance, thus making it necessary to adjust the detection routine parameters of the focus detection. The carA label for example shows a low intensity background which enables the detection of less pronounced foci. Thus the prominence value is reduced to detect and enable the selection of less prominent foci. For a low intensity focus, a wrong choice of parameters would mean that a too low prominence factor could blur the line between focus and background, while a too high chosen factor could cut of areas of the focus. This example illustrate the compromises made width the parameter selection and explains the necessity of label dependent parameter adjustments. This can be seen for example in the agreement of the median, for the LimE foci with increased clc intensity with 0.67 x$10^{-12}$m$^2$ and clc foci with increased LimE intensity with 0.62 x$10^{-12}$m$^2$. Interestingly, both groups cover a comparable section of the actin/clathrin foci process and probably a large part of the detected foci is present in both groups. Thus for parts of the group, the focus extension of the same foci were determined by different labels.
The clathrin light chain label shows a large variability in the detected foci sizes, ranging up to foci areas of comparable size to detected carA foci with no increase in LimE activity (Figure 4.15). However only a few of these large areas where detected while they appear as outliers and far outliers for the clc foci distribution. These differences in the size of the detected clc foci, can be due to different foci appearances ranging from large areas of increased clc activity to small clathrin punctea but also can be influenced by different background intensities of the clc label. While cells showing a nearly uniform distributed intensity where sorted out, also a high pre-selection threshold was chosen to detect only the prominent intensity maxima. The prominence factor was adapted for the foci of the entire image depending on the background intensity. The adjustment of the foci detection parameters could be avoided by the already described classification into background dependent groups for the clc label.

### Kernel Density Estimation

The kernel density estimation as a continues estimation for the PDF neglects possible uncertainties of the underlying data but instead assigns each data point a kernel

whose constant bandwidth accounts for the uncertainty and thus the bandwidth estimation is purely data driven. If the measurement error were chosen for the Gaussian kernel width in the case of MIET and the intensity dependent error magnitude, this would lead on one hand to cells with high intensity being counted more strongly (the way it is desired). But this would also mean that if the height distributions range is determined, the range would increase due to the error-dependent bandwidth adjustment of images with lower intensity and thus would strongly bias the range values. For a possible but unknown dependence between the height of the pixel and its intensity it would mean, that one group is more weighted and thus shifts the maximum probability density towards this direction.

## 5.3. Summary with Timeline of Active Intensity Regions

This work shows that despite the lack of temporal resolution a temporal subdivision was possible, based on focus formation and its time-dependent colocalisation with a second label, which can be attributed to different stages of the process. However, due to the lack of temporal resolution, only a rough temporal classification was possible, so that foci which can be assigned to an interval were grouped and as such the group is a superposition of the continuous focus process at different time steps. This subdivision in combination with different dual labels, allows the observation of the actin foci under different label backgrounds and thus shows different aspects of the foci process. The obtained results were summarized in the schematic drawing (Figure 5.3), beginning with a height change of the clathrin coat towards the substrate, followed by an actin height change. Member of WASp family colocalize with clathrin patches and induce their disappearance, while Arp2/3 proteins colocalize to over 90% with actin foci [52, 59]. WASp could be recruited to regulate the actin polarization and branching towards the membrane. Furthermore, it was found that *D.d.* major adhesion protein SadA and Talin A also colocalize to actin foci with over 90% spatially and temporally [39]. Thus a cluster of adhesion proteins assembles in the area of the clc foci and it is possible that clathrin act as a coat to stabilize the cluster. Further, height differences of the membrane label up to 140 nm appear at the focus regions compared to the neighbouring region, which could be explained by the pit formation of a CME at the position of an actin foci. Thus it might be possible that adhesion cluster formations at the actin foci are regulated and dissolved by clathrin structures. The detection of carA foci colocalizing with actin foci indicates that actin foci could serve as signaling platforms and that the carA foci are engulfed by CME. The clathrin structures of *D.d.* cells described in this work show similarities to clathrin plaques of mammalian cells, that occur as adhesion cluster independently of focal adhesion points and serve as signaling platforms [21].
A knock-out of the clc allows to investigate the impact of a not fully functional clathrin apparatus on the cell behaviour and especially the cell adhesion. While

the combination of MIET microscopy with SCFS allows to examine the knock-out from different perspectives due to these applied methods. The knock-out shows for SCFS experiments a strongly reduced number of steps and deficiencies in the step force. The examination of the MIET-based height maps revealed that cells without clc show an actin activity closer to the substrate compared to wild-type cells. Furthermore, a doubling of the actin foci was observed. The results of SCFS experiments impressively show that clathrin plays a significant roll in the adhesion of *D.d.* cells, while the MIET results indicates a possible compensation of the not fully functional clathrin structure by the actin cortex. The applied methods show different aspects of the adhesion mechanism, which allows to get a more complete picture of the underlying process.
In conclusion, it can be said, that clathrin has a wide range of applications and that possibly in comparison with mammalian cells a less developed adhesion mechanism is established for *D.d.* based on clathrin structures.

### 5.3.1. Timeline and Outlook

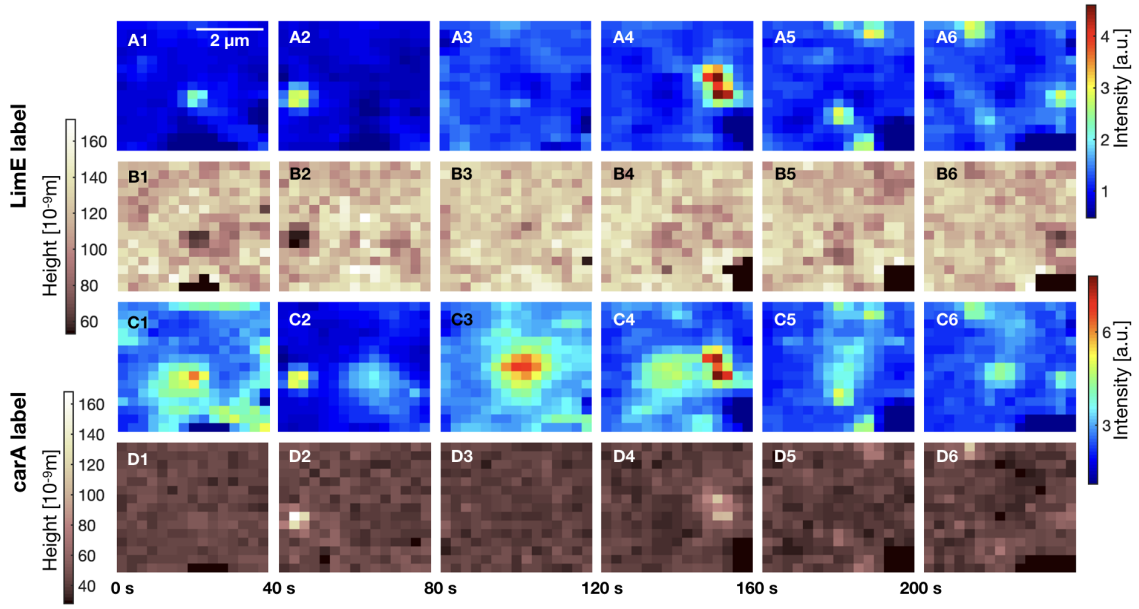


Figure 5.5.: Timline of an region with increased foci activity. For the LimE intensity matrix in (A), the corresponding height matrix in (B), the carA intensity image in (C) and its corresponding height image in (D). The numbers behind the letter refer to the image number. The time value on the bottom are estimated due to the absence of the recorded time.

In spite of the large time intervals between images compared to the lifetime of an actin foci, it is possible to show areas with a variety of activities, which is shown in a Timline for the LimE and carA label combination in Figure 5.5 and for the LimE

and clc label combination in Figure 5.6. It is noticeable that the actin foci shown here are clearly identifiable and thus the detection is not affected by adjacent foci, as for example visible in A1, A2, A4, A5 for Figure 5.5 or A3, A4, A5 in Figure 5.6. However the case is not so unambiguous for the second label. For example, while for the carA label in image C2, two independent foci can be detected one of which correlates with a LimE label focus and shows the characteristics described above, while a separation is more difficult for C4. At the position of the actin foci, visible in A4, also a carA foci is visible and the membrane shows an increase to its neighbours (D4). The neighboring carA intensity increase in C4 is spatially inseparable from the carA foci and shows characteristics attributed to the carA foci group without LimE activity, such as actin (B4) and membrane (D4) activity closer to the substrate compared to its surroundings.
For further analysis a combined foci analysis might be useful. So far, each label was considered independently for the focus detection, whereas colocalization was defined based on an average intensity increase in the focus area compared to the focus adjacent area. In a combined foci analysis, two foci detected in different label overlapping in parts of the detected foci areas, would be considered together. This would lead to an enlarged focus area and thus contain points which are not assigned to the respective intensity focus. However, the combined analysis would cover the entire activity range of the combined focus area. This would make it possible to analyze whether a focus occurs independently or whether the focus is part of a larger area of activity in the second label, which can be seen for example in C1, C3, C4 of the carA label in Figure 5.5. The same tendency also applies to the timeline which is shown in Figure 5.6, while actin shows distinctly detectable foci, the clc label in this example shows a two-dimensional activity over the entire time series. The combined analysis would also minimize possible errors of overlapping foci by the detection of the adjacent pixel and thus reduce the bias of the neighbours distribution. Further, this would enable a segmentation of pixel showing a focus in one of the respective label to pixel showing an activity in both label and thus a separation of the activity groups in the combined focus area.
However, due to the rough temporal resolution it can only be assumed that, for example the membrane intensity focus nucleates in C2, persists in C3 and leads to the combined detection of an carA focus with adjacent actin focus shown in C4 and that these are not simply independent events. The same applies to the clc label, where it can only be assumed that the clathrin focus shown in Figure 5.6 C1-C5 is counted as one event and not as 5 independet foci. An increase time resolution could link these detected foci and prove the continuous appearence of the clc structure as long lasting structures. It would also make it possible to examine the carA foci lifetime and thus might give further evidence that the carA foci show a comparable behaviour to clc foci and that both foci groups possibly even colocalize. Nevertheless, the timeline shows that large carA and clc foci are present in the image section shown and that LimE foci regularly occur in their vicinity.

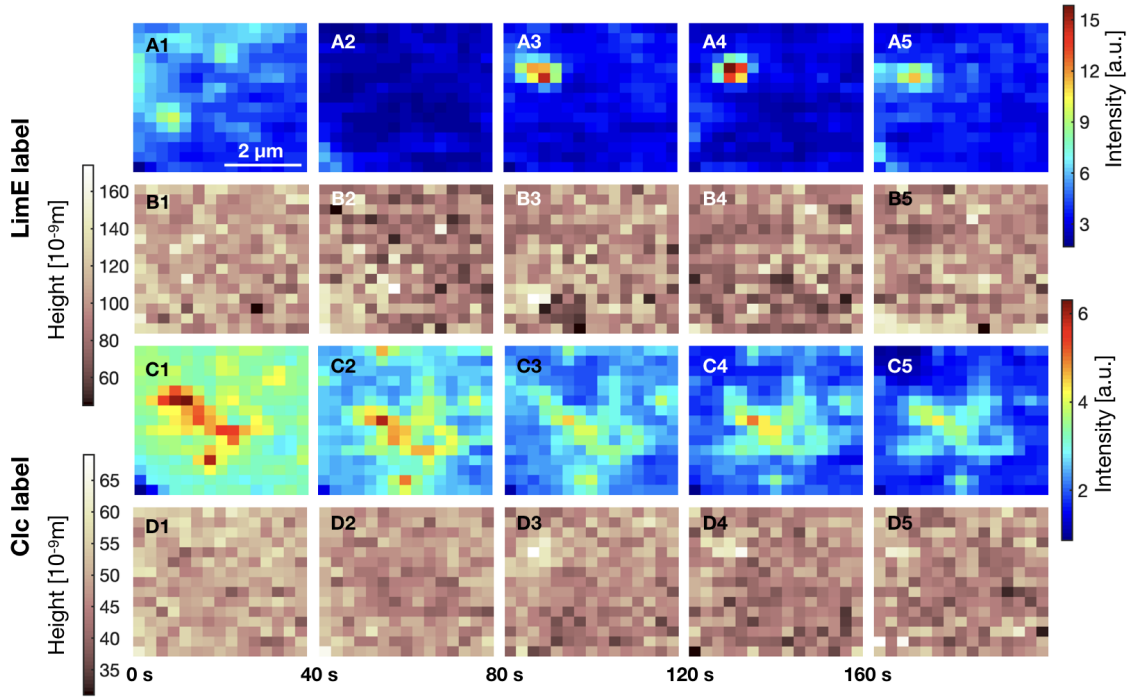


Figure 5.6.: Timline of an region with increased foci activity. For the LimE intensity matrix in (A), the corresponding height matrix in (B), the clc intensity image in (C) and its corresponding height image in (D). The numbers behind the letter refer to the image number. The time value on the bottom are estimated due to the absence of the recorded time.

# A. Statistical Analysis Methods

A short overview is given at this section about the applied analysis methods. The first part of this section, deals with the *IGOR PRO* implemented test routine for choice of the applied significance test, while the second part gives an overview about box plots and 1D and 2D kernel density estimation as applied presentation methods. The *IGOR PRO* version used in this thesis is 8.03 (Build 33570), the *MATLAB* version used is *R*2018*a*.

## A.1. Moments of Probability Density Function

For the test procedures to chose the required significance test, moments of a probability density function (PDF) are used to estimate the underlying distribution of the extracted parameters. In general, the n-th central moment $\mu^n$ of a random variable X and its mean value $\mu$ are given by

$$\mu^n = E[(X - E[X])^n] = \int_{-\infty}^{\infty} (x-\mu)^n f(x) dx \qquad \text{and} \tag{A.1}$$

$$\mu^1 = E[X] = \int_{-\infty}^{\infty} x f(x) dx, \tag{A.2}$$

of a continuous probability distribution with the PDF $f(x)$ and expectation value $E(X)$ of the random variable $X$. Based on this formula the four moments, mean $\mu^1$, variance $\mu^2$ and the third and fourth moment $\mu^3$ and $\mu^4$ used to define skewness and kurtosis can be derived. All of these are used in this work.
However, the parameters obtained from $N$ measurements can be seen as values $(x_0, x_1, ..., x_{N-1})$ of an unknown distribution. The moments calculated of this sample, drawn from an unknown distribution are only an estimation of the moments of the underlying distribution. The mean $\bar{x}$, variance $\sigma^2_{\bar{x}}$, skewness $sk_{\bar{x}}$ and kurtosis $ku_{\bar{x}}$ of

a data sample are given by [94]

$$\bar{x} = \frac{1}{N}\sum_{i=0}^{N-1} x_i \tag{A.3}$$

$$\sigma_{\bar{x}}^2 = \frac{1}{N-1}\sum_{i=0}^{N-1}(x_i - \bar{x}) \tag{A.4}$$

$$sk_{\bar{x}} = \frac{1}{N}\sum_{i=0}^{N-1}\left(\frac{x_i - \bar{x}}{\sigma_{\bar{x}}}\right)^3 \tag{A.5}$$

$$ku_{\bar{x}} = \left[\frac{1}{N}\sum_{i=0}^{N-1}\left(\frac{x_i - \bar{x}}{\sigma_{\bar{x}}}\right)^4\right] - 3. \tag{A.6}$$

The skewness defines the asymmetry of the distribution. Even a symmetric distribution can lead to a non-zero result for $sk_{\bar{x}}$, where the sign defines the direction of asymmetry [94]. The kurtosis describes the distributions shape, as peaked with $ku_{\bar{x}} > 0$, or flattened with $ku_{\bar{x}} < 0$. The subtraction with three in Formula A.6 sets the kurtosis of a normal distribution to zero. To distinct the results from a normal distribution a threshold needs to be defined. Therefore a critical value is calculated by the test procedure, usually depending on the sample size, to decide whether a skewness or kurtosis is given.

## A.2. Test for Normal Distribution

The *Jarque -Bera* ($JB$) *Test* is designed to to test normality of a distribution and is defined as

$$JB = \frac{N}{6}\left(sk_{\bar{x}}^2 + \frac{ku_{\bar{x}}^2}{4}\right). \tag{A.7}$$

If the skewness or kurtosis of the tested sample corresponds to that of a normal distribution the $JB$ value is close to zero.
Another test performed for this thesis is the *Kolmogorov -Smirnov* ($KS$) *Test*. Therefore the cumulative distribution function (CDF) of the sample $S_N(x)$ is calculated, which is defined as the probability that a random variable $X$, drawn from the underlying distribution is $X \leq x$ with the boundary condition $S_N(-\infty) = 0$ and $S_N(\infty) = 1$. The $KS$ test is then defined as the maximal distance $d_{KS}$ from $S_N(x)$ to the CDF of the distribution $P(x)$ [94] with

$$d_{KS} = \max_{-\infty<x<\infty}[S_N(x) - P(x)]. \tag{A.8}$$

In *IGOR Pro*, the *KS Test* is used to compare the calculated $S_N(x)$ with the CDF of a normal distribution ($P(x)$) with the estimated mean and variance parameters of the sample.

In *IGOR Pro*, the result of a test is compared to a critical value to decide if the results fulfill the hypothesis of a normal distribution. The critical value is calculated from the given distribution and the significance level $\alpha$, which is by default set to $\alpha = 0.05$. The significance level defines the risk in the default case of 5%, of having a normal distribution while rejecting the hypothesis of a normal distribution. The calculation of the critical value and the decision of accepting or rejecting the hypothesis is implemented into the test operation in *IGOR Pro*. For more information, the reader is refereed to [95].

## A.3. Significance test

The significance tests used in this work, calculate the probability (*p-value*) of two samples from different populations, assuming the independence of both populations, to fulfill the null-hypothesis of having the same mean/median or show a shift between the distributions.
With the test procedure implemented in *IGOR Pro*, the input data sets can be tested for a normal distribution with the *JB* or *KS Test*, mentioned before. If fulfilling the requirements, the data sets are tested for equal variance to ensure that this assumption necessary for the *Two-Sample T Test* is justified.
The *T Test* sets the null-hypothesis of equal mean and calculates the $t$ value as difference between the mean of the data sets $\bar{x}_1, \bar{x}_2$ to be compared with

$$t = \frac{\bar{x}_1 - \bar{x}_2}{\sigma_t \sqrt{\frac{1}{N_1} + \frac{1}{N_2}}}, \tag{A.9}$$

with $\sigma_t$ the estimated standard deviation of the pooled set of data [94]. The *p-value* is antiproportional to the $t$, for small $t$ and *p-value*$> 0.1$, the hypothesis of a same mean is valid. With increasing $t$ value the *p-value* drops below certain significance level $\alpha = 0.1$, $0.05$, $0.01, 0.005$ indicated in the following by [*],[**],[***],[****].
If the necessary assumptions for a *T Test* are not fulfilled, the test procedure recommends the *Wilcoxon Rank-Sum* ($W$) *Test*. The *W Test* compares two independent data sets with $N_1, N_2$ points respectively to test the null-hypothesis in order to find out whether the median of both samples are the same. The idea of the test is to pool both data sets and rank the data points according to their measured value. The sum of the ranks from one sample is compared to the expected value for the mean rank sum of the pooled set with $E(X_{N_i}) = N_i \frac{N_1+N_2+1}{2}$ [96]. The *p-value* is antiproportional to the distance of the rank sum from the expected value. For a small distance and *p-value*$> 0.1$, the hypothesis of same median is valid, with increasing distances the *p-value* drops below the same significance level $\alpha = 0.1$, $0.05$, $0.01, 0.005$ indicated in the following by [*],[**],[***],[****].

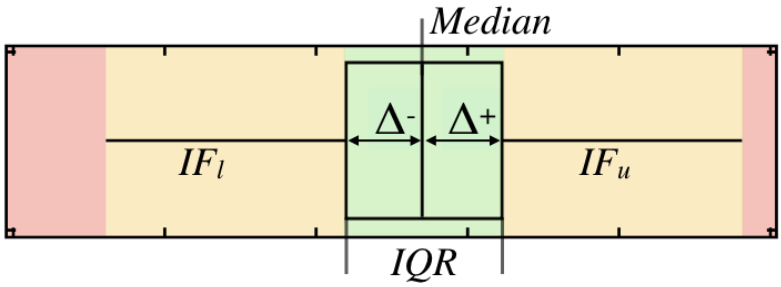


Figure A.1.: Sketch to symbolize the box plot parameters. The box contains 50% of the data points colored in green, with box width defined as $IQR$ and the upper and lower box as $\Delta^{+/-}$. The whiskers and yellow area show the inner fence $IF$. Points in the red area are considered outliers.

## A.4. Box Plots

One common routine to present the underlying distribution of the data by using box plots. The box contains 50% of the data points and is set between 25th percentile at the postion $Q_1$ and 75th percentile at the postion $Q_3$, with the 50th percentile of the data points and the postion $Q_2$ representing the median of the distribution, as shown in Figure A.1. The width of the box is defined by the interquartile range $IQR = Q_3 - Q_1$. The width between median and 75% line is in the following referred to as $\Delta^+ = Q_3 - Q_2$ and the width to the 25% line as $\Delta^- = Q_2 - Q_1$. A point $x$ is considered as outlier if it exceeds the inner fence $IF$ which is defined as $IF_l = Q_1 - 1.5 \cdot IQR$ as the lower inner fence and $IF_u = Q_3 + 1.5 \cdot IQR$ as the upper inner fence. The $IF$ is shown as whisker on the box. Points are considered as far outliers if they exceed the outer fence $OF$, which is defined as $OF_l = Q_1 - 3 \cdot IQR$ as the lower outer fence and $OF_u = Q_3 + 3 \cdot IQR$ as the upper outer fence. These points are highlighted in the plot.

## A.5. Kernel Density Estimation (KDE)

While a box plot is assuming a monomodal distribution and is not covering a possible multimodal distribution, the kernel density estimation ($KDE$) is chosen providing a continuous estimation of the data portrayed in a histogram. Each of the $n$ drawn data points $x$ of the unknown distribution is assumed to span a kernel with the bandwidth $h_{ba}$ as width of the kernel. The resulting PDF is given by the sum over the individual kernels. The kernel used for this thesis has a Gaussian shape, which

can be defined as follows in the 1-dimensional case [97, 98]

$$KDE(y, h_{ba}) = \frac{1}{n} \sum_{i=1}^{n} K\left(\frac{y - x_i}{h_{ba}}\right) \tag{A.10}$$

$$K(y, x_i, h_{ba}) = \frac{1}{\sqrt{2\pi h_{ba}}} \exp -\frac{1}{2}\left(\frac{y - x_i}{h_{ba}}\right)^2. \tag{A.11}$$

The bandwidth is selected by the *MATLAB* program *kde* [99], which detects the bandwidth purely data-driven [98]. With the optimal bandwidth the PDF is evaluated with the *fitdist* function for a given data set on a vector spanning the region of interest, with $y$ as an elements of this vector.
In the 2-dimensional case, the Gaussian kernel shape can be described by

$$K(\overrightarrow{y}, \overrightarrow{x_i}, \mathbf{h}_{ba}) = \frac{1}{2\pi\sqrt{h_{ba_{1,1}} h_{ba_{2,2}}}} \exp\left(-\frac{1}{2}\left(\frac{y_1 - x_{i_1}}{h_{ba_{1,1}}}\right)^2 - \frac{1}{2}\left(\frac{y_2 - x_{i_2}}{h_{ba_{2,2}}}\right)^2\right), \tag{A.12}$$

with $h_{ba_{1,1/2,2}}$ the non-zero elements of the diagonal bandwidth matrix $\mathbf{h}_{ba}$ [98], the $n$ drawn bivariate data points $\overrightarrow{x_i}$ and the matrix spanning the region of interest, with its elements $\overrightarrow{y}$. The bandwidth matrix elements are selected and the PDF is evaluated with the *MATLAB* program *kde2d* [100].

# B. Single Cell Force Spectroscopy (SCFS)

| | | WT NC4A2 | NC4A2 clc- |
|---|---|---|---|
| $F_{Max}$ | Median | 1.39 x $10^{-9}$ N | 1.14 x $10^{-9}$ N |
| | $p-value$ | 0.0042 ($W$ *Test*) | |
| | $\Delta^{+}_{F_{Max}}$ | 0.78 x $10^{-9}$ N | 0.76 x $10^{-9}$ N |
| | $\Delta^{-}_{F_{Max}}$ | 0.54 x $10^{-9}$ N | 0.52 x $10^{-9}$ N |
| | # points | 210 | 258 |
| $W_{Adh}$ | Median | 0.42 x $10^{-15}$ J | 0.22 x $10^{-15}$ J |
| | $p-value$ | 1.2 x $10^{-6}$ ($W$ *Test*) | |
| | $\Delta^{+}_{W_{Adh}}$ | 0.87 x $10^{-15}$ J | 0.44 x $10^{-15}$ J |
| | $\Delta^{-}_{W_{Adh}}$ | 0.25 x $10^{-15}$ J | 0.12 x $10^{-15}$ J |
| | # points | 210 | 258 |
| Cell Diameter | Median | 12.6 x $10^{-6}$ m | 13.9 x $10^{-6}$ m |
| | $p-value$ | 0 ($W$ *Test*) | |
| | $\Delta^{+}_{\text{Cell Diameter}}$ | 1.0 x $10^{-6}$ m | 1.7 x $10^{-6}$ m |
| | $\Delta^{-}_{\text{Cell Diameter}}$ | 1.1 x $10^{-6}$ m | 1.2 x $10^{-6}$ m |
| | # points | 109 | 74 |

Table B.1.: Results for the maximum adhesion force (top row), adhesion work (middle row) and cell diameter (bottom row). Result values shown are the median, $p-value$ and the test performed ($W$ *Test* referes to *Wilcoxon Rank-Sum Test* and $T$ *Test* to *Two-Sample T Test*), the box width for the upper and lower box and the number of data points.

| Cell Diameter | WT NC4A2 | NC4A2 clc- |
|---|---|---|
| Mean | $(12.6 \pm 2.6)$ x $10^{-6}$ m | $(14.2 \pm 2.3)$ x $10^{-6}$ m |
| Standard Deviation | 1.6 x $10^{-6}$ m | 2.0 x $10^{-6}$ m |
| $sk_{\bar{x}}$ | 0.09 (0.23) | 0.52 (0.28) |
| $ku_{\bar{x}}$ | $-0.45$ (0.47) | $-0.21$ (0.57) |
| $JB$ | 1.07 (5.19) | 3.47 (4.86) |
| # points | 109 | 74 |

Table B.2.: Results for the mean with the calculated error and the standard deviation for the cell diameter. The skewness, kurtosis and the results from the *Jarque -Bera Test* are listed for the cell diameter, because the normal distribution hypothesis is not rejected. The values in brackets refer to the standard error as an suggested estimator for skewness and kurtosis, as shown in section A.1. The brackets behind the $JB$ value show the critical value calculated by *IGOR Pro* after which the normal distribution hypothesis is rejected.

| | | WT NC4A2 | NC4A2 clc- |
|---|---|---|---|
| $F_{Max}/A_{Con}$ | Median | 12.2 N/m$^2$ | 7.7 N/m$^2$ |
| | $p-value$ | 0.00006 ($W$ *Test*) | |
| | $\Delta^{+}_{F_{Max}/A_{Con}}$ | 9.4 N/m$^2$ | 6.9 N/m$^2$ |
| | $\Delta^{-}_{F_{Max}/A_{Con}}$ | 4.7 N/m$^2$ | 3.8 N/m$^2$ |
| | # points | 109 | 74 |
| $W_{Adh}/A_{Con}$ | Median | 0.42 x $10^{-5}$ J/m$^2$ | 0.19 x $10^{-5}$ J/m$^2$ |
| | $p-value$ | 0.0009 ($W$ *Test*) | |
| | $\Delta^{+}_{W_{Adh}/A_{Con}}$ | 0.48 x $10^{-5}$ J/m$^2$ | 0.21 x $10^{-5}$ J/m$^2$ |
| | $\Delta^{-}_{W_{Adh}/A_{Con}}$ | 0.26 x $10^{-5}$ J/m$^2$ | 0.11 x $10^{-5}$ J/m$^2$ |
| | # points | 109 | 74 |

Table B.3.: Results for the maximum adhesion force per area (top row) and adhesion work per area (bottom row). Result values shown are the median, $p-value$ and the test performed, the box width for the upper and lower box and the number of data points.

| | | WT NC4A2 | NC4A2 clc- |
|---|---|---|---|
| $F_{Step}$ | Median | 114.9 x $10^{-12}$ N | 109.3 x $10^{-12}$ N |
| | $p-value$ | 0.54 ($W$ *Test*) | |
| | $\Delta^{+}_{F_{Step}}$ | 33.7 x $10^{-12}$ N | 51 x $10^{-12}$ N |
| | $\Delta^{-}_{F_{Step}}$ | 22.0 x $10^{-12}$ N | 23.7 x $10^{-12}$ N |
| | #points | 268 | 90 |
| $l_{Step}$ | Median | 1.15 x $10^{-6}$ m | 0.65 x $10^{-6}$ m |
| | $p-value$ | 0.25 ($W$ *Test*) | |
| | $\Delta^{+}_{l_{Step}}$ | 1.34 x $10^{-6}$ m | 1.45 x $10^{-6}$ m |
| | $\Delta^{-}_{l_{Step}}$ | 0.71 x $10^{-6}$ m | 0.25 x $10^{-6}$ m |
| | #points | 176 | 50 |
| $F-Position_{Step}$ | Median | 196.1 x $10^{-12}$ N | 139.2 x $10^{-12}$ N |
| | $p-value$ | 0.029 ($W$ *Test*) | |
| | $\Delta^{+}_{F-Position_{Step}}$ | 254.4 x $10^{-12}$ N | 155.5 x $10^{-12}$ N |
| | $\Delta^{-}_{F-Position_{Step}}$ | 115.8 x $10^{-12}$ N | 65.8 x $10^{-12}$ N |
| | # points | 268 | 90 |
| $l-Position_{Step}$ | Median | 3.65 x $10^{-6}$ m | 3.01 x $10^{-6}$ m |
| | $p-value$ | 0.17 ($W$ *Test*) | |
| | $\Delta^{+}_{l-Position_{Step}}$ | 3.85 x $10^{-6}$ m | 2.05 x $10^{-6}$ m |
| | $\Delta^{-}_{l-Position_{Step}}$ | 1.77 x $10^{-6}$ m | 0.95 x $10^{-6}$ m |
| | # points | 268 | 90 |

Table B.4.: Results for the step force (top row), step length (upper middle row), step position in force direction (lower middle row) and step position in separation direction (bottom row). Result values shown are the median, $p-value$ and the test performed, the box width for the upper and lower box and the number of data points.

| | | WT NC4A2 | NC4A2 clc- |
|---|---|---|---|
| $l_{Pulling}$ | Median | 4.75 x $10^{-6}$ m | 3.60 x $10^{-6}$ m |
| | $p-value$ | 0.31 ($W$ *Test*) | |
| | $\Delta^{+}_{l_{Pulling}}$ | 6.89 x $10^{-6}$ m | 2.76 x $10^{-6}$ m |
| | $\Delta^{-}_{l_{Pulling}}$ | 2.75 x $10^{-6}$ m | 1.64 x $10^{-6}$ m |
| | # points | 92 | 40 |
| # Steps | Median | 2 | 2 |
| | $p-value$ | 0.173 ($W$ *Test*) | |
| | $\Delta^{+}_{\#Steps}$ | 1.75 | 0.75 |
| | $\Delta^{-}_{\#Steps}$ | 1 | 1 |
| | # points | 92 | 40 |

Table B.5.: Results for the pulling length (top row) and number of steps per curve (bottom row). Result values shown are the median, $p-value$ and the test performed, the box width for the upper and lower box and the number of data points.

| mean steps per cell | WT NC4A2 | NC4A2 clc- |
|---|---|---|
| Median | 0.61 | 0 |
| $p-value$ | 3 x $10^{-4}$ ($W$ *Test*) | |
| $\Delta^{+}_{\text{mean steps per cell}}$ | 1.52 | 0.52 |
| $\Delta^{-}_{\text{mean steps per cell}}$ | 0.56 | 0 |
| # points | 52 | 40 |

Table B.6.: Results for the mean number of steps per cell. Result values shown are the median, $p-value$ and the test performed, the box width for the upper and lower box and the number of data points.

# C. Metal Induced Energy Transfer (MIET)

## C.1. Detection of Cell Contour and Cytosol

Based on the requirements to exclude actin activity at pseudopodia and the increase in height at the cell periphery, a *MATLAB* script is used to delete background noises, detect an outline of the contact area and define the extend of the cell contour and the cytosolic area for the actin intensity signal. Which serve as template for the additional fluorescence channel and height maps. This processing cascade is illustrated for the actin intensity signal in Figure C.1.
To detect the outline of the contact area a threshold is defined at 5% of the maximum intensity value. A binarisation transforms all matrix elements larger than the threshold into a 2D binary matrix with the *imbinarize* function. Possible holes in the binary matrix, e.g. originated due to the missing actin activity in vacuoles, are closed by *imfill*. Furthermore, there is the possibility of another cell at the edges of a matrix section. These cell remnants are deleted by removing all connected objects that are smaller than half of the sum of non zero elements with the *bwareaopen* function. This ensures that only the largest connected object is selected, provided that an image section was chosen that covers only one cell. The resulting binary matrix of the cell is shown in Figure C.1 (A).
In order to detect the area of possible pseudopodia formations, the *regionprobs* function determines the cell center of mass and the axis parameter of an ellipse corresponding to the cell periphery. The minor axis length provides an initial value for a circle diameter to crop the cell center. This circle diameter is reduced until the cell covers 90% of the circle area. The resulting cell segments are shown for the cell center in Figure C.1 (B) and the area containing possible pseudopodia formations in C.1 (C).
The function *bwboundaries* detects the contact area outline in the binary matrix, which is shown in Figure C.1 (A) and (D). To determine the extent of the cell contour, the cell outline is removed from the matrix (cytosol matrix) and converted into an equally dimensioned zero matrix, which is in the following referred to as contour matrix. The outline of the narrowed contact area is detected again for further processing. The lower expansion limit of the cell contour is three pixels in width for both segments, in order to avoid the aforementioned change in height on the contour of the contact area. In order to count the high actin activity in a pseudopodium to the contour matrix, the area between the lower expansion limit

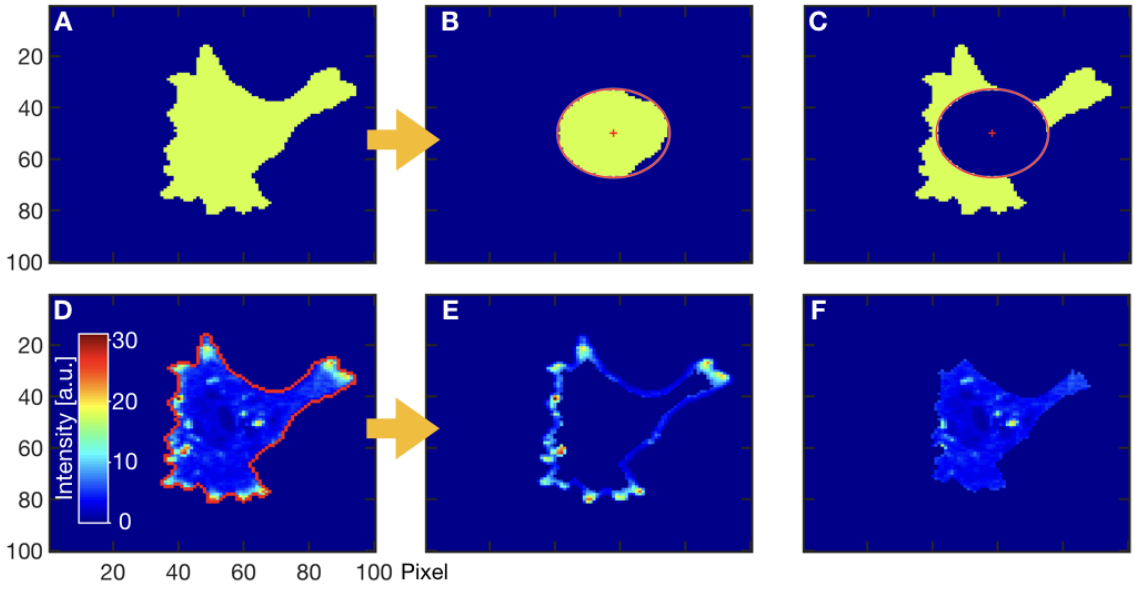


Figure C.1.: The micrographs in the top row show the processing cascade of the actin intensity matrix converted to a binary matrix with background noise removed by a cell threshold. The rows and columns of the graphs define the position in pixels, the corresponding element is one at the cells position and zero at the backgrounds. (A) Shows an exemplary cell with high pseudopodia activity. Based on the binary matrix, the center of mass is detected (B,red marker) and the circle covering the cell center (B,red circle). The red circle segments the binary matrix into a cell center domain (B) and outlier formations showing possible random pseudopodia (C). The bottom row show the processing cascade of the corresponding actin intensity matrix. The rows and columns define the position in pixel, the corresponding element defines the intensity value. (D) shows the intensity signal and the detected cell contour boundary in red. Based on the detected boundary the cell contour is defined and extracted with extended scope in the area indicated in (C), the resulting contour is shown in (E). The remaining cytosol (F) is extracted as difference between the narrowed cell (red boundary) from (D) and its contour in (E).

and a variable upper limit is incrementally analyzed for the area shown in Figure C.1 (C). Pixels are added from the respective outline of the contact area to the contour that have a higher intensity than the average contour intensity. The upper limit is manually adjusted to cover possible pseudopodia and is by default set to seven pixels in width. The resulting cell contour and cytosol are shown in C.1 (E) and (F). By detecting the contour separately for both regions, the contour should cover high actin activity at pseudopodia accurate and reduce the contour extent at the contour close to the cell center.

## C.2. Detection of Vacuoles

A *MATLAB* script detects vacuoles in the actin intensity matrix and generates a binary image of the vacuole regions as template to remove these regions in the intensity and height matrices. The processing cascade is shown in Figure C.2. To

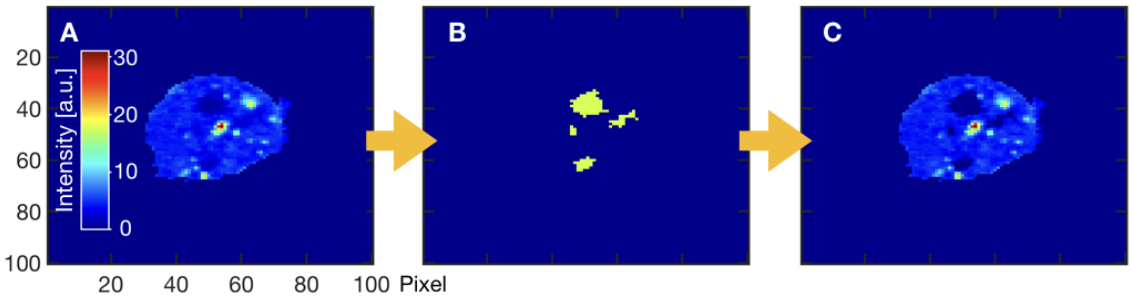


Figure C.2.: The micrographs show the processing cascade to detect vacuoles in the actin intensity matrix. The rows and columns of the graphs define the position in pixel, the corresponding element defines the intensity value. (A) shows an exemplary cell with removed cell contour and pronounced vacuoles, visible as areas of low intensity in the cytosol. The routine detects the vacuoles in the intensity image and returns a binary image with the vacuole positions, as shown in (B), which is used as template to remove the vacuoles from the original matrix, as shown in (C).

detect vacuoles, values higher than a threshold value are removed from the actin intensity matrix and converted with the *imbinarize* function into a binarized matrix. The threshold is defined as half the intensity between the minimum and the average cytosolic actin intensity. Afterwards possible holes are filled (*imfill*) and isolated pixels removed (*bwareaopen*). The user can manually change the threshold until all vacuoles are covered by the code.
The resulting matrices contain only the cytosolic contact area, with removed contour and vacuoles. For determination of the height distribution of the respective fluorescence label, the non-zero matrix elements are saved as a list for each matrix. Based on the axial resolution fit shown in Figure 3.7 (A), the height error is calculated for each element with the pixel intensity.

## C.3. Cell Height

| contact Area | LimE & carA label | LimE & clc label | LimE label & clc- |
|---|---|---|---|
| Median | 121.8 x $10^{-12}$ $m^2$ | 146.7 x $10^{-12}$ $m^2$ | 124.5 x $10^{-12}$ $m^2$ |
| $\Delta^{+}_{contactArea}$ | 27.7 x $10^{-12}$ $m^2$ | 36.3 x $10^{-12}$ $m^2$ | 49.7 x $10^{-12}$ $m^2$ |
| $\Delta^{-}_{contactArea}$ | 35.1 x $10^{-12}$ $m^2$ | 22 x $10^{-12}$ $m^2$ | 12.8 x $10^{-12}$ $m^2$ |
| # points | 108 | 112 | 73 |
| $p_{1,2} - value$ | | 0 | (*W Test*) |
| $p_{1,3} - value$ | | 0.011 | (*W Test*) |
| $p_{2,3} - value$ | | 0.004 | (*W Test*) |

Table C.1.: Results for the contact Area. Result values shown are the median, the box width for the upper and lower box, the number of data points, the $p - value$ and the test performed (*W Test* referes to *Wilcoxon Rank-Sum Test* and *T Test* to *Two-Sample T Test*). The indices refer to the compared coloumns.

| Height weighted Mean | carA label | clc label |
|---|---|---|
| Median | 52.9 x $10^{-9}$ m | 45.5 x $10^{-9}$ m |
| $\Delta^{+}_{weightedMean}$ | 3.2 x $10^{-9}$ m | 2.2 x $10^{-9}$ m |
| $\Delta^{-}_{weightedMean}$ | 4.4 x $10^{-9}$ m | 1.0 x $10^{-9}$ m |
| # points | 106 | 112 |

Table C.2.: Results for the error weighted mean heights of the cytosol with removed contour and vacuole area. Result values shown are the median, the box width for the upper and lower box and the number of data points.

| Height weighted Mean | LimE label (carA) | LimE label (clc) | LimE label (clc-) |
|---|---|---|---|
| Median | 86.1 x $10^{-9}$ m | 81.7 x $10^{-9}$ m | 78.2 x $10^{-9}$ m |
| $\Delta^{+}_{weightedMean}$ | 4.6 x $10^{-9}$ m | 14.2 x $10^{-9}$ m | 7.7 x $10^{-9}$ m |
| $\Delta^{-}_{weightedMean}$ | 1.9 x $10^{-9}$ m | 7.1 x $10^{-9}$ m | 3.2 x $10^{-9}$ m |
| # points | 108 | 112 | 73 |
| $p_{1,2} - value$ | | 0.012 | $(W\ Test)$ |
| $p_{1,3} - value$ | | 0.02 | $(W\ Test)$ |
| $p_{2,3} - value$ | | 0 | $(W\ Test)$ |

Table C.3.: Results for the error weighted mean heights of the cytosol with removed contour and vacuole area. Result values shown are the median, the box width for the upper and lower box, the number of data points, the $p - value$ and the test performed. The indices refer to the compared coloumns.

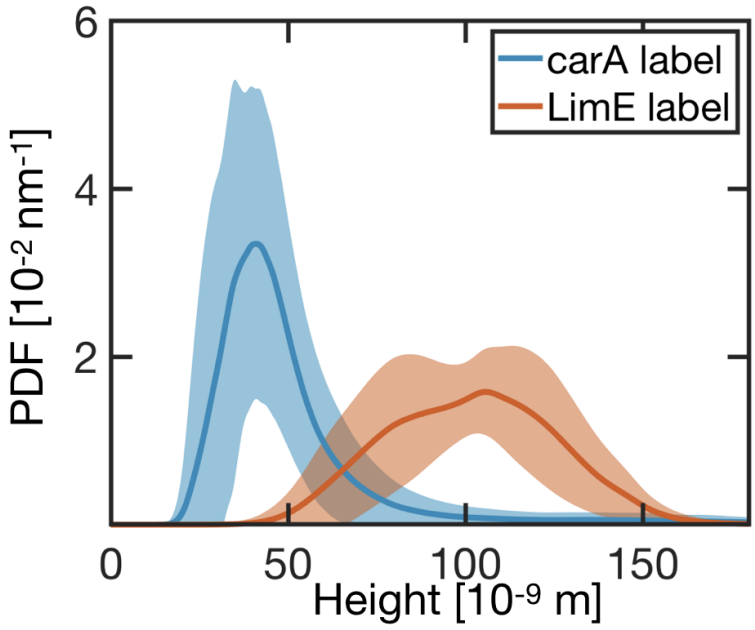


Figure C.3.: Average PDF of height maps from the carA and LimE dual fluorescence label are shown as a straight lines. The same colored area around the PDF line indicates the standard deviation.

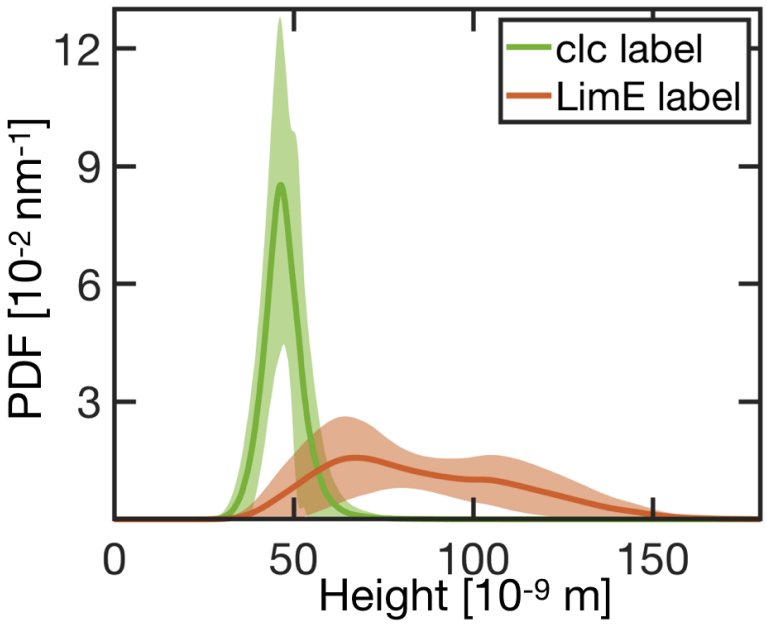


Figure C.4.: Average PDF of height maps from the clc and LimE dual fluorescence label are shown as a straight lines. The same colored area around the PDF line indicates the standard deviation.

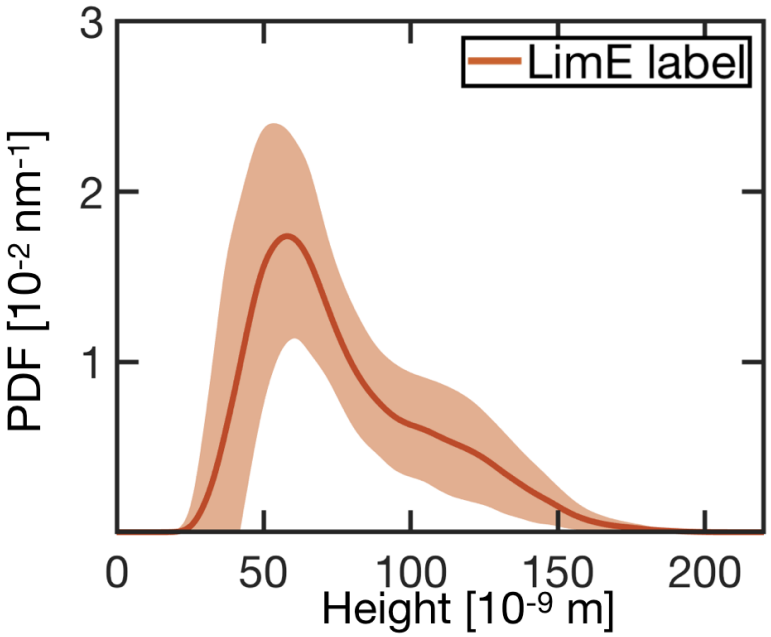


Figure C.5.: Average PDF of height maps from the LimE fluorescence label with clc knock-out, is shown as a straight line. The same colored area around the PDF line indicates the standard deviation.

| Height | carA label | clc label |
|---|---|---|
| Modulus | 41.0 x $10^{-9}$ m | 46.5 x $10^{-9}$ m |
| $\sigma^{+}_{Modulus}$ | 10.2 x $10^{-9}$ m | 5.2 x $10^{-9}$ m |
| $\sigma^{-}_{Modulus}$ | 14.5 x $10^{-9}$ m | 3.6 x $10^{-9}$ m |
| $Q_{25}$ | 36.4 x $10^{-9}$ m | 43.6 x $10^{-9}$ m |
| $\sigma^{\pm}_{Q_{25}}$ | 10.8 x $10^{-9}$ m | 2.2 x $10^{-9}$ m |
| $Q_{75}$ | 54.2 x $10^{-9}$ m | 50.3 x $10^{-9}$ m |
| $\sigma^{\pm}_{Q_{75}}$ | 7.4 x $10^{-9}$ m | 3.0 x $10^{-9}$ m |
| # PDF curves | 106 | 112 |

Table C.4.: Part 1 of the results: for the modulus and the 25% and 75% Quartile of the average PDF of height maps from different fluorescence label. The $\sigma^{+/-}_{Modulus}$-values refer to the distance to the boundary of the standard deviation area in the positive or negative height direction, the $\sigma^{\pm}_{Q}$-values refer to the distance to the boundary of the standard deviation area in the positive height direction for 75% Quartile and in negative height direction for 25% Quartile.

| Height | LimE label (carA) | LimE label (clc) | LimE label (clc-) |
|---|---|---|---|
| Modulus | 105.7 x $10^{-9}$ m | 67.0 x $10^{-9}$ m | 58.0 x $10^{-9}$ m |
| $\sigma^{+}_{Modulus}$ | 23.6 x $10^{-9}$ m | 22.1 x $10^{-9}$ m | 13.7 x $10^{-9}$ m |
| $\sigma^{-}_{Modulus}$ | 35.7 x $10^{-9}$ m | 18.2 x $10^{-9}$ m | 19.2 x $10^{-9}$ m |
| $Q_{25}$ | 83.9 x $10^{-9}$ m | 65.0 x $10^{-9}$ m | 54.6 x $10^{-9}$ m |
| $\sigma^{\pm}_{Q_{25}}$ | 19.6 x $10^{-9}$ m | 15.9 x $10^{-9}$ m | 16.2 x $10^{-9}$ m |
| $Q_{75}$ | 118.8 x $10^{-9}$ m | 105.3 x $10^{-9}$ m | 96.3 x $10^{-9}$ m |
| $\sigma^{\pm}_{Q_{75}}$ | 14.1 x $10^{-9}$ m | 22.6 x $10^{-9}$ m | 31.4 x $10^{-9}$ m |
| # PDF curves | 108 | 112 | 73 |

Table C.5.: Part 2 of the results: for the modulus and the 25% and 75% Quartile of the average PDF of height maps from different fluorescence label. The $\sigma^{+/-}_{Modulus}$-values refer to the distance to the boundary of the standard deviation area in the positive or negative height direction, the $\sigma^{\pm}_{Q}$-values refer to the distance to the boundary of the standard deviation area in the positive height direction for 75% Quartile and in negative height direction for 25% Quartile.

## C.4. Foci Detection

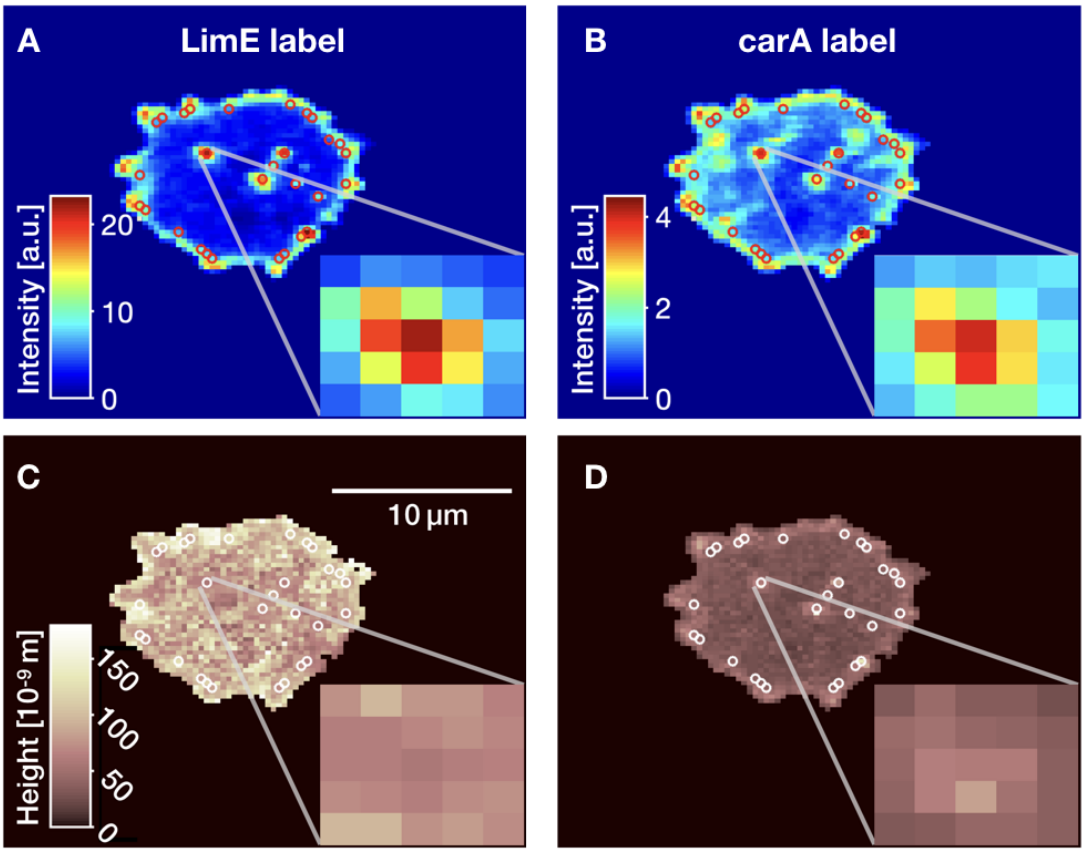


Figure C.6.: Micrograph of a WT NC4A2 cell with carA and LimE dual label. Showing the intensity of the actin channel (A) and membrane channel (B) and the associated height information below (C,D). The marked pixels show pre-selected actin foci, detected by the regional maxima routine by its prominence. Enlarged window shows an exemplary actin focus (A) and the corresponding regions on the carA micrographs. A membrane height increase at the position of the actin focus is visible (D).

Foci at the intensity images can be distinguished from their surroundings by their peak-like intensity increase. A pre-selection of foci is detected at the cytosolic contact area with removed vacuoles, as shown in Section C.1 and C.2 by detecting the position and prominence of local maxima with the *islocalmax* function. A prominence threshold is defined as product of the difference between maximum and minimum pixel intensity of non-zero matrix elements and a prominence factor, which is chosen as 0.2 for the LimE label. The pre-selected position of the actin foci are shown in Figures C.6, C.8 and C.9. The clathrin label appears in different intensity distributions, ranging from cells with low background intensity and clearly

definable foci, cells with medium intensity and still detectable foci and cells with high intensity as shown in Figure 5.2 (A), which are excluded because no foci detection is possible. Also, the clathrin label of medium background intensity shows regions of low intensity that where not recorded in the previous sections. Thus, areas of medium intensity with an adjacent low intensity region could be counted as a regional maximum and thus bias the pre-selection routine. To cover the different cases and to detect only clearly definable foci, the prominence factor of 0.4 is chosen. The pre-selected foci for the clathrin label are shown in Figure C.15
This routine also detects the intensity increase close to the removed contour of the contact area, which can be seen in Figure C.6. To exclude these points, the user selects the desired actin foci from a given set of pre-selected points in an interactive pop-up window.
In the next step the focus extend is defined. Therefore the region around each individual focus is transferred to a focus matrix, with an extent of 9 pixels in both directions and the regional maximum at its center, as shown in Figure C.7 (B). While the approach to examine a reasonably sized focus matrix to cover the focus extent is suitable for larger foci, or foci with an inactive surrounding, there is a possibility to find neighboring local maxima in one focus matrix. Furthermore, these maxima can also be connected by a medium intensity. However, if those maxima are detected by the prominence routine and are at least 4 pixels away from central maximum, a possible connection is disregarded and both points are separately detected and examined as individual maxima. If the distance between both detected maxima is smaller and the focus matrix covers the extent of the combined maxima, the routine treats these detected points as one focus. To reduce the possibility of repeated counting of pixels while evaluating neighboring foci, a circular area of 5 pixel in diameter at the position of the respective focus is set to zero.

To detect the focus extent, the focus matrix is divided by the average background intensity in the immediate vicinity of the focus. Therefore the elements of the matrix with erased rudimentary focus areas are transferred into a list and sorted in ascending order according to their values. The average intensity of the focus surrounding pixels is calculated for 60% of the list entries starting with the lowest, in the following referred to as surrounding intensity. Each entry of the resulting filter matrix is a multiplication factor of the surrounding intensity, as it is shown in Figure C.7 (C). The focus extent is defined as the pixel intensities higher then 1.8 times the surrounding intensity for the LimE signal, which is shown in Figure C.7 (D).
Due to the described variability of the background intensity for the clathrin label, the default focus extent threshold value is set at 1.5. However, the threshold is varied for the whole contact area, depending on the respective intensity matrix appearance. The lower boundary of the focus extent threshold is set to 1.3 times its background value. Detected regional maxima with less then 2 connected pixels at the lower boundary or with no pre-detected foci are excluded.
The described routine for foci determination is applied to the carA intensity images

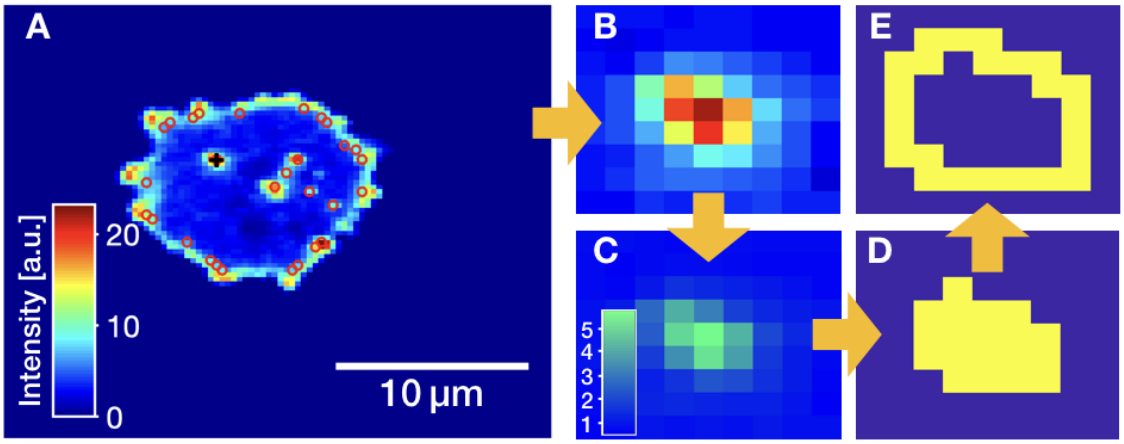


Figure C.7.: Micrographs of a WT NC4A2 cell with carA and LimE dual label illustrate the processing cascade to extract the template of the focus extent in a binary image (D). The intensity of the actin channel is shown in (A) with pre-selected actin foci. The foci marked by the black cross goes through the processing cascade, starting with the transfer into the focus matrix (B), filter (C), detection of the focus extent (D) and detection of the focus boundary (E). The resulting templates (D,E) are used for further processing.

as well, with adapted parameters, to detect regions of increased carA intensity. The prominence factor of the foci detection routine is set to 0.15 to detect less prominent regions of increased intensity, while the focus extent threshold is set to 1.4 times the background intensity. The focus matrix extent is increased because the current focus matrix cannot cover all possible foci for the carA label. Thus the focus matrix is increased to 13 pixels in each direction with the maximum of the focus in the middle. The pre-selection of detected foci is shown in Figure C.15. The binary templates are used to transfer the corresponding areas at the intensity and height matrices into lists. The weighted average height and its standard error are calculated for the focus and the focus boundary pixels for both height maps. Also, the average intensity at the focus and its boundary pixels is calculated for all fluorescence label. Further, the focus area is evaluated, which is calculated by the product of the number of pixel containing one focus and the area of one pixel and the number of foci per image is noted.

## C.5. Foci Results

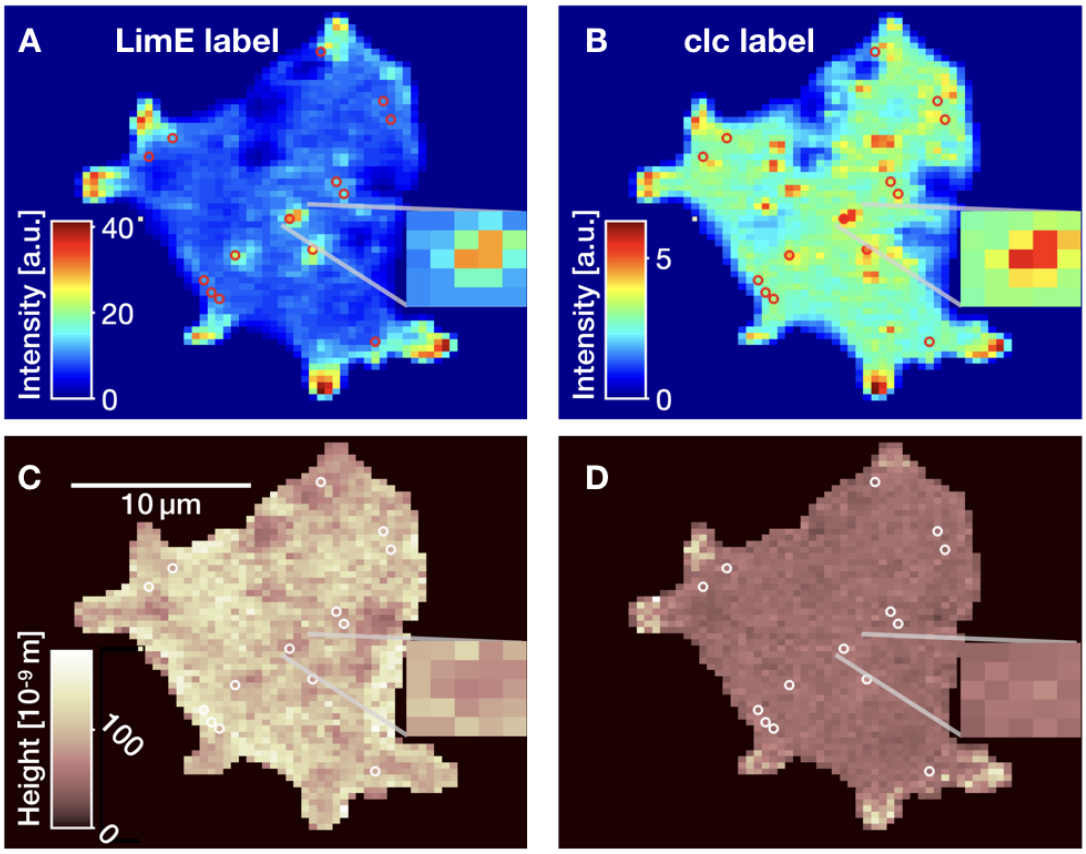


Figure C.8.: Micrograph of a WT NC4A2 cell with clc and LimE dual label. Showing the intensity of the actin channel (A) and clathrin channel (B) and the associated height informations below (C,D). The marked pixels show the pre-selected actin foci, with the regional maxima detection by prominence. Zoom-in shows an exemplary actin foci (A) and the corresponding regions on the other micrographes.

| # Foci | LimE label (carA) | LimE label (clc) | LimE label (clc-) | clc label (LimE) |
|---|---|---|---|---|
| Median | 5 | 4 | 10 | 8 |
| $\Delta^{+}_{\#Foci}$ | 2 | 2 | 3 | 3 |
| $\Delta^{-}_{\#Foci}$ | 3 | 1.5 | 3 | 2 |
| # points | 535 | 486 | 747 | 775 |
| $p_{1,2} - value$ | | 0.08 | $(W\ Test)$ | |
| $p_{1,3} - value$ | | 0 | $(W\ Test)$ | |
| $p_{2,3} - value$ | | 0 | $(W\ Test)$ | |

Table C.6.: Results for the number of detected foci. Result values shown are the median, the box width for the upper and lower box, the number of data points, the $p - value$ and the test performed. The indices refer to the compared coloumns.

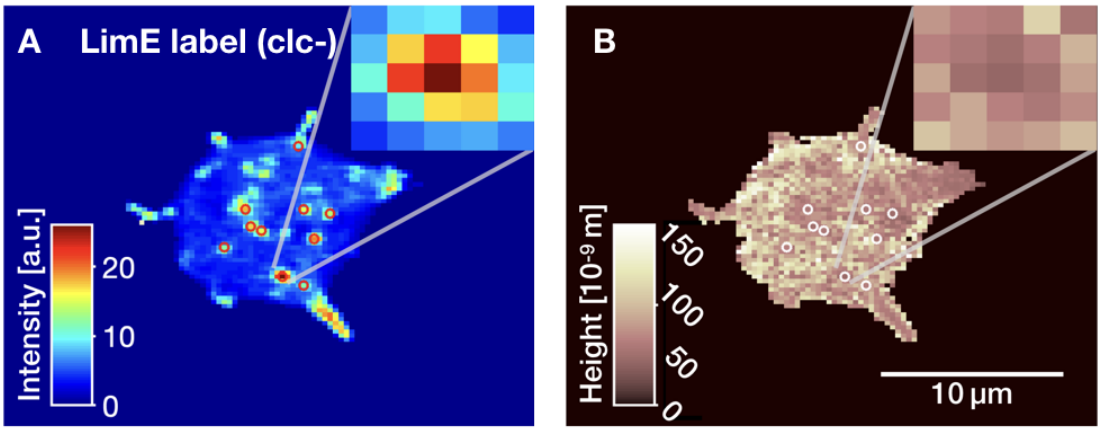


Figure C.9.: Micrograph of a WT NC4A2 cell with LimE label and clc knock-out. Showing the intensity of the actin channel (A) the associated height information (B). The marked pixels show the pre-selected actin foci, with the regional maxima detection by prominence. Zoom-in shows an exemplary actin foci (A) and the corresponding regions on the other micrographe.

| Area Foci | LimE label (carA) | LimE label (clc) | LimE label (clc-) | clc label (LimE) |
|---|---|---|---|---|
| Median | 0.36 x$10^{-12}$m$^2$ | 0.53x$10^{-12}$m$^2$ | 0.45x$10^{-12}$m$^2$ | 0.53x$10^{-12}$m$^2$ |
| $\Delta^{+}_{FociArea}$ | 0.35x$10^{-12}$m$^2$ | 0.36x$10^{-12}$m$^2$ | 0.36x$10^{-12}$m$^2$ | 0.19x$10^{-12}$m$^2$ |
| $\Delta^{-}_{FociArea}$ | 0.09x$10^{-12}$m$^2$ | 0.26x$10^{-12}$m$^2$ | 0.18x$10^{-12}$m$^2$ | 0.18x$10^{-12}$m$^2$ |
| # points | 535 | 486 | 747 | 775 |
| $p_{1,2} - value$ | | 5x$10^{-6}$ | ($W$ *Test*) | |
| $p_{1,3} - value$ | | 0.0004 | ($W$ *Test*) | |
| $p_{2,3} - value$ | | 0.13 | ($W$ *Test*) | |

Table C.7.: Results for the detected foci area at the cytosolic contact are. Result values shown are the median, the box width for the upper and lower box, the number of data points, the $p - value$ and the test performed. The indices refer to the compared coloumns.

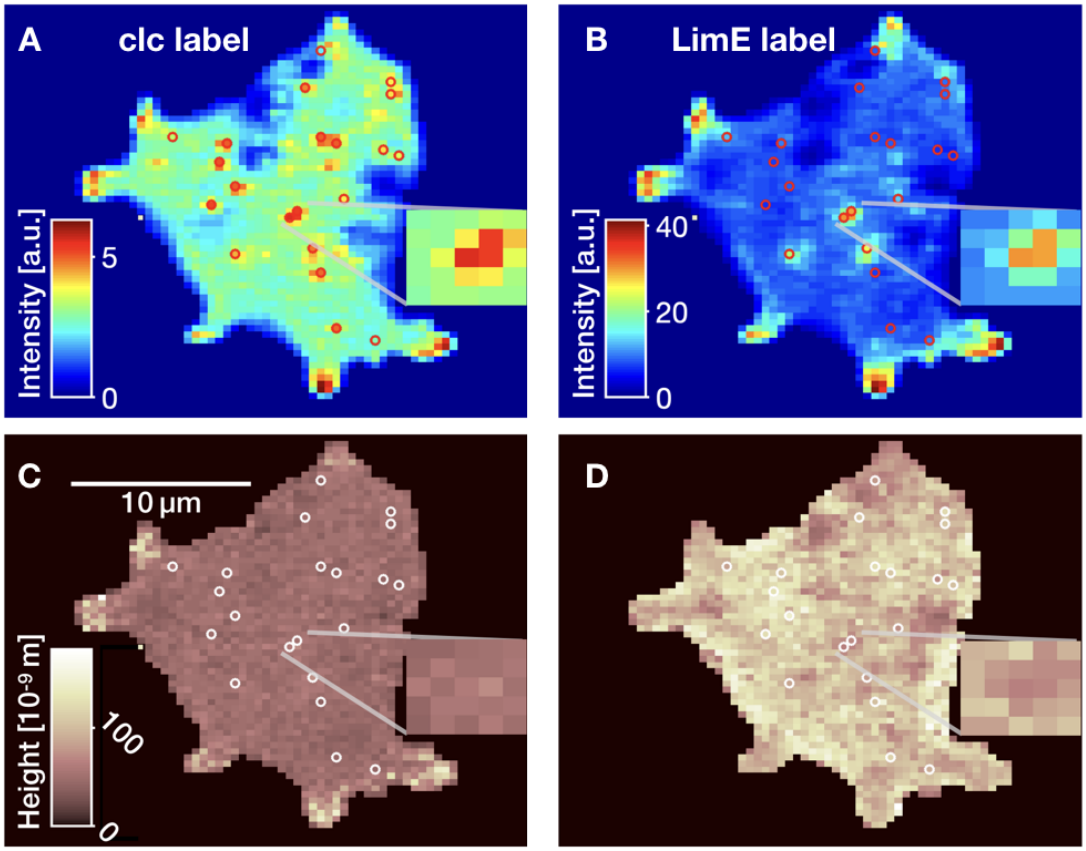


Figure C.10.: Micrograph of a WT NC4A2 cell with clc and LimE dual label. Showing the intensity of the clathrin channel (A) and actin channel (B) and the associated height informations below (C,D). The marked pixels show the pre-selected clathrin foci, with the regional maxima detection by prominence. Zoom-in shows an exemplary clathrin foci (A) and the corresponding regions on the other micrographes.

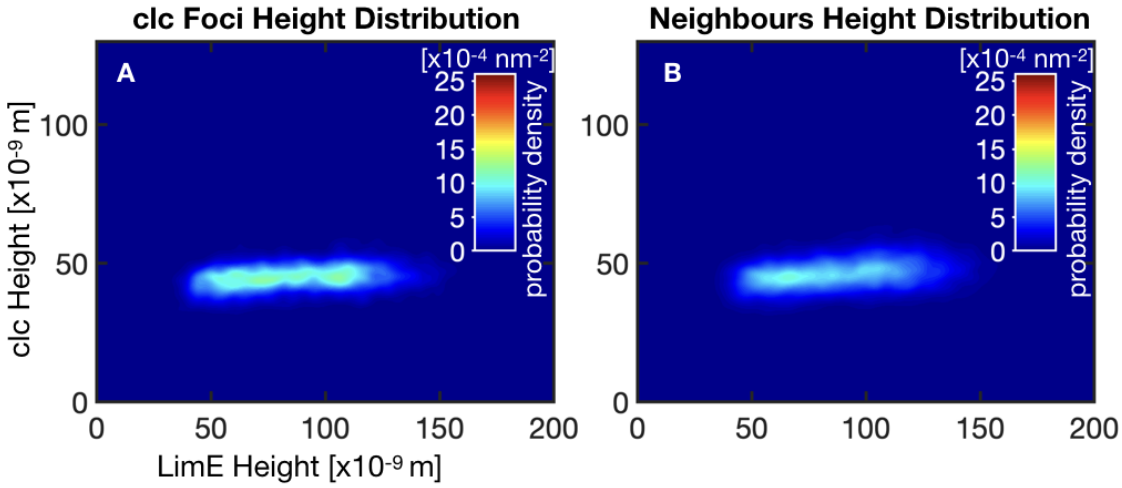


Figure C.11.: Probability density map shows the height of the clc label against the LimE label height above the substrate. The map in (A) shows the distribution for the pixels at the position of the detected clc foci with no detected increase of the averaged LimE intensity and (B) shows the distribution for the pixel adjacent to the foci.

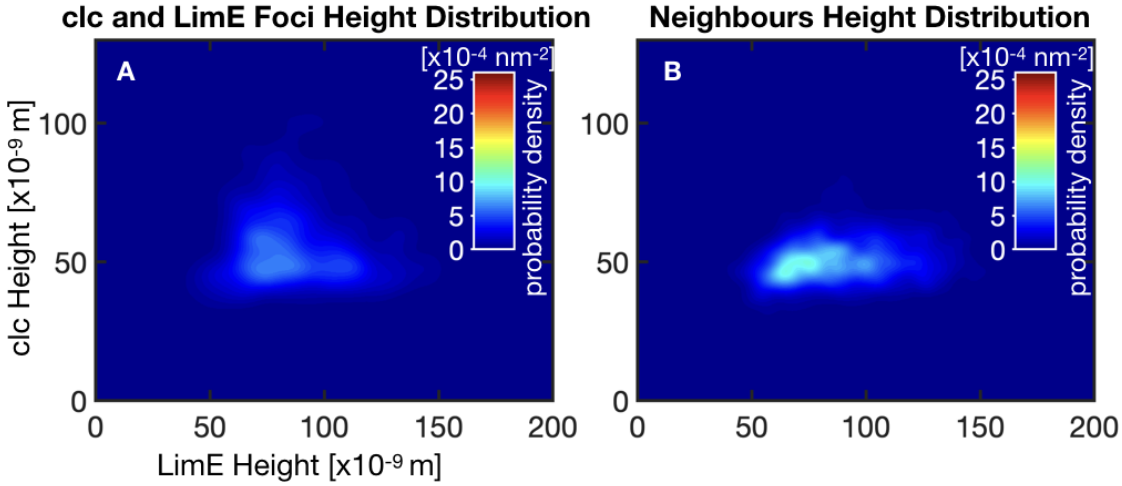


Figure C.12.: Probability density map shows the height of the clc label against the LimE label height above the substrate. The map in (A) shows the distribution for the pixels at the position of the detected clc foci with an increased LimE intensity and (B) shows the distribution for the pixel adjacent to the foci.

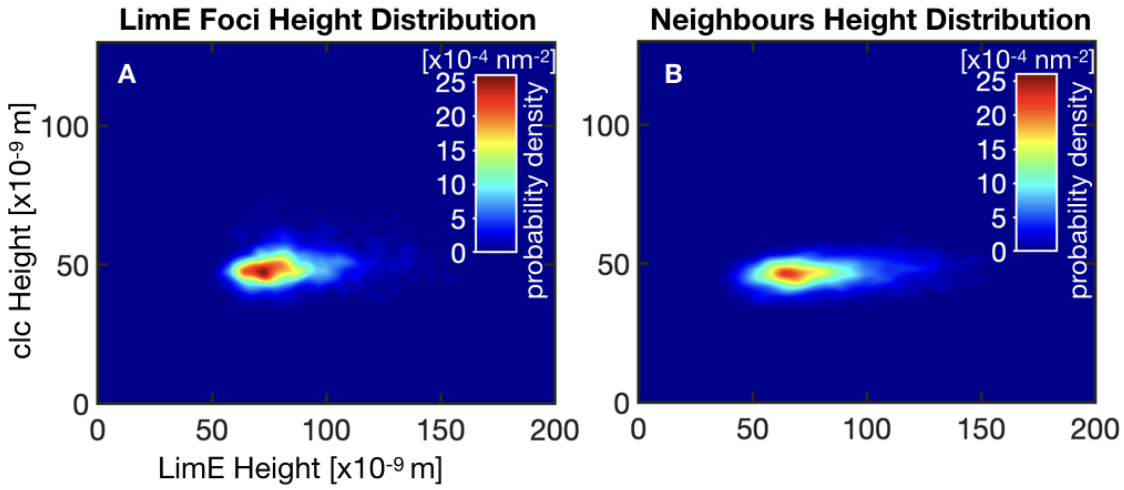


Figure C.13.: The probability density map shows the height of the clc label against the LimE label height above the substrate. The map in (A) shows the distribution for the pixels at the position of the detected LimE foci with no detected increase of the averaged clc intensity and (B) shows the distribution for the pixel adjacent to the foci.

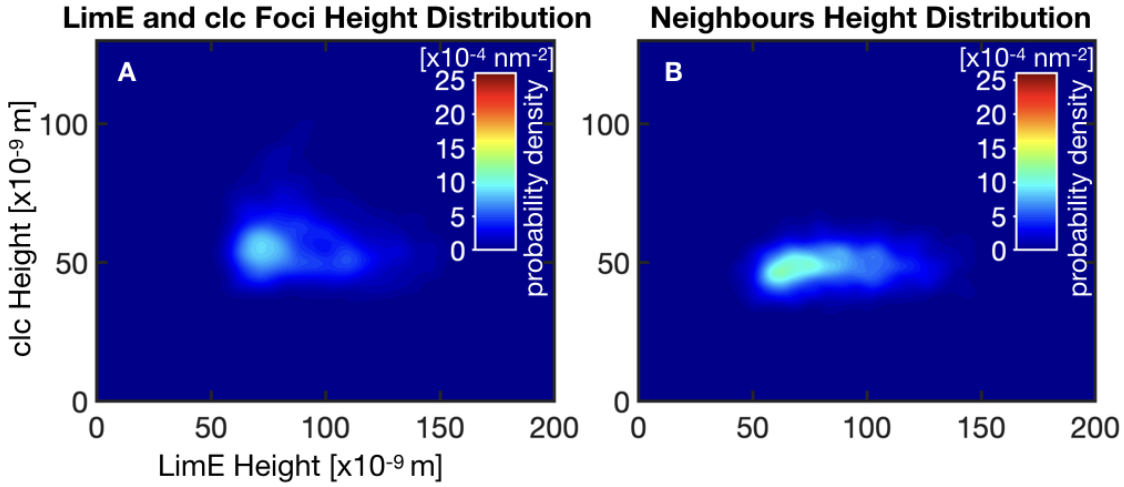


Figure C.14.: The probability density map shows the height of the clc label against the LimE label height above the substrate. The map in (A) shows the distribution for the pixels at the position of the detected LimE foci with an increased clc intensity and (B) shows the distribution for the pixel adjacent to the foci.

| | | Max. | X-Positon | Y-Position |
|---|---|---|---|---|
| LimE Foci (carA) | Max. Foci | $5.4\text{x}10^{-4}$ | $65.9\text{x}10^{-9}$ m | $54.3\text{x}10^{-9}$ m |
| | Max. Neighbours | $5.1\text{x}10^{-4}$ | $75.6\text{x}10^{-9}$ m | $46.3\text{x}10^{-9}$ m |
| | Diff. Max. | $3.8\text{x}10^{-4}$ | $62.8\text{x}10^{-9}$ m | $59.6\text{x}10^{-9}$ m |
| | Diff. Min. | $-3.7\text{x}10^{-4}$ | $105.1\text{x}10^{-9}$ m | $41.7\text{x}10^{-9}$ m |
| carA Foci (LimE) | Max. Foci | $1.1\text{x}10^{-3}$ | $72.1\text{x}10^{-9}$ m | $39.9\text{x}10^{-9}$ m |
| | Max. Neighbours | $7.0\text{x}10^{-4}$ | $95.0\text{x}10^{-9}$ m | $41.1\text{x}10^{-9}$ m |
| | Diff. Max. | $7.1\text{x}10^{-4}$ | $64.5\text{x}10^{-9}$ m | $40.1\text{x}10^{-9}$ m |
| | Diff. Min. | $-2.5\text{x}10^{-4}$ | $91.5\text{x}10^{-9}$ m | $50.2\text{x}10^{-9}$ m |
| carA & LimE Foci | Max. Foci | $4.1\text{x}10^{-4}$ | $68.9\text{x}10^{-9}$ m | $50.6\text{x}10^{-9}$ m |
| | Max. Neighbours | $5.3\text{x}10^{-4}$ | $81.9\text{x}10^{-9}$ m | $47.6\text{x}10^{-9}$ m |
| | Diff. Max. | $2.6\text{x}10^{-4}$ | $66.1\text{x}10^{-9}$ m | $66.7\text{x}10^{-9}$ m |
| | Diff. Min. | $-2.7\text{x}10^{-4}$ | $103.1\text{x}10^{-9}$ m | $42.1\text{x}10^{-9}$ m |
| LimE Foci (clc) | Max. Foci | $2.5\text{x}10^{-3}$ | $72.5\text{x}10^{-9}$ m | $47.3\text{x}10^{-9}$ m |
| | Max. Neighbours | $2.2\text{x}10^{-3}$ | $65.1\text{x}10^{-9}$ m | $46.5\text{x}10^{-9}$ m |
| | Diff. Max. | $1.2\text{x}10^{-3}$ | $79.5\text{x}10^{-9}$ m | $51.2\text{x}10^{-9}$ m |
| | Diff. Min. | $-9.8\text{x}10^{-4}$ | $57.7\text{x}10^{-9}$ m | $45.1\text{x}10^{-9}$ m |
| LimE & clc Foci | Max. Foci | $8.6\text{x}10^{-4}$ | $71.9\text{x}10^{-9}$ m | $55.8\text{x}10^{-9}$ m |
| | Max. Neighbours | $1.2\text{x}10^{-3}$ | $62.3\text{x}10^{-9}$ m | $46.8\text{x}10^{-9}$ m |
| | Diff. Max. | $6.1\text{x}10^{-4}$ | $71.9\text{x}10^{-9}$ m | $59.4\text{x}10^{-9}$ m |
| | Diff. Min. | $-9.0\text{x}10^{-4}$ | $59.8\text{x}10^{-9}$ m | $46.0\text{x}10^{-9}$ m |
| clc Foci (LimE) | Max. Foci | $1.3\text{x}10^{-3}$ | $105.2\text{x}10^{-9}$ m | $44.8\text{x}10^{-9}$ m |
| | Max. Neighbours | $1.1\text{x}10^{-3}$ | $66.5\text{x}10^{-9}$ m | $45.0\text{x}10^{-9}$ m |
| | Diff. Max. | $5.6\text{x}10^{-4}$ | $106.9\text{x}10^{-9}$ m | $43.8\text{x}10^{-9}$ m |
| | Diff. Min. | $-3.3\text{x}10^{-4}$ | $99.7\text{x}10^{-9}$ m | $53.5\text{x}10^{-9}$ m |
| clc & LimE Foci | Max. Foci | $6.6\text{x}10^{-4}$ | $80.2\text{x}10^{-9}$ m | $50.8\text{x}10^{-9}$ m |
| | Max. Neighbours | $1.0\text{x}10^{-3}$ | $74.4\text{x}10^{-9}$ m | $49.8\text{x}10^{-9}$ m |
| | Diff. Max. | $3.1\text{x}10^{-4}$ | $70.7\text{x}10^{-9}$ m | $64.4\text{x}10^{-9}$ m |
| | Diff. Min. | $-5.8\text{x}10^{-4}$ | $63.5\text{x}10^{-9}$ m | $46.3\text{x}10^{-9}$ m |

Table C.8.: Results for the maximum and in case of the difference curve between the foci PDF and the neighbours PDF also the minimum position of the 2-dimensional probability density maps for the different label and knock-out combinations as well as for sorted points of an additional LimE or clc foci.

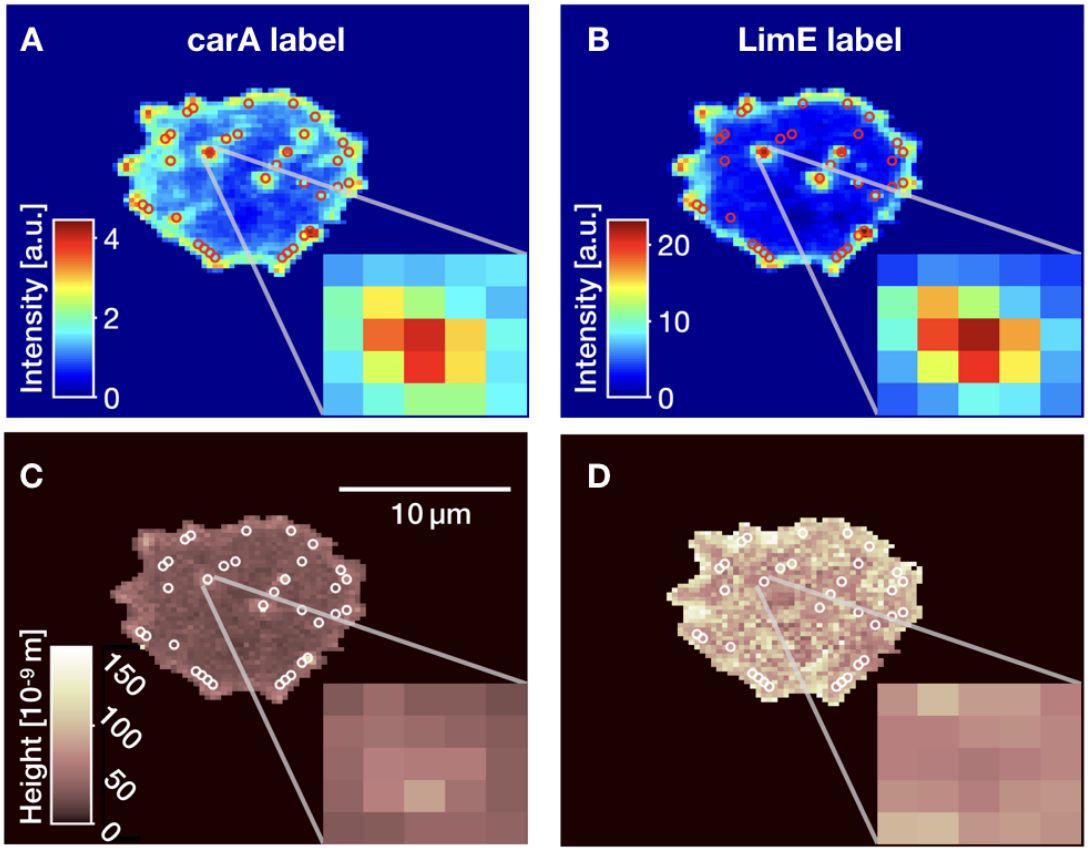


Figure C.15.: Micrograph of a WT NC4A2 cell with carA and LimE dual label. Showing the intensity of the carA channel (A) and actin channel (B) and the associated height informations below (C,D). The marked pixels show the pre-selected carA foci, with the regional maxima detection by prominence. Zoom-in shows an exemplary carA foci (A) and the corresponding regions on the other micrographes.

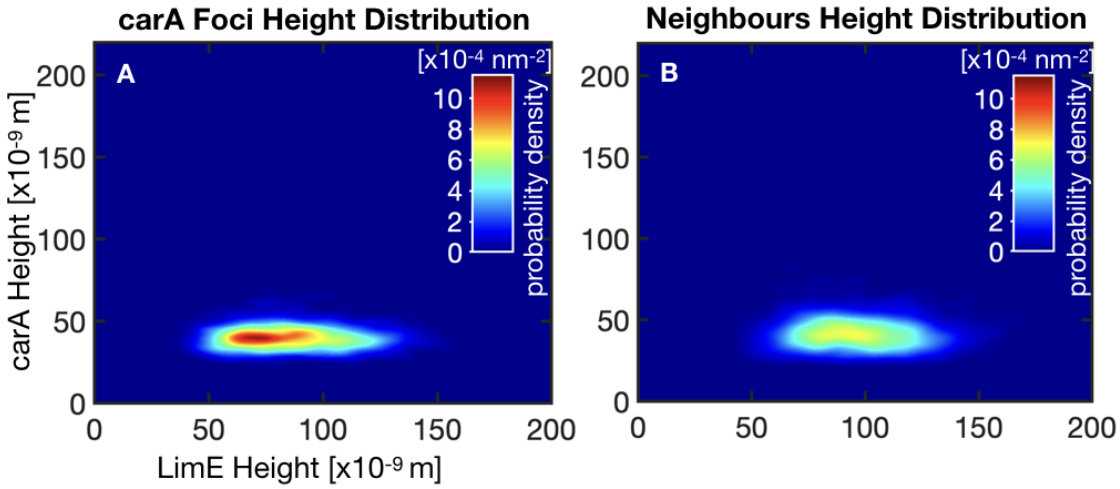


Figure C.16.: Probability density map shows the height of the carA label against the LimE label height above the substrate. The map in (A) shows the distribution for the pixels at the position of the detected carA foci with no detected increase of the averaged LimE intensity and (B) shows the distribution for the pixel adjacent to the foci.

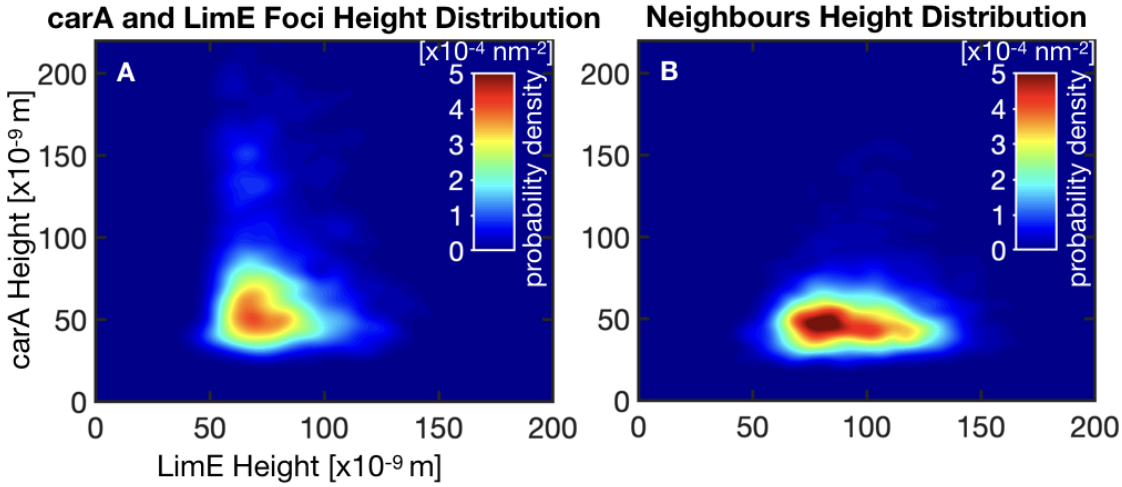


Figure C.17.: Probability density map shows the height of the carA label against the LimE label height above the substrate. The map in (A) shows the distribution for the pixels at the position of the detected carA foci with an increased LimE intensity and (B) shows the distribution for the pixel adjacent to the foci.

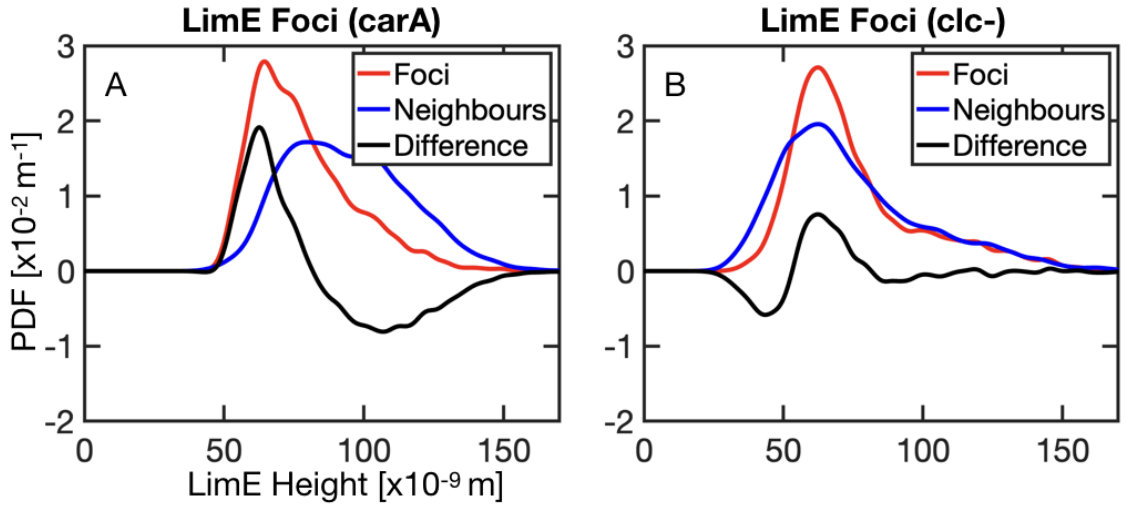


Figure C.18.: The PDF of the LimE foci height distribution, the neighbour height distribution and their difference is shown for the LimE and carA label combination in (A) and for the LimE label with clc- in (B).

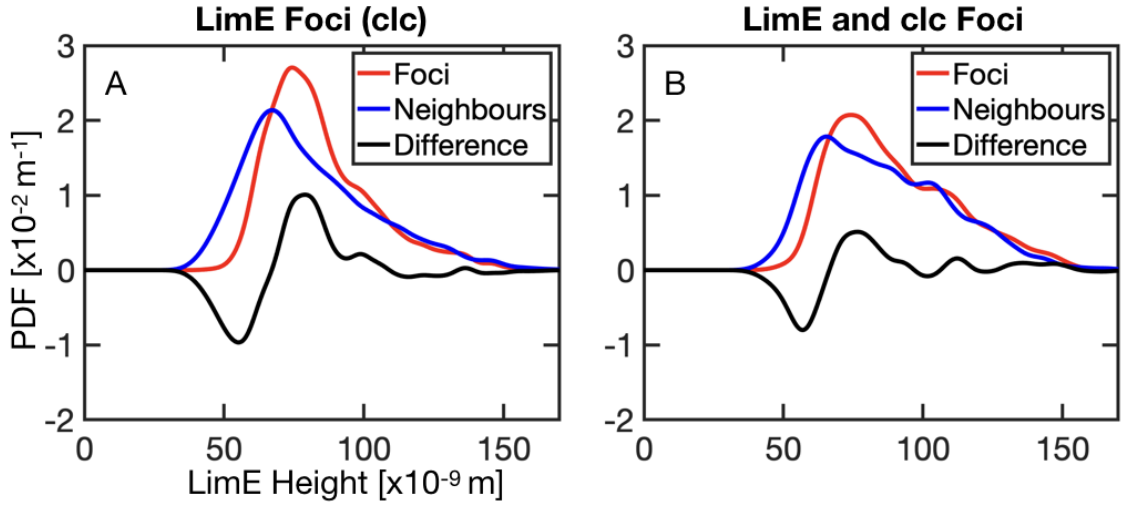


Figure C.19.: The PDF of the LimE foci height distribution, the neighbour height distribution and their difference is shown for the LimE foci with no detected increase of the averaged clc intensity in (A) and for the LimE foci with an increased average clc intensity (B).

| | | Max. | X-Position |
|---|---|---|---|
| LimE Foci (carA) | Max. Foci | $2.8\text{x}10^{-2}$ | $64.4\text{x}10^{-9}$ m |
| | Max. Neighbours | $1.7\text{x}10^{-2}$ | $79.6\text{x}10^{-9}$ m |
| | Max. Diff. | $1.9\text{x}10^{-2}$ | $62.6\text{x}10^{-9}$ m |
| | Min. Diff. | $-8.1\text{x}10^{-3}$ | $106.9\text{x}10^{-9}$ m |
| LimE Foci (clc) | Max. Foci | $2.7\text{x}10^{-2}$ | $74.3\text{x}10^{-9}$ m |
| | Max. Neighbours | $2.1\text{x}10^{-2}$ | $67.2\text{x}10^{-9}$ m |
| | Max. Diff. | $1.0\text{x}10^{-2}$ | $79.0\text{x}10^{-9}$ m |
| | Min. Diff. | $-9.7\text{x}10^{-3}$ | $55.2\text{x}10^{-9}$ m |
| LimE & clc Foci | Max. Foci | $2.1\text{x}10^{-2}$ | $74.1\text{x}10^{-9}$ m |
| | Max. Neighbours | $1.8\text{x}10^{-2}$ | $65.4\text{x}10^{-9}$ m |
| | Max. Diff. | $5.1\text{x}10^{-3}$ | $76.5\text{x}10^{-9}$ m |
| | Min. Diff. | $-8.0\text{x}10^{-3}$ | $56.9\text{x}10^{-9}$ m |
| LimE label (clc-) | Max. Foci | $2.7\text{x}10^{-2}$ | $62.3\text{x}10^{-9}$ m |
| | Max. Neighbours | $2.0\text{x}10^{-2}$ | $62.4\text{x}10^{-9}$ m |
| | Max. Diff. | $7.5\text{x}10^{-3}$ | $62.3\text{x}10^{-9}$ m |
| | Min. Diff. | $-5.8\text{x}10^{-3}$ | $43.5\text{x}10^{-9}$ m |

Table C.9.: Results for the maximum and in case of the difference curve between the foci PDF and the neighbours PDF also the minimum of the 1-dimensional LimE PDF for the different label and knock-out combinations.

| # Foci | LimE & clc Foci | LimE Foci (clc) |
|---|---|---|
| Median | 2 | 3 |
| $\Delta^{+}_{\#Foci}$ | 1 | 2 |
| $\Delta^{-}_{\#Foci}$ | 2 | 1 |
| # points | 186 | 300 |
| $p_{1,2} - value$ | 0.14 | ($W$ *Test*) |

Table C.10.: Results for the detected foci number at the cytosolic contact are. Result values shown are the median, the box width for the upper and lower box, the number of data points, the $p - value$ and the test performed.

| # Foci | clc & LimE Foci | clc Foci (LimE) |
|---|---|---|
| Median | 2 | 7 |
| $\Delta^{+}_{\#Foci}$ | 1 | 3 |
| $\Delta^{-}_{\#Foci}$ | 1 | 2 |
| # points | 126 | 648 |
| $p_{1,2} - value$ | 0 | $(W\ Test)$ |

Table C.11.: Results for the detected foci number at the cytosolic contact are. Result values shown are the median, the box width for the upper and lower box, the number of data points, the $p - value$ and the test performed.

| # Foci | carA & LimE Foci | carA Foci (LimE) |
|---|---|---|
| Median | 2 | 2 |
| $\Delta^{+}_{\#Foci}$ | 1 | 1 |
| $\Delta^{-}_{\#Foci}$ | 1 | 1 |
| # points | 317 | 159 |
| $p_{1,2} - value$ | 6.4x$10^{-3}$ | $(W\ Test)$ |

Table C.12.: Results for the detected foci number at the cytosolic contact are. Result values shown are the median, the box width for the upper and lower box, the number of data points, the $p - value$ and the test performed.

| Foci Area | LimE & clc Foci | LimE Foci (clc) |
|---|---|---|
| Median | 0.67 x$10^{-12}$m$^2$ | 0.36x$10^{-12}$m$^2$ |
| $\Delta^{+}_{FociArea}$ | 0.39x$10^{-12}$m$^2$ | 0.36x$10^{-12}$m$^2$ |
| $\Delta^{-}_{FociArea}$ | 0.22x$10^{-12}$m$^2$ | 0.09x$10^{-12}$m$^2$ |
| # points | 186 | 300 |
| $p_{1,2} - value$ | 0 | $(W\ Test)$ |

Table C.13.: Results for the detected foci number at the cytosolic contact are. Result values shown are the median, the box width for the upper and lower box, the number of data points, the $p - value$ and the test performed.

| Foci Area | clc & LimE Foci | clc Foci (LimE) |
|---|---|---|
| Median | 0.62 x$10^{-12}$m$^2$ | 0.45x$10^{-12}$m$^2$ |
| $\Delta^{+}_{FociArea}$ | 0.36x$10^{-12}$m$^2$ | 0.27x$10^{-12}$m$^2$ |
| $\Delta^{-}_{FociArea}$ | 0.22x$10^{-12}$m$^2$ | 0.1x$10^{-12}$m$^2$ |
| # points | 126 | 648 |
| $p_{1,2} - value$ | 4x$10^{-5}$ | $(W\ Test)$ |

Table C.14.: Results for the detected foci number at the cytosolic contact are. Result values shown are the median, the box width for the upper and lower box, the number of data points, the $p - value$ and the test performed.

| Foci Area | carA & LimE Foci | carA Foci (LimE) |
|---|---|---|
| Median | 0.71 x$10^{-12}$m$^2$ | 1.43x$10^{-12}$m$^2$ |
| $\Delta^{+}_{FociArea}$ | 0.54x$10^{-12}$m$^2$ | 0.65x$10^{-12}$m$^2$ |
| $\Delta^{-}_{FociArea}$ | 0.27x$10^{-12}$m$^2$ | 0.56x$10^{-12}$m$^2$ |
| # points | 317 | 159 |
| $p_{1,2} - value$ | 0 | ($W$ *Test*) |

Table C.15.: Results for the detected foci number at the cytosolic contact are. Result values shown are the median, the box width for the upper and lower box, the number of data points, the $p - value$ and the test performed.

| | | Max. | X-Positon | Y-Position |
|---|---|---|---|---|
| LimE Foci (carA) | Max. Diff. | 9.9x$10^{-4}$ | $-$11.9x$10^{-9}$m | 10.0x$10^{-9}$m |
| carA Foci (LimE) | Max. Diff. | 6.1x$10^{-3}$ | $-$8.3x$10^{-9}$m | $-$1.3x$10^{-9}$m |
| carA & LimE Foci | Max. Diff. | 6.6x$10^{-4}$ | $-$14.6x$10^{-9}$m | 12.7x$10^{-9}$m |
| LimE Foci (clc) | Max. Diff. | 4.4x$10^{-3}$ | 10.2x$10^{-9}$m | 1.0x$10^{-9}$m |
| LimE & clc Foci | Max. Diff. | 1.3x$10^{-3}$ | 5.7x$10^{-9}$m | 7.1x$10^{-9}$m |
| clc Foci (LimE) | Max. Diff. | 6.0x$10^{-3}$ | $-$1.5x$10^{-9}$m | $-$1.1x$10^{-9}$m |
| clc & LimE Foci | Max. Diff. | 1.9x$10^{-3}$ | $-$0.4x$10^{-9}$m | 2.9x$10^{-9}$m |

Table C.16.: Results for the maximum of the 2-dimensional probability density maps of the difference between the error weighted average pixel heights at the focus area and the averaged neighbour heights, for the different label and knock-out combinations as well as for sorted points of an additional LimE or clc foci.

| | Max. | Max. Diff.- Position |
|---|---|---|
| LimE Foci (carA) | 3.6x$10^{-2}$ | $-$16.8x$10^{-9}$m |
| LimE Foci (clc) | 2.4x$10^{-2}$ | 9.8x$10^{-9}$m |
| LimE & clc Foci | 2.1x$10^{-2}$ | 0.1x$10^{-9}$m |
| LimE label (clc-) | 2.4x$10^{-2}$ | $-$0.9x$10^{-9}$m |

Table C.17.: Results for the maximum of the 1-dimensional PDF of the difference between the error weighted averaged height at the detected LimE foci area and the neighbour average height distribution for the different label and knock-out combinations as well as for sorted points of an additional LimE or clc foci.

# D. Discussion

| | | WT NC4 | NC4 CLC- |
|---|---|---|---|
| l-difference | Median | 1.25 x $10^{-6}$ m | 1.45 x $10^{-6}$ m |
| | $p - value$ | 0.52 ($W$ *Test*) | |
| | $\Delta^{+}_{l-difference}$ | 1.49 x $10^{-6}$ m | 0.94 x $10^{-6}$ m |
| | $\Delta^{-}_{l-difference}$ | 0.44 x $10^{-6}$ m | 0.36 x $10^{-6}$ m |
| l-difference ratio | Median | 0.24 | 0.35 |
| | $p - value$ | 0.072 ($W$ *Test*) | |
| | $\Delta^{+}_{l-ratio}$ | 0.15 | 0.25 |
| | $\Delta^{-}_{l-ratio}$ | 0.09 | 0.14 |
| F-difference | Median | 1.84 x$10^{-9}$ N | 1.84x$10^{-9}$ N |
| | $p - value$ | 0.94 ($W$ *Test*) | |
| | $\Delta^{+}_{F-difference}$ | 0.96 x $10^{-9}$ N | 1.26 x $10^{-9}$ N |
| | $\Delta^{-}_{F-difference}$ | 0.79 x $10^{-9}$ N | 1.11 x $10^{-9}$ N |
| F-difference ratio | Median | 0.84 | 0.87 |
| | $p - value$ | 0.3 ($W$ *Test*) | |
| | $\Delta^{+}_{Fratio}$ | 0.05 | 0.03 |
| | $\Delta^{-}_{Fratio}$ | 0.08 | 0.10 |
| | Nr. points | 57 | 23 |

Table D.1.: Results for the maximum adhesion force per area (top row) and adhesion work per area (bottom row). Result values shown are the median, $p - value$ and the test performed, the box width for the upper and lower box and the number of data points.

# Bibliography


[1] Canel, Marta ; Serrels, Alan ; Frame, Margaret C. ; Brunton, Valerie G.: E-cadherin–integrin crosstalk in cancer invasion and metastasis. In: *J Cell Sci* 126 (2013), Nr. 2, S. 393–401

[2] Kamprad, Nadine ; Witt, Hannes ; Schröder, Marcel ; Kreis, Christian T. ; Bäumchen, Oliver ; Janshoff, Andreas ; Tarantola, Marco: Adhesion strategies of Dictyostelium discoideum–a force spectroscopy study. In: *Nanoscale* 10 (2018), Nr. 47, S. 22504–22519

[3] Fery, Andreas ; Weinkamer, Richard: Mechanical properties of micro-and nanocapsules: Single-capsule measurements. In: *Polymer* 48 (2007), Nr. 25, S. 7221–7235

[4] Flowers, Jonathan M. ; Li, Si I. ; Stathos, Angela ; Saxer, Gerda ; Ostrowski, Elizabeth A. ; Queller, David C. ; Strassmann, Joan E. ; Purugganan, Michael D.: Variation, sex, and social cooperation: molecular population genetics of the social amoeba Dictyostelium discoideum. In: *PLoS genetics* 6 (2010), Nr. 7, S. e1001013

[5] Pan, Miao ; Xu, Xuehua ; Chen, Yong ; Jin, Tian: Identification of a chemoattractant G-protein-coupled receptor for folic acid that controls both chemotaxis and phagocytosis. In: *Developmental cell* 36 (2016), Nr. 4, S. 428–439

[6] Bretschneider, Till ; Othmer, Hans G. ; Weijer, Cornelis J.: Progress and perspectives in signal transduction, actin dynamics, and movement at the cell and tissue level: lessons from Dictyostelium. In: *Interface Focus* 6 (2016), Nr. 5, S. 20160047

[7] Tariqul Islam, AFM ; Yue, Haicen ; Scavello, Margarethakay ; Haldeman, Pearce ; Rappel, Wouter-Jan ; Charest, Pascale G.: The cAMP-induced G protein subunits dissociation monitored in live Dictyostelium cells by BRET reveals two activation rates, a positive effect of caffeine and potential role of microtubules. (2018)

[8] Tarantola, Marco ; Bae, Albert ; Fuller, Danny ; Bodenschatz, Eberhard ; Rappel, Wouter-Jan ; Loomis, William F.: Cell substratum adhesion during early development of Dictyostelium discoideum. In: *PloS one* 9 (2014), Nr. 9, S. e106574

[9] Kessin, Richard H.: *Dictyostelium: evolution, cell biology, and the development of multicellularity*. Bd. 38. Cambridge University Press, 2001

[10] O'day, Danton H. ; Keszei, Alex: Signalling and sex in the social amoebozoans. In: *Biological Reviews* 87 (2012), Nr. 2, S. 313–329

[11] Pollard, Thomas D. ; Earnshaw, William C.: *Cell Biology*. 2004

[12] Pollard, Thomas D. ; Cooper, John A.: Actin, a central player in cell shape and movement. In: *Science* 326 (2009), Nr. 5957, S. 1208–1212

[13] Pollard, Thomas D.: Regulation of actin filament assembly by Arp2/3 complex and formins. In: *Annu. Rev. Biophys. Biomol. Struct.* 36 (2007), S. 451–477

[14] Davidson, Andrew J. ; Amato, Clelia ; Thomason, Peter A. ; Insall, Robert H.: WASP family proteins and formins compete in pseudopod-and bleb-based migration. In: *J Cell Biol* 217 (2018), Nr. 2, S. 701–714

[15] Clark, Kristopher ; Langeslag, Michiel ; Figdor, Carl G. ; Leeuwen, Frank N.: Myosin II and mechanotransduction: a balancing act. In: *Trends in cell biology* 17 (2007), Nr. 4, S. 178–186

[16] Kollmar, Martin: Thirteen is enough: the myosins of Dictyostelium discoideum and their light chains. In: *BMC genomics* 7 (2006), Nr. 1, S. 183

[17] Tsujioka, Masatsune ; Yumura, Shigehiko ; Inouye, Kei ; Patel, Hitesh ; Ueda, Masahiro ; Yonemura, Shigenobu: Talin couples the actomyosin cortex to the plasma membrane during rear retraction and cytokinesis. In: *Proceedings of the National Academy of Sciences* 109 (2012), Nr. 32, S. 12992–12997

[18] Uchida, Kazuhiko S. ; Yumura, Shigehiko: Dynamics of novel feet of Dictyostelium cells during migration. In: *Journal of cell science* 117 (2004), Nr. 8, S. 1443–1455

[19] Schwarz, Ulrich S. ; Safran, Samuel A.: Physics of adherent cells. In: *Reviews of Modern Physics* 85 (2013), Nr. 3, S. 1327

[20] Schwarz, Ulrich S. ; Gardel, Margaret L.: United we stand–integrating the actin cytoskeleton and cell–matrix adhesions in cellular mechanotransduction. In: *Journal of cell science* 125 (2012), Nr. 13, S. 3051–3060

[21] Baschieri, Francesco ; Dayot, Stéphane ; Elkhatib, Nadia ; Ly, Nathalie ; Capmany, Anahi ; Schauer, Kristine ; Betz, Timo ; Vignjevic, Danijela M. ; Poincloux, Renaud ; Montagnac, Guillaume: Frustrated endocytosis controls contractility-independent mechanotransduction at

clathrin-coated structures. In: *Nature communications* 9 (2018), Nr. 1, S. 3825

[22] Wozniak, Michele A. ; Modzelewska, Katarzyna ; Kwong, Lina ; Keely, Patricia J.: Focal adhesion regulation of cell behavior. In: *Biochimica et Biophysica Acta (BBA)-Molecular Cell Research* 1692 (2004), Nr. 2-3, S. 103–119

[23] Parsons, J T. ; Horwitz, Alan R. ; Schwartz, Martin A.: Cell adhesion: integrating cytoskeletal dynamics and cellular tension. In: *Nature reviews Molecular cell biology* 11 (2010), Nr. 9, S. 633

[24] Nobes, Catherine D. ; Hall, Alan: Rho, rac, and cdc42 GTPases regulate the assembly of multimolecular focal complexes associated with actin stress fibers, lamellipodia, and filopodia. In: *Cell* 81 (1995), Nr. 1, S. 53–62

[25] Welch, Matthew D. ; Mallavarapu, Aneil ; Rosenblatt, Jody ; Mitchison, Timothy J.: Actin dynamics in vivo. In: *Current opinion in cell biology* 9 (1997), Nr. 1, S. 54–61

[26] Lin, Chihung H. ; Espreafico, Enilza M. ; Mooseker, Mark S. ; Forscher, Paul: Myosin drives retrograde F-actin flow in neuronal growth cones. In: *Neuron* 16 (1996), Nr. 4, S. 769–782

[27] Raucher, Drazen ; Sheetz, Michael P.: Cell spreading and lamellipodial extension rate is regulated by membrane tension. In: *The Journal of cell biology* 148 (2000), Nr. 1, S. 127–136

[28] Alexandrova, Antonina Y. ; Arnold, Katya ; Schaub, Sébastien ; Vasiliev, Jury M. ; Meister, Jean-Jacques ; Bershadsky, Alexander D. ; Verkhovsky, Alexander B.: Comparative dynamics of retrograde actin flow and focal adhesions: formation of nascent adhesions triggers transition from fast to slow flow. In: *PloS one* 3 (2008), Nr. 9

[29] Sunnick, Eva ; Janshoff, Andreas ; Geil, Burkhard: Energetics of adhesion cluster formation in the context of biological membranes. In: *Physical Review E* 86 (2012), Nr. 5, S. 051913

[30] Fenz, Susanne F. ; Bihr, Timo ; Schmidt, Daniel ; Merkel, Rudolf ; Seifert, Udo ; Sengupta, Kheya ; Smith, Ana-Sunčana: Membrane fluctuations mediate lateral interaction between cadherin bonds. In: *Nature Physics* 13 (2017), Nr. 9, S. 906–913

[31] Balaban, Nathalie Q. ; Schwarz, Ulrich S. ; Riveline, Daniel ; Goichberg, Polina ; Tzur, Gila ; Sabanay, Ilana ; Mahalu, Diana ; Safran, Sam ; Bershadsky, Alexander ; Addadi, Lia u. a.: Force and focal adhesion assembly: a close relationship studied using elastic micropatterned substrates. In: *Nature cell biology* 3 (2001), Nr. 5, S. 466

[32] Bell, George I.: Models for the specific adhesion of cells to cells. In: *Science* 200 (1978), Nr. 4342, S. 618–627

[33] Erdmann, T ; Schwarz, US: Stability of adhesion clusters under constant force. In: *Physical review letters* 92 (2004), Nr. 10, S. 108102

[34] Trefalt, Gregor ; Borkovec, Michal: Overview of DLVO theory. In: *Laboratory of Colloid and Surface Chemistry, University of Geneva* 29 (2014)

[35] Loomis, William F. ; Fuller, Danny ; Gutierrez, Edgar ; Groisman, Alex ; Rappel, Wouter-Jan: Innate non-specific cell substratum adhesion. In: *PloS one* 7 (2012), Nr. 8, S. e42033

[36] Froquet, Romain ; Le Coadic, Marion ; Perrin, Jackie ; Cherix, Nathalie ; Cornillon, Sophie ; Cosson, Pierre: TM9/Phg1 and SadA proteins control surface expression and stability of SibA adhesion molecules in Dictyostelium. In: *Molecular biology of the cell* 23 (2012), Nr. 4, S. 679–686

[37] Kowal, Anthony S. ; Chisholm, Rex L.: Uncovering a role for the tail of the Dictyostelium discoideum SadA protein in cell-substrate adhesion. In: *Eukaryotic cell* 10 (2011), Nr. 5, S. 662–671

[38] Cornillon, Sophie ; Gebbie, Leigh ; Benghezal, Mohammed ; Nair, Prashant ; Keller, Sebastien ; Wehrle-Haller, Bernhard ; Charette, Steve J. ; Brückert, Franz ; Letourneur, François ; Cosson, Pierre: An adhesion molecule in free-living Dictyostelium amoebae with integrin $\beta$ features. In: *EMBO reports* 7 (2006), Nr. 6, S. 617–621

[39] Kamprad, Nadine ; Mamojan, Lyova ; Kvietkauskas, Justas ; Bae, Albert ; Tarantola, Marco: Actin foci dynamics and adhesion cluster mechanics of Dictyostelium discoideum. (*in preparation*)

[40] Riddelle-Spencer, Kathryn S. ; O'halloran, Theresa J.: Purification of clathrin heavy and light chain from Dictyostelium discoideum. In: *Protein expression and purification* 11 (1997), Nr. 3, S. 250–256

[41] Wang, Jingshan ; Wang, Yanqin ; O'Halloran, Theresa J.: Clathrin light chain: importance of the conserved carboxy terminal domain to function in living cells. In: *Traffic* 7 (2006), Nr. 7, S. 824–832

[42] Fotin, Alexander ; Cheng, Yifan ; Sliz, Piotr ; Grigorieff, Nikolaus ; Harrison, Stephen C. ; Kirchhausen, Tomas ; Walz, Thomas: Molecular model for a complete clathrin lattice from electron cryomicroscopy. In: *Nature* 432 (2004), Nr. 7017, S. 573

[43] Wakeham, Diane E. ; Chen, Chih-Ying ; Greene, Barrie ; Hwang, Peter K. ; Brodsky, Frances M.: Clathrin self-assembly involves coordinated weak

interactions favorable for cellular regulation. In: *The EMBO journal* 22 (2003), Nr. 19, S. 4980–4990

[44] O'HALLORAN, Theresa J. ; ANDERSON, RG: Clathrin heavy chain is required for pinocytosis, the presence of large vacuoles, and development in Dictyostelium. In: *The Journal of cell biology* 118 (1992), Nr. 6, S. 1371–1377

[45] NISWONGER, Maria L. ; O'HALLORAN, Theresa J.: Clathrin heavy chain is required for spore cell but not stalk cell differentiation in Dictyostelium discoideum. In: *Development* 124 (1997), Nr. 2, S. 443–451

[46] WANG, Jingshan ; VIRTA, Valerie C. ; RIDDELLE-SPENCER, Kathryn ; O'HALLORAN, Theresa J.: Compromise of clathrin function and membrane association by clathrin light chain deletion. In: *Traffic* 4 (2003), Nr. 12, S. 891–901

[47] OWEN, David J. ; COLLINS, Brett M. ; EVANS, Philip R.: Adaptors for clathrin coats: structure and function. In: *Annu. Rev. Cell Dev. Biol.* 20 (2004), S. 153–191

[48] KAKSONEN, Marko ; TORET, Christopher P. ; DRUBIN, David G.: Harnessing actin dynamics for clathrin-mediated endocytosis. In: *Nature reviews Molecular cell biology* 7 (2006), Nr. 6, S. 404

[49] MCMAHON, Harvey T. ; BOUCROT, Emmanuel: Molecular mechanism and physiological functions of clathrin-mediated endocytosis. In: *Nature reviews Molecular cell biology* 12 (2011), Nr. 8, S. 517

[50] TRAYNOR, David ; KAY, Robert R.: Possible roles of the endocytic cycle in cell motility. In: *Journal of Cell science* 120 (2007), Nr. 14, S. 2318–2327

[51] MACRO, Laura ; JAISWAL, Jyoti K. ; SIMON, Sanford M.: Dynamics of clathrin-mediated endocytosis and its requirement for organelle biogenesis in Dictyostelium. In: *J Cell Sci* 125 (2012), Nr. 23, S. 5721–5732

[52] VELTMAN, Douwe M. ; INSALL, Robert H.: WASP family proteins: their evolution and its physiological implications. In: *Molecular biology of the cell* 21 (2010), Nr. 16, S. 2880–2893

[53] VELTMAN, Douwe M. ; AUCIELLO, Giulio ; SPENCE, Heather J. ; MACHESKY, Laura M. ; RAPPOPORT, Joshua Z. ; INSALL, Robert H.: Functional analysis of Dictyostelium IBARa reveals a conserved role of the I-BAR domain in endocytosis. In: *Biochemical Journal* 436 (2011), Nr. 1, S. 45–52

[54] CHAO, Wei-Ting ; KUNZ, Jeannette: Focal adhesion disassembly requires clathrin-dependent endocytosis of integrins. In: *FEBS letters* 583 (2009), Nr. 8, S. 1337–1343

[55] Bridgewater, Rebecca E. ; Norman, Jim C. ; Caswell, Patrick T.: Integrin trafficking at a glance. In: *J Cell Sci* 125 (2012), Nr. 16, S. 3695–3701

[56] Lampe, Marko ; Vassilopoulos, Stéphane ; Merrifield, Christien: Clathrin coated pits, plaques and adhesion. In: *Journal of structural biology* 196 (2016), Nr. 1, S. 48–56

[57] Dannhauser, Philip N. ; Ungewickell, Ernst J.: Reconstitution of clathrin-coated bud and vesicle formation with minimal components. In: *Nature cell biology* 14 (2012), Nr. 6, S. 634

[58] Boulant, Steeve ; Kural, Comert ; Zeeh, Jean-Christophe ; Ubelmann, Florent ; Kirchhausen, Tomas: Actin dynamics counteract membrane tension during clathrin-mediated endocytosis. In: *Nature cell biology* 13 (2011), Nr. 9, S. 1124

[59] Heinrich, Doris ; Youssef, Simon ; Schroth-Diez, Britta ; Engel, Ulrike ; Aydin, Daniel ; Blümmel, Jacques ; Spatz, Joachim P. ; Gerisch, Günther: Actin-cytoskeleton dynamics in non-monotonic cell spreading. In: *Cell adhesion & migration* 2 (2008), Nr. 2, S. 58–68

[60] Förster, Th: Zwischenmolekulare energiewanderung und fluoreszenz. In: *Annalen der physik* 437 (1948), Nr. 1-2, S. 55–75

[61] Karedla, Narain ; Ruhlandt, Daja ; Chizhik, Anna M. ; Enderlein, Jörg ; Chizhik, Alexey I.: Metal-Induced Energy Transfer. In: *Advanced Photon Counting*. Springer, 2014, S. 265–281

[62] Clegg, Robert M.: Fluorescence resonance energy transfer. In: *Current opinion in biotechnology* 6 (1995), Nr. 1, S. 103–110

[63] Gregor, Ingo ; Chizhik, Alexey ; Karedla, Narain ; Enderlein, Jörg: Metal-induced energy transfer. In: *Nanophotonics* 8 (2019), Nr. 10, S. 1689–1699

[64] Enderlein, Jörg: Single-molecule fluorescence near a metal layer. In: *Chemical Physics* 247 (1999), Nr. 1, S. 1–9

[65] Chizhik, Alexey I. ; Gregor, Ingo ; Schleifenbaum, Frank ; Müller, Claus B. ; Röling, Christian ; Meixner, Alfred J. ; Enderlein, Jörg: Electrodynamic coupling of electric dipole emitters to a fluctuating mode density within a nanocavity. In: *Physical review letters* 108 (2012), Nr. 16, S. 163002

[66] Fey, Petra ; Kowal, Anthony S. ; Gaudet, Pascale ; Pilcher, Karen E. ; Chisholm, Rex L.: Protocols for growth and development of Dictyostelium discoideum. In: *Nature protocols* 2 (2007), Nr. 6, S. 1307

[67] Schneider, Natalie ; Weber, Igor ; Faix, Jan ; Prassler, Josef ; Müller-Taubenberger, Annette ; Köhler, Jana ; Burghardt, Emmanuel ; Gerisch, Günther ; Marriott, Gerard: A Lim protein involved in the progression of cytokinesis and regulation of the mitotic spindle. In: *Cell motility and the cytoskeleton* 56 (2003), Nr. 2, S. 130–139

[68] Karmakar, Richa ; Schich, Christoph ; Kamprad, Nadine ; Scheller, Vanessa ; Gutierrez, Edgar ; Groisman, Alex ; Rappel, Wouter-Jan ; Tarantola, Marco: Novel micropatterning technique reveals dependence of cell-substrate adhesion and migration of social amoebas on parental strain, development, and fluorescent markers. In: *PloS one* 15 (2020), Nr. 7, S. e0236171

[69] Xiao, Zhan ; Zhang, Ning ; Murphy, Douglas B. ; Devreotes, Peter N.: Dynamic distribution of chemoattractant receptors in living cells during chemotaxis and persistent stimulation. In: *The Journal of cell biology* 139 (1997), Nr. 2, S. 365–374

[70] Lemieux, Michael G. ; Janzen, Dani ; Hwang, Rander ; Roldan, Jeannette ; Jarchum, Irene ; Knecht, David A.: Visualization of the actin cytoskeleton: different F-actin-binding probes tell different stories. In: *Cytoskeleton* 71 (2014), Nr. 3, S. 157–169

[71] Friedrichs, Jens ; Legate, Kyle R. ; Schubert, Rajib ; Bharadwaj, Mitasha ; Werner, Carsten ; Müller, Daniel J. ; Benoit, Martin: A practical guide to quantify cell adhesion using single-cell force spectroscopy. In: *Methods* 60 (2013), Nr. 2, S. 169–178

[72] company, Asylum Research Oxford I.: *Applications Guide*. 2018. – Version 16, Revision: A-2053

[73] Asylum Research Oxford Instruments company, 6310 Hollister Ave, Santa Barbara, CA 93117: *Installation and Operation Manual*. 2008

[74] Butt, H-J ; Jaschke, Manfred: Calculation of thermal noise in atomic force microscopy. In: *Nanotechnology* 6 (1995), Nr. 1, S. 1

[75] Munz, Martin: Force calibration in lateral force microscopy: a review of the experimental methods. In: *Journal of Physics D: Applied Physics* 43 (2010), Nr. 6, S. 063001

[76] BD Biosciences Discovery Labware, Two oak park, Bedford, MA 01730 : *BD CELL-TAK™Cell and Tissue Adhesive, Catalog No. 354240*. 2001. – Lot No. 40404

[77] Taubenberger, Anna ; Cisneros, David A. ; Friedrichs, Jens ; Puech, Pierre-Henri ; Muller, Daniel J. ; Franz, Clemens M.: Revealing early steps of $\alpha 2\beta 1$ integrin-mediated adhesion to collagen type I by using single-cell force spectroscopy. In: *Molecular biology of the cell* 18 (2007), Nr. 5, S. 1634–1644

[78] Taubenberger, Anna V. ; Hutmacher, Dietmar W. ; Muller, Daniel J.: Single-cell force spectroscopy, an emerging tool to quantify cell adhesion to biomaterials. In: *Tissue Engineering Part B: Reviews* 20 (2013), Nr. 1, S. 40–55

[79] Sariisik, Ediz ; Popov, Cvetan ; Müller, Jochen P. ; Docheva, Denitsa ; Clausen-Schaumann, Hauke ; Benoit, Martin: Decoding cytoskeleton-anchored and non-anchored receptors from single-cell adhesion force data. In: *Biophysical journal* 109 (2015), Nr. 7, S. 1330–1333

[80] Schindelin, Johannes ; Arganda-Carreras, Ignacio ; Frise, Erwin ; Kaynig, Verena ; Longair, Mark ; Pietzsch, Tobias ; Preibisch, Stephan ; Rueden, Curtis ; Saalfeld, Stephan ; Schmid, Benjamin u. a.: Fiji: an open-source platform for biological-image analysis. In: *Nature methods* 9 (2012), Nr. 7, S. 676–682

[81] Lakowicz, Joseph R.: *Principles of fluorescence spectroscopy*. Springer Science & Business Media, 2013

[82] Caswell, Patrick T. ; Vadrevu, Suryakiran ; Norman, Jim C.: Integrins: masters and slaves of endocytic transport. In: *Nature reviews Molecular cell biology* 10 (2009), Nr. 12, S. 843–853

[83] Ferreira, Filipe ; Foley, Matthew ; Cooke, Alex ; Cunningham, Margaret ; Smith, Gemma ; Woolley, Robert ; Henderson, Graeme ; Kelly, Eamonn ; Mundell, Stuart ; Smythe, Elizabeth: Endocytosis of G protein-coupled receptors is regulated by clathrin light chain phosphorylation. In: *Current Biology* 22 (2012), Nr. 15, S. 1361–1370

[84] Saffarian, Saveez ; Cocucci, Emanuele ; Kirchhausen, Tomas: Distinct dynamics of endocytic clathrin-coated pits and coated plaques. In: *PLoS biol* 7 (2009), Nr. 9, S. e1000191

[85] Stavrou, Irene ; O'Halloran, Theresa J.: The monomeric clathrin assembly protein, AP180, regulates contractile vacuole size in Dictyostelium discoideum. In: *Molecular biology of the cell* 17 (2006), Nr. 12, S. 5381–5389

[86] Wessels, Deborah ; Reynolds, Josh ; Johnson, Olof ; Voss, Edward ; Burns, Royce ; Daniels, Karla ; Garrard, Elizabeth ; O'Halloran, Teresa J. ; Soll, David R.: Clathrin plays a novel role in the regulation of cell

polarity, pseudopod formation, uropod stability and motility in Dictyostelium. In: *Journal of Cell Science* 113 (2000), Nr. 1, S. 21–36

[87] Bloomfield, Gareth ; Tanaka, Yoshimasa ; Skelton, Jason ; Ivens, Alasdair ; Kay, Robert R.: Widespread duplications in the genomes of laboratory stocks of Dictyostelium discoideum. In: *Genome biology* 9 (2008), Nr. 4, S. R75

[88] Shelden, Eric ; Knecht, David A.: Mutants lacking myosin II cannot resist forces generated during multicellular morphogenesis. In: *Journal of Cell Science* 108 (1995), Nr. 3, S. 1105–1115

[89] Pollitt, Alice Y. ; Blagg, Simone L. ; Ibarra, Neysi ; Insall, Robert H.: Cell motility and SCAR localisation in axenically growing Dictyostelium cells. In: *European journal of cell biology* 85 (2006), Nr. 9-10, S. 1091–1098

[90] Kamprad, N. ; Tarantola, M.: The dual role of Actin foci in Adhesion and Endocytosis of Dictyostelium discoideum. (2018)

[91] Idrissi, Fatima-Zahra ; Grötsch, Helga ; Fernández-Golbano, Isabel M. ; Presciatto-Baschong, Cristina ; Riezman, Howard ; Geli, María-Isabel: Distinct acto/myosin-I structures associate with endocytic profiles at the plasma membrane. In: *The Journal of cell biology* 180 (2008), Nr. 6, S. 1219–1232

[92] Ghosh, Arindam ; Tsukanov, Roman ; Chizhik, Alexey ; Gregor, Ingo ; Karedla, Narain ; Enderlein, Jörg: Dynamics using Metal Induced Energy Transfer (DynaMIET): Probing Nanoscale Biomolecular Dynamics at Single-Molecule Level.

[93] Changede, Rishita ; Xu, Xiaochun ; Margadant, Felix ; Sheetz, Michael P.: Nascent integrin adhesions form on all matrix rigidities after integrin activation. In: *Developmental cell* 35 (2015), Nr. 5, S. 614–621

[94] Press, WH ; Teukolsky, SA ; Vetterling, WT ; Flannery, BP: Statistical description of data. In: *Numerical Recipes in C: The Art of Scientific Computing* (1992), S. 636

[95] WaveMetrics, Inc. P.O. Box 2088 Lake Oswego, OR 97035 USA: *Igor Pro Manula, Volume III - User's Guide Part 2, Chapter 12 Statistics*

[96] Hogg, Robert V. ; Tanis, Elliot A. ; Zimmerman, Dale L.: *Probability and statistical inference*. Pearson/Prentice Hall, 2010

[97] Silverman, Bernard W.: *Density estimation for statistics and data analysis*. Bd. 26. CRC press, 1986

[98] Botev, Zdravko I. ; Grotowski, Joseph F. ; Kroese, Dirk P. u. a.: Kernel density estimation via diffusion. In: *The annals of Statistics* 38 (2010), Nr. 5, S. 2916–2957

[99] Botev, Zdravko I.: *Kernel Density Estimator*. (https://www.mathworks.com/matlabcentral/fileexchange/14034-kernel-density-estimator), . – MATLAB Central File Exchange. Retrieved July 1, 2020

[100] Botev, Zdravko I.: *Kernel Density Estimation*. (https://www.mathworks.com/matlabcentral/fileexchange/17204-kernel-density-estimation), . – MATLAB Central File Exchange. Retrieved July 1, 2020